REDESIGN AND NUMERICAL ANALYSIS OF AN AEROSPACE HEAT EXCHANGER FOR LASER POWDER BED FUSION

by

Tharuka Kuruppu

Submitted in partial fulfilment of the requirements
for the degree of Master of Applied Science

at

Dalhousie University
Halifax, Nova Scotia
August 2024

Dalhousie University is located in Mi'kma'ki, the
Ancestral and unceded territory of the Mi'kmaq
We are all Treaty people.

Table of Contents

List of Tables

List of Figures

Abstract

Additive manufacturing (AM) offers significant potential for the design and manufacture of heat exchangers with complex internal geometries, not feasible to fabricate through traditional manufacturing techniques. This thesis presents the design process and numerical simulations of heat transfer in an additively manufactured direct replacement heat exchanger for an aircraft engine. The heat exchanger is a Fuel Oil Heat Exchanger (FOHE), where the engine's hot lubrication oil is used to preheat the fuel. In doing so, an AM design optimized for Laser Powder Bed Fusion (LPBF) process that incorporates a Triply Periodic Minimal Surface (TPMS) lattice for the heat exchanger core was developed. A steady state conjugate heat transfer simulation was modeled using Reynolds-averaged Navier-Stokes (RANS) approach with the k-omega SST turbulence model. Variations in lattice wall thickness, material, and fluid mass flow rate were analyzed to assess their impact on the fuel outlet temperature. The study finds the variation in lattice wall thickness and material properties of solid body exert minimal influence on the fuel outlet temperature in a steady state condition. The thermal resistance analysis of the system indicate that the fluid's thermal resistance overshadows that of the AM material. Hence, optimization of fluid dynamics within the heat exchanger core is necessary to enhance heat exchanger performance further. The results affirm the AM-derived heat exchanger offers equivalent performance to the conventionally fabricated counterpart but also highlight a path for design improvements focusing on the fluid domain. Further efforts are required to improve the AM geometry and heat transfer between the oil and fuel. This research underlines the viability of AM for complex thermal systems and sets a foundation for future exploration into optimizing heat exchanger designs.

List of Abbreviations Used

3D	three-dimensional
AM	Additive Manufacturing
ASTM	American Society for Testing and Materials
CAD	Computer Aided Design
CFD	Computational Fluid Dynamic
CMM	Coordinate Measuring Machine
CNC	Computer Numerical Control
CT	Computed Tomography
CTE	Coefficient of Thermal Expansion
DLMS	Direct Metal Laser Sintering
DSC	Differential Scanning Calorimeter
FFF	Fused Filament Fabrication
HITEMMP	High Intensity Thermal Exchange through Materials and Manufacturing Processes
LFA	Laser Flash Analysis
LPBF	Laser Powder Bed Fusion
MTPS	Modified Transient Plane Source
PLA	Polylactic Acid
PSD	Powder Size Distribution
RANS	Reynolds-Averaged Navier-Stokes
SEM	Scanning Electron Microscope

SI	International System of Unit
SLM	Selective Laser Melting
SST	Shear Stress Transport
STI	Screw Thread Insert
TPMS	Triply Periodic Minimal Surface
TPS	Transient Plane Source

Acknowledgements

The author would like to acknowledge Tronosjet and Mitacs for their financial support. Special thanks go to Dr. Paul Bishop, the research supervisor, for his continuous guidance, insightful feedback, and unwavering support, and to Dr. Matthew Harding for his dedication and effort in initiating the master's journey. The author would also like to thank Dr. Mohammad Saeedi and Dr. Dominic Groulx for their assistance in conducting the numerical analysis. Gratitude is extended to Equispheres for providing the stock material for the project. Additionally, the author appreciates the laboratory assistance provided by colleagues at Dalhousie University—Kenzie Timmons, Addison Rayner, Jon Hierlihy, Melissa Trask, and Conner Spence—for their invaluable assistance in conducting preliminary material analysis.

Chapter 1 Introduction

1.1 Thesis Motivation

The motivation for this research stems from the growing need for advanced heat exchanger designs that leverage the unique capabilities of additive manufacturing (AM). Currently, traditional manufacturing methods often impose limitations on the complexity and efficiency of heat exchangers. As industries, particularly aerospace, strive for higher performance and efficiencies, there is a pressing need to explore new heat exchanger designs and manufacturing techniques.

AM, especially laser powder bed fusion (LPBF), offers unprecedented design freedom, enabling the fabrication of complex geometries that are not feasible to manufacture through traditional manufacturing methods. This capability is particularly advantageous in manufacturing intricate internal structures that can enhance heat transfer performance. Additionally, with AM, it is possible to optimize the structure to reduce weight and increase fuel efficiency.

This research aims leverage the capabilities inherent to metal AM to redesign a conventionally fabricated aerospace fuel oil heat exchanger for production via LPBF. The goal is to replicate the functionality of the traditional heat exchanger and enhance its performance through innovative design approaches that take full advantage of AM concepts. This research will provide valuable insight into the design, optimization and manufacturing processes of the AM heat exchanger, and a numerical analysis of the thermal performance. Furthermore, the AM-derived heat exchanger will be a technology demonstration component to support the industry partner.

1.2 Problem Definition and Objectives

The heat exchanger in focus is a heat-oil heater for a turboprop engine. As shown in Figure 1, this traditionally manufactured heat exchanger is fabricated from aluminum alloys using several manufacturing processes including sheet metal stamping, brazing, welding, casting,

and machining. Sheet metal stamping and casting involve high tooling cost and long lead times, while manual operations such as welding and brazing introduce inconsistencies in dimensionality, weight, and performance. Reliance on multiple suppliers for different parts adds further complexity to the supply chain while increasing the risk of quality control issues and production delays. AM offers a unique opportunity to manufacture this component using fewer manufacturing processes and fewer suppliers, while potentially reducing weight, improving performance, and enhancing part to part consistency. The AM design can also leverage exceptional levels of design freedom to optimize geometry for improved pressure drop while meeting all thermal performance metrics. Accordingly, the objective of this research is to develop a direct replacement aircraft engine fuel-oil heat exchanger designed for AM. The developed heat exchanger will be used as a technology demonstration piece for the industry partner and a learning opportunity to understand the design process as well as optimization of AM heat exchangers.

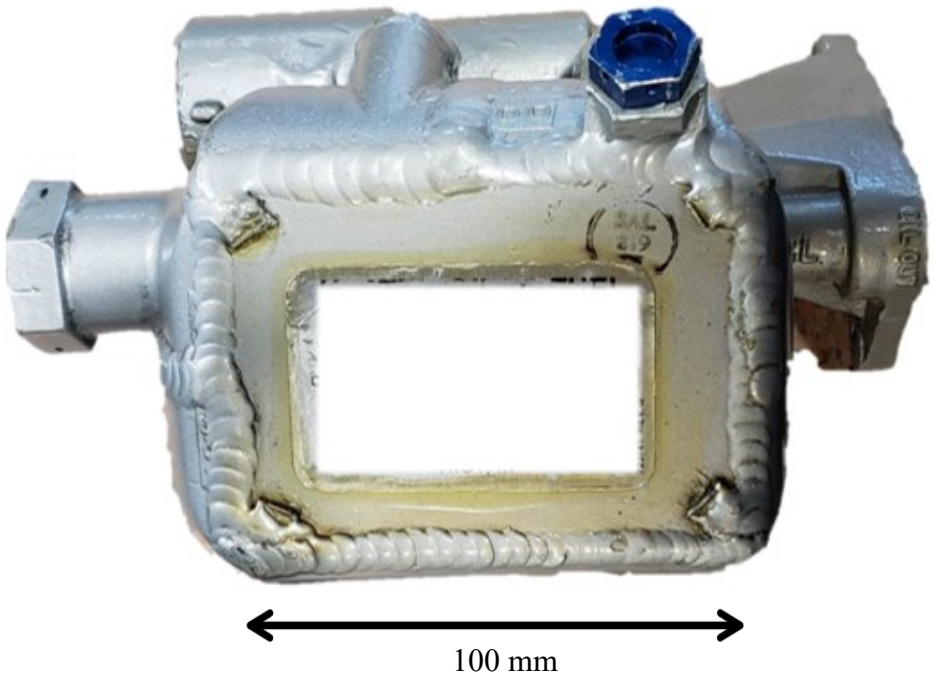

Figure 1: Traditionally manufactured aluminum heat exchanger

1.2.1 Design Requirements

To be a direct replacement for the conventionally fabricated heat exchanger, certain constraints must be imposed to ensure proper fit and function. Specific requirements were as follows:

1) Physically, the AM counterpart design must fit within the bounding box of the traditional component to ensure, it does not interfere with other components in the aircraft.
2) It must also have identical inlets, outlets, and mounting features as the traditional counterpart to ensure full and complete connectivity with the engine itself.
3) The heat exchanger core must be optimized to attain a comparable pressure drop and heat transfer efficiency.
4) The design must integrate a standardized thermally controlled valve system to regulate the outlet temperature of the fuel as found in the conventional design.
5) Since part consolidation is a key advantage for AM, the developed heat exchanger shall be fabricated as a single piece component.
6) The print model of the heat exchanger shall be constrained to fit within the usable volume of the Renishaw 500S Flex printer (250 mm × 250 mm × 350 mm) used for component fabrication [1].
7) The final geometry must be developed in accordance with design for AM principles to minimize the use of support structures and simplify any post processing requirements.
8) Prototypes must be fabricated from AlSi10Mg powder (Equispheres, ON, Canada).

1.3 Background

AM is a manufacturing process that fabricates components through successive addition of material in a layer-by-layer process. Applicable materials include polymers, metals and ceramics. The aerospace industry has been a leading early adopter and plays a prominent role in continued growth, primarily due to its need for highly complex and lightweight components in low annual production volumes. Projections by GE and SmarTech

publishing indicate that the aerospace industry will take account for 21% of global AM revenue, representing the largest single sector by revenue [2].

One major focus for the aerospace sector's use of AM is in the fabrication of heat exchangers. Established in 2018 and on going, the US Department of Energy's Advanced Research Projects Agency has invested over $36 million in their High Intensity Thermal Exchange through Materials and Manufacturing Processes (HITEMMP) program with many grants focused on the use of AM for heat sink fabrication [3]. The application of AM in this domain is motivated by the design freedom that enables the creation of complex lattice structures with a high surface to volume ratio and the capacity to consolidate features thereby reducing the need for extensive assembly and brazing procedures common to conventional methods employed for heat exchanger production [4].

One prominent example is GE Aerospace's GE9X engine, developed for the Boeing 777X family of aircrafts, incorporates 267 metal AM components, including an aluminum heat exchanger which is 40% lighter and 25% cheaper. Notably, the AM design consolidates 163 parts found in the traditional heat exchanger into a single unit [5]. Typically, aerospace heat exchangers are utilized to preheat the fuel and cool the engine oil. Preheating the fuel reduces the viscosity of the fluid thus reducing the pressure drop within the system while increasing the fuel efficiency through enhanced atomization when it is injected into the combustion chamber.

Niknam et al. [6] have conducted a comprehensive review on AM heat exchanger opportunities and challenges. They outlined significant opportunities in AM-enabled heat exchangers to produce optimized geometries with enhanced surface-controlled surface roughness, fully controlled and organized porous structures, and the elimination of joining (welding and/or brazing) operations. Schnabel et al. [7] have conducted two case studies on heat exchanger design for AM. One study designed and manufactured a counter flow water-to-water miniature heat exchanger for a feasibility test to demonstrate achievable efficiency compared to conventional heat exchangers. Here, the AM heat exchanger weighed less than half of its conventional counterpart. In a second study, the team evaluated an air-to-air counterflow heat exchanger for micro gas turbine systems. Even though the

AM component was costly, it was impossible to manufacture through traditional manufacturing methods.

The design for AM heat exchangers can also leverage Triply Periodic Minimum Surface (TPMS) lattice structures; a feature that is challenging, or in many cases impossible, to replicate through traditional manufacturing methods [8]. TPMS lattice structures, with their high surface area-to-volume ratio, are prime candidates for heat exchangers. Moreover, TPMS surfaces divide the design volume into two separate domains, a feature that is ideal for fluid-to-fluid heat exchangers. In one instance, Advanced Engineering Solutions [9] utilized a TPMS lattice in a heat exchanger designed to cool the gearbox oil of a helicopter. The AM design being half the volume and four times more efficient than the conventional component, is a strong testament to the unique advantages that TPMS lattice structures bring to heat exchanger designs.

Baobaid et al. (2022) [10] explored the potential of TPMS lattice structures for heat sink applications using computational fluid dynamics (CFD) models. Their results showed that the TPMS-based heat sink outperformed conventional heat sinks by 48–61%. Similarly, Puntozero [11] has redesigned a liquid-cooled cold plate for automotive power electronics. It uses a gyroid lattice that has been warped using advanced Field-Driven design techniques to increase the surface area by three times and reduce the weight by 25%.

Moradmand et al. (2024) [12] have conducted numerical and experimental studies on the thermal-hydraulic performance of heat exchangers with Schwarz-P and gyroid TPMS structures. The gyroid lattice significantly improved heat transfer performance compared to conventional tube banks. In contrast, the Schwarz-P lattice did not show any notable improvement in thermal performance over the conventional heat exchanger design. Additionally, the study revealed that the shear stress transport (SST) turbulence model provided better agreement with the experimental results, with an error of 0.8%.

These studies establish a strong foundation for understanding the benefits of AM heat exchangers. AM opens the opportunity to design heat exchangers that are lighter and more efficient compared to conventionally fabricated counterparts, hence being more appealing for aerospace, as it would lead to significant savings in fuel and carbon emissions over the lifespan of the aircraft [13] [14] [15] [16].

This study provides a case study on the design, assessment and production of an aircraft fuel oil heat exchanger utilized LPBF Am technology. The purpose of the heat exchanger is to preheat the fuel before it enters the engine. The conventionally manufactured heat exchanger involves a multitude of manufacturing processes, is expensive, and has become challenging to source given the age of the aircraft engine in question. Hence, the motivation behind the project is to develop a direct replacement heat exchanger via AM that is lightweight, requires fewer manufacturing processes, and meets the performance requirements for the application. This paper outlines the Computer Aided Design (CAD) workflow, geometry meshing, setting physics and boundary conditions, numerical and data analysis as well as the AM-based production of a functional prototype.

1.4 Heat Exchanger Classification

Heat exchangers are crucial components in various industrial applications and are instrumental in maintaining required performance of complex systems such as gas turbine engines. Their effectiveness and efficiency depend on the design and classification. R. K. Shah et al.'s Fundamentals of Heat Exchanger Design [17] classifies heat exchangers by their heat transfer process, number of fluids, construction features, flow arrangements, surface compactness, and heat transfer mechanism, as shown in Figure 3.

At a high level, transfer processes are categorized as indirect, and direct contact types. In indirect-contact heat exchangers, the fluids remain separate and transfer heat through a solid wall, such as tubular, plate-type, and extended-surface heat exchangers. In direct-contact type heat exchangers, the fluid comes into direct contact with the different fluids, exchanging heat, such as cooling towers and desuperheaters. The compactness of the heat exchanger is classified by its heat transfer surface area per unit volume. Compact heat exchangers are used in aerospace applications where component weight and volume are critical concerns.

The construction of the heat exchanger refers to its design, and flow arrangement refers to the fluid path within it. For fuel oil heat exchangers where the fluid’s phase does not change, its heat transfer mechanism can be classified as single-phase convection on both

sides as both oil and fuel fluids remain in the same initial phase throughout the heat exchanger, and convection heat transfer is the dominant heat transfer mechanism. Conversely, radiation heat transfer mechanism is found in high temperature waste recovery exchangers, fossil-fuel power plant boilers, incinerators and other fired heat exchangers.

The construction features can also be used to classify and differentiate heat exchanger designs. The primary types of construction include tubular, plat type, extended surface, and regenerative exchangers. Tubular heat exchangers are fabricated from a series of tubes, where hot and cold fluid flow and transfer heat from tube to tube. This design is preferred for high-pressure and high-temperature applications, making it suitable for a wide range of industrial applications. Plate-type heat exchangers utilize multiple thin plates separated by a thin gap to create channels for fluid flow, as shown in Figure 4. They are highly customizable and repairable due to their modular design. For example, the number of plates can be adjusted to meet required heat transfer needs, and singular damaged plates can be readily replaced in lieu of scrapping the entire heat exchanger. However, plate-type heat exchangers generally cannot accommodate low-pressure drop requirements due to their abrupt fluid flow path. Extended surface heat exchangers utilize thin fins extending from the solid walls separating the fluids, as shown in Figure 2, to increase surface area and enhance heat transfer performance, making them highly efficient and compact. The fins are usually thinner than the primary wall dividing the hot and cold fluids. Therefore, the fins introduce a lower thermal resistance surface for enhanced heat transfer, encouraging mixing and turbulent flow. These designs are commonly used in the aerospace and automotive industries, where high efficiency and lightweight are crucial. Finally, regenerative construction is a storage-type heat exchanger design in which the heat transfer surface or medium is periodically moved into and out of the fluids to transfer heat. Common use cases for regenerative designs are gas turbines, industrial furnaces, and ventilating systems where continuous heat recovery is employed.

Understanding these classifications allows for a more detailed breakdown of traditionally manufactured aerospace heat exchangers. It provides insight into different heat exchanger designs manufactured using traditional techniques. As AM becomes more prevalent, these

classification categories will likely evolve to accommodate novel heat exchanger designs that are only manufacturable through AM.

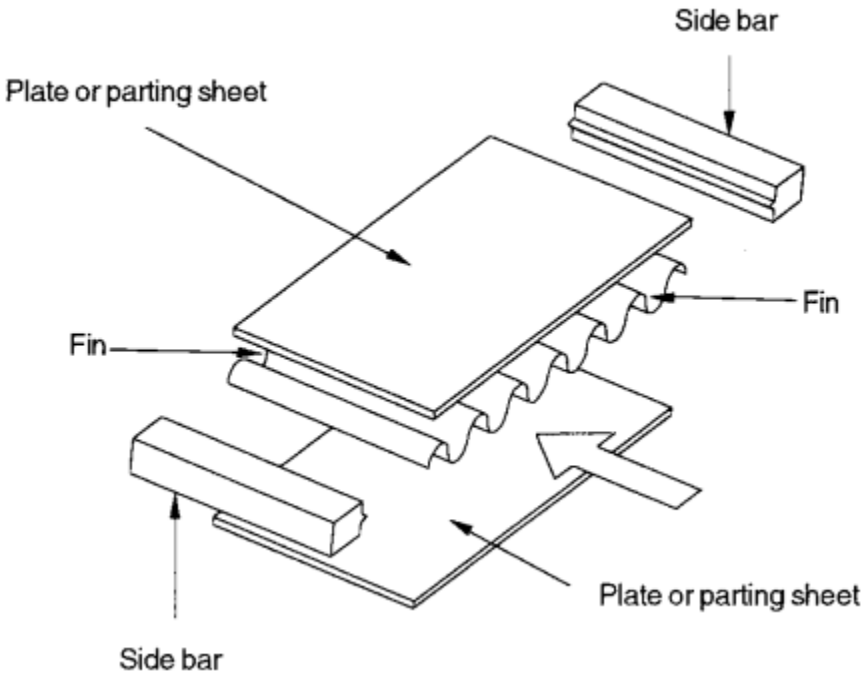

Figure 2: Components of a plate fin heat exchanger [17]

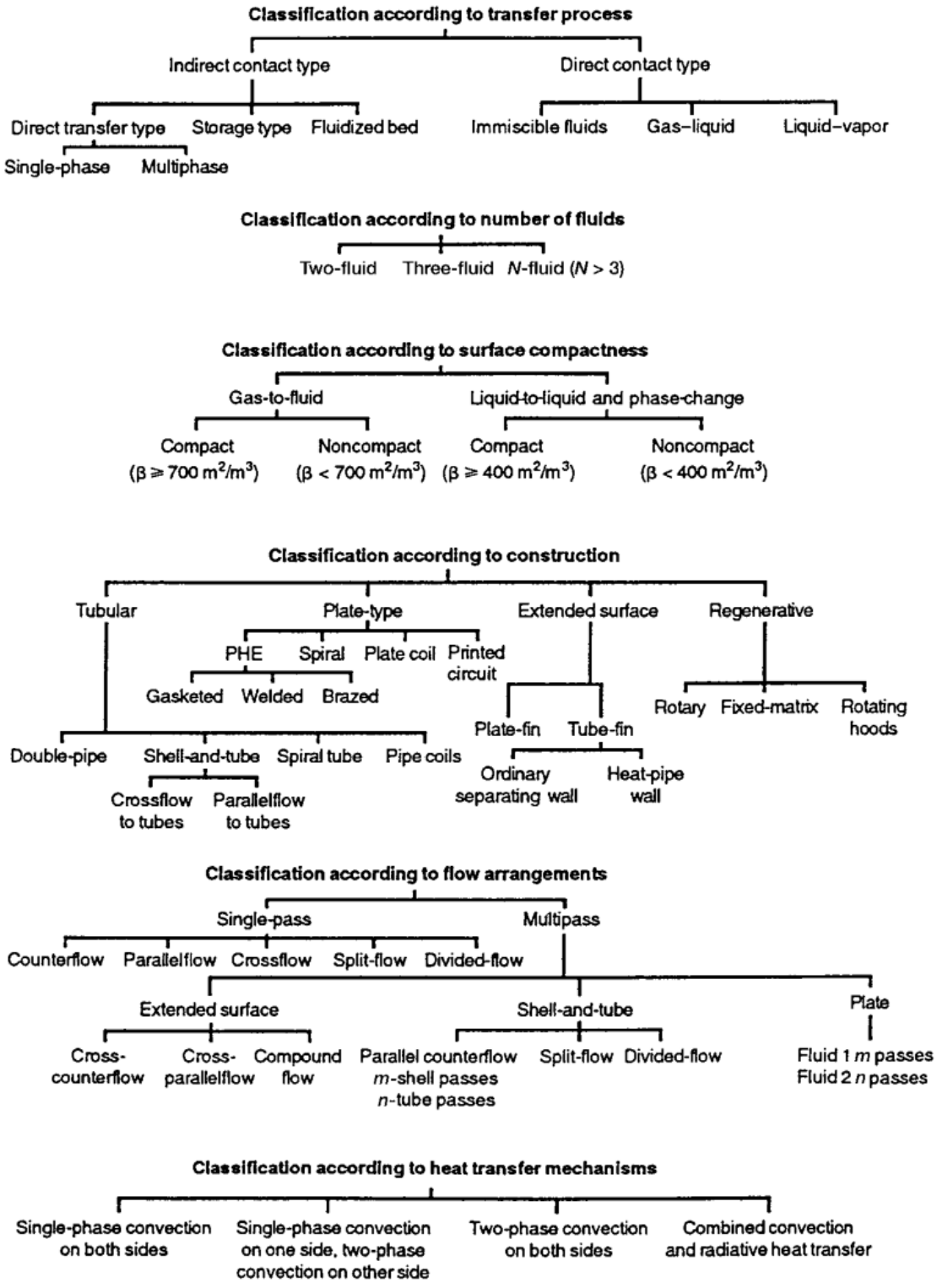

Figure 3: Classification of heat exchangers [17]

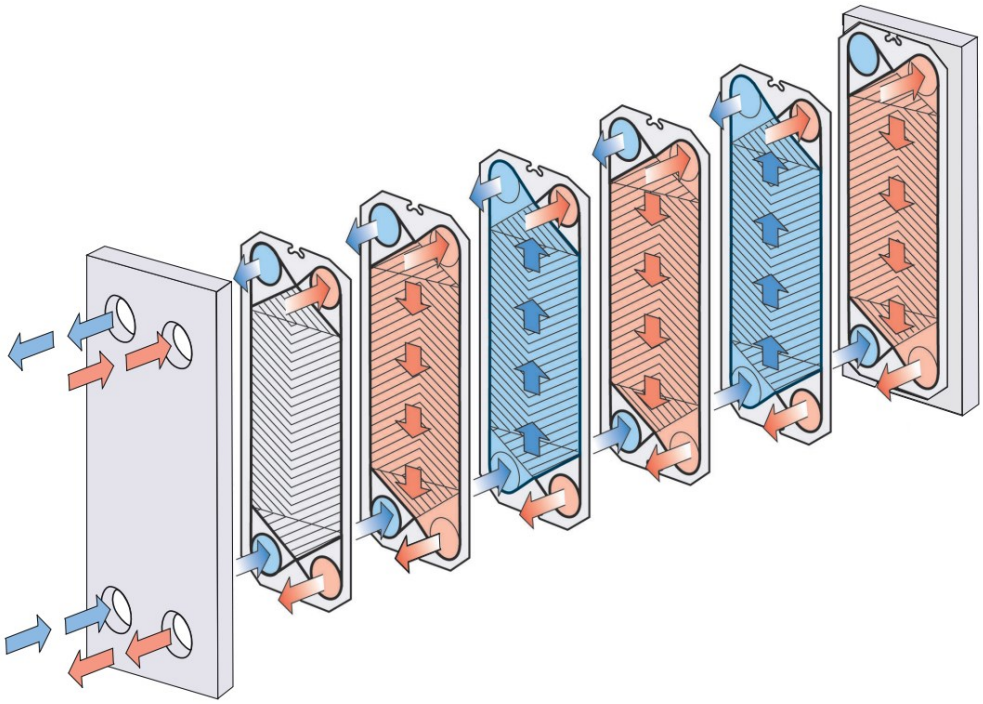

Figure 4:Schematic of plate heat exchanger [18]

1.5 Fundamentals of Heat Transfer

The thermodynamic definition for heat (Q) is the form of energy transfer from a higher temperature boundary system to a lower temperature system. Therefore, heat transfer occurs solely because of the temperature difference and is defined as when energy transfers from one boundary into another. When a two-boundary system reaches an equilibrium temperature, the heat transfer then falls to zero. A positive heat transfer represents energy transferred into the system, and a negative heat transfer represents energy transferred from the system. Similarly to work, heat is a transfer of energy; therefore, the International System of Unit (SI) for heat transfer is Joules (J).

There are three primary mechanisms for heat transfer: convection, conduction, and radiation. Understanding these mechanisms is crucial for a comprehensive understanding of heat transfer.

1.5.1 Convection Heat Transfer

Convection heat transfer occurs in fluid mediums, where heat is transferred due to a change in density. Density is a function of temperature. When the temperature of a fluid increases, its density decreases. Therefore, the lower-density particles in the fluid rise due to buoyancy, which carries heat energy with it.

Convection heat transfer can be calculated using Newton's law of cooling equation (1).

$$\dot{Q} = -Ah\Delta T \tag{1}$$

Where, $\dot{Q}$ is the rate of heat transfer, A is the heat transfer surface area, h is the convection heat transfer coefficient of the fluid, and ΔT is the difference in temperature.

The convection heat transfer coefficient is a function of density, specific heat, viscosity, the temperature of the fluid, the dimensionality of the surface, and the flow type (turbulent or laminar).

To increase convection heat transfer in a heat exchanger, the heat exchanger design should maximize the surface area interfacing with the fluids, introduce geometries that encourage turbulent flow, and maximize the temperature gradient between the heat transfer wall and fluid.

1.5.2 Conduction Heat Transfer

Conduction heat transfer occurs through molecular vibrations. When a molecule is heated, its kinetic energy increases, causing the molecule to vibrate. The vibrating molecules collide with adjacent molecules to transfer energy. This heat transfer mechanism is most effective within solids, as molecules are packed close together, increasing the extent of molecule collisions.

Conduction heat transfer can be calculated using Fourier's law (2).

$$\dot{Q} = -kA\frac{dT}{dx} \tag{2}$$

In this equation k represent the thermal conductivity of the material, A is the cross-sectional area of the heat transfer surface and $\frac{dT}{dx}$ is the temperature gradient within the material.

To increase conduction heat transfer in a heat exchanger, the material of the wall dividing the fluids must exhibit a high thermal conductivity while the thickness of the wall must be minimized to obtain a high thermal gradient and maximize the area of the wall interfacing with the fluids. The use of lattice structures fabricated from a conductive metal such as copper or aluminum is one way that these traits can be maintained. Specifically, Gyroid-type lattices are ideal candidates for the internal structure of a heat exchanger as the lattice is parametrically optimized for a maximum surface area to weight ratio [19]. Additionally, a gyroid lattice contains two separate volumes that do not overlap, which is ideal for an indirect contact type heat exchanger.

1.5.3 Radiation Heat Transfer

Radiation heat transfer refers to thermal energy transferred through electromagnetic waves. Radiation heat transfer does not require a medium to travel through but does require substances to transmit and absorb thermal energy. All bodies over the temperature of absolute zero, radiate energy in the form of radiation. However, only wavelengths between 0.1um to 100um radiate as thermal radiation [20]. A blackbody is an ideal thermal radiator as it absorbs all wavelengths.

The rate of heat transfer by radiation can be determined by the Stefan-Boltzmann law of radiation (3).

$$\dot{Q} = \sigma e A T^4 \tag{3}$$

Where σ is the Stefan-Boltzmann constant ($5.67 \times 10{-}8$ J/s·m^2·K^4), A is the surface area of the object, and T is the absolute temperature in kelvin. The symbol e represents the emissivity of the object, which is a measure of radiation absorptivity.

1.5.4 Thermal Conductivity

Thermal conductivity is a property that reflects the rate of heat flow through a material. The SI unit for thermal conductivity is watts per meter kelvin (W/mK). It is a function of the materials' density, thermal diffusivity, and specific heat capacity. Since density and thermal diffusivity are temperature dependant, the thermal conductivity of the material changes with temperature. The thermal conductivity of a material can be calculated using the following equation (4).

$$k = \rho \alpha C_p \tag{4}$$

Where, ρ, α, and C_p are the density, thermal diffusivity and specific heat capacity of the material respectively.

There are several methods to measure the thermal conductivity of a material. The oldest method of measuring thermal conductivity is the guarded hot plate method. As shown in Figure 5, the test specimen is placed between a heated plate and a cold plate. The heated plate is insulated using a guard ring and heat can only transfer through the sample. The heated plate supplies a constant heat flow through the sample. Once the system reaches an equilibrium temperature state, the temperature gradient, thickness, and surface area of the sample are used in equation (4) to calculate the thermal conductivity of the material. This method is primary used for low thermal conductive materials and slow, time-consuming test [21].

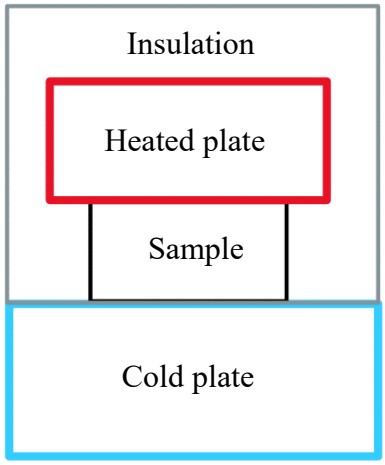

Figure 5: Schematic of the guarded hot plate method utilised to measure thermal conductivity

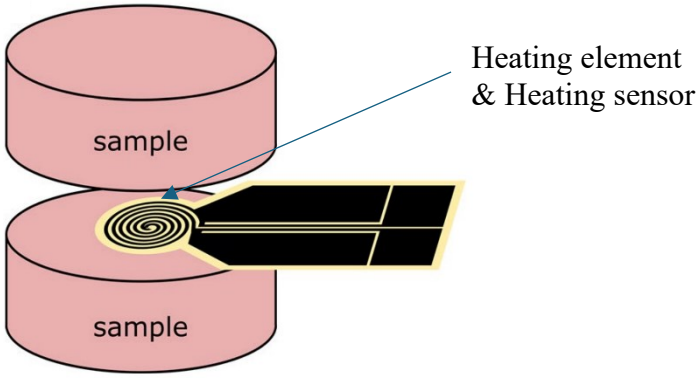

Figure 6: Transient plane source schematic [22]

The Transient Plane Source (TPS) or Modified Transient Plane Source (MTPS) method can also be used to measure thermal conductivity of a material. As shown in Figure 6, the sample is placed on a disc shaped heating sensor that acts as both a heat source and thermometer. The heating element applies a burst of heat into the material, and the temperature response is measured as the sensor returns back to its initial state. The rate at which the temperature falls is then utilized to calculate the thermal conductivity of the material.

Laser flash analysis (LFA) is also a common method of calculating thermal conductivity by measuring the thermal diffusivity of a prescribed material. LFA utilizes a laser beam to

apply a pulse of energy on one side of a specimen and then monitors the temperature rise of the material with respect to time to measure the thermal diffusivity. Additional details on LFA technique are presented in section 1.5.8 Thermal Diffusivity.

1.5.5 Density

Density represents the mass of a unit volume of a substance. The SI units for density are kg/m^3. For simple geometries such as cubes or cylinders, the volume can be measured using calipers. For complex geometries Archimedes' principle can be used to measure volume by submerging the sample in a liquid and measuring the change in volume. Porosity reduces the density of the material, which concomitantly reduces its thermal conductivity. Therefore, for AM components, it is important to optimize print parameters to obtain a high relative density to maximize thermal conductivity.

The density of a sample can be calculated by the following equation (5). Where, m and V are the mass and volume of the sample respectively.

$$\rho = \frac{m}{V} \tag{5}$$

1.5.6 Thermal Expansion

Thermal expansion is the change in the dimensionality of a material due to change in temperature. When the temperature is increased the kinetic energy of the atoms increases and the atoms vibrate. This results in a larger separation between the atoms thus resulting in thermal expansion.

The thermal expansion can be calculated using the following equation (6).

$$\Delta L = \alpha_L L_0 \Delta T \tag{6}$$

Where, α_L, L_0, and ΔT represents the coefficient of thermal expansion (CTE), initial length of the sample, and change in temperature respectively.

The CTE is a function of change in length and change in temperature, and its SI unit is inverse kelvin (1/K). The CTE of the material can be measured using a dilatometer, where the sample is placed in a furnace and heated to a specific temperature and then its thermal expansion is measure mechanically, optically, or through energy intensity measurement systems.

The advantage of optical and laser dilatometry is that they both provide a non-contact measurement. Therefore, the sample does not experience any forces during the experiment that may skew the results. Additionally, soft samples or samples that melt during the experiment would not distort due to external forces.

In an optical dilatometer, a camera is used to measure the expansion via the change in pixels. A laser dilatometer measures the interference of two reflected laser beams with one of the beams reflecting off the sample and the second reflecting off a reference plane next to the sample as shown in Figure 7. The interference beam's intensity is used to calculate the expansion of the sample.

Pushrod dilatometers are the most common method for CTE measurement as the equipment is cheaper than optical or laser dilatometers [23]. As shown in Figure 8, a pushrod is positioned in contact with the test sample in the furnace. When the sample is heated, its thermal expansion pushes against the pushrod displacing it from its starting position. The pushrod translation is measured using a capacitive sensor or an optical encoder to calculate the CTE of the sample.

The furnace temperature and pushrod displacement must be calibrated frequently to ensure accurate readings. The temperature is calibrated using high purity samples such as tin, zinc, or silver, where the sample is heated to its melting point. The melting point of the sample can be identified by the abrupt drop in thermal expansion by the pushrod. The melting temperature of the sample is then compared with the reference melting point of the sample to calibrate the furnace. The pushrod displacement is calibrated by using a reference sample with known CTE values, such as a crystal of sapphire.

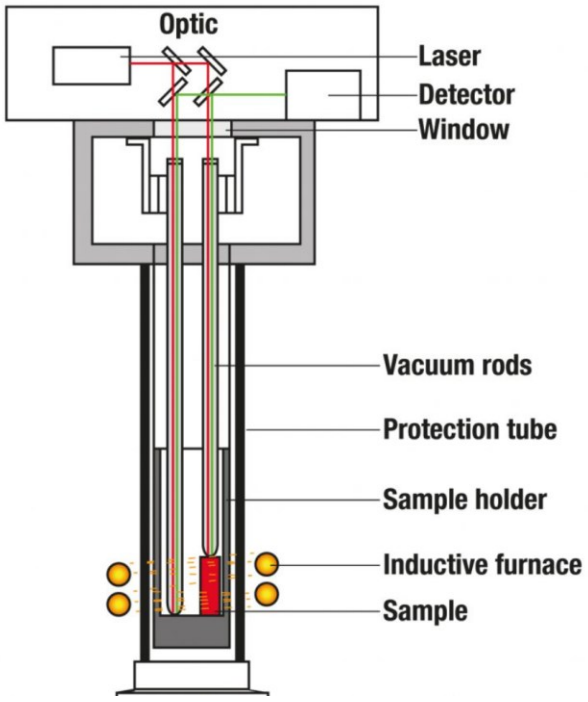

Figure 7: laser dilatometer schematic [24]

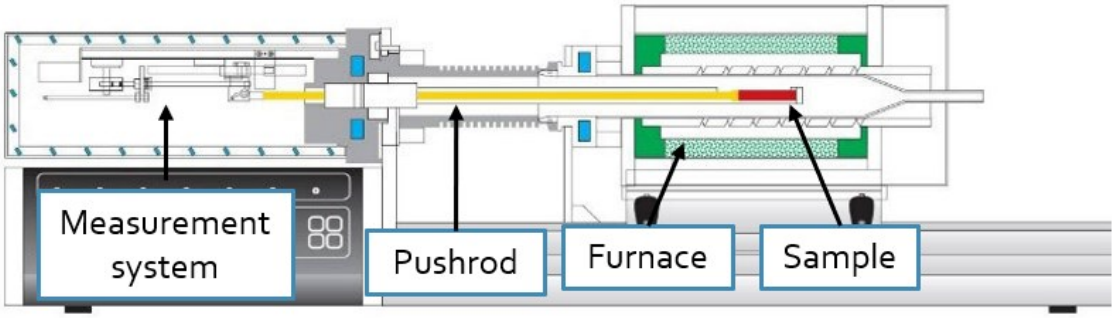

Figure 8: Pushrod dilatometer schematic [25]

1.5.7 Specific Heat Capacity

Specific heat capacity represents the amount of energy required to increase the temperature of 1kg substance by 1 degree. This is commonly measured using a differential scanning calorimeter (DSC) and is reported in joule per kelvin per kilogram (J/K · kg). Since specific heat is a measure of energy and temperature, the temperature and heat flow of the DSC must be calibrated. The temperature mode of the instrument is calibrated occasionally as

heat capacity does not rapidly change with time; however, the heat flow must be calibrated frequently. The heat flow is calibrated using a synthetic sapphire disk with a known specific heat capacity [26]. A baseline test is run with an empty crucible to remove noise generated by the DSC itself. Then the sample is tested to measure and calculate specific heat capacity. The specific heat capacity can be calculated using the following equation (7).

$$C_{p(s)} = C_{p(st)} \cdot \frac{D_s \cdot \mathrm{W}_{st}}{D_{st} \cdot \mathrm{W}_s} \tag{7}$$

Where, $C_{p(s)}$, and $C_{p(st)}$, are the specific heat capacity of the sample, and the sapphire specimen respectively. The symbol D_s represents the vertical displacement between the empty crucible and the specimen on the DSC thermal curve, D_{st} is the vertical displacement between the empty crucible and the sapphire specimen on the DSC thermal curve. The symbols W_s, and W_{st} are the mass of the sample and the sapphire specimen respectively.

1.5.8 Thermal Diffusivity

Thermal diffusivity represents the rate of temperature change due to heat propagation. The SI unit for thermal diffusivity is meter square per second (m^2/s). It is typically measured using the laser flash analysis (LFA) method. As shown in Figure 9, a laser is used to apply a pulse of energy into a sample, and the temperature change over time is measured at the opposite side of the sample using an infrared detector. To maximize the energy absorbed by the sample, a thin layer of graphite is applied to the sample. Furthermore, the sample can be heated to test its thermal conductivity at a specific temperature. However thermal expansion must be taken to account at high temperatures as the thickness of the material increases as the temperature is increased. The time it takes to reach the halfway point of

the resulting temperature profile graph is then used to calculate the thermal diffusivity of the material.

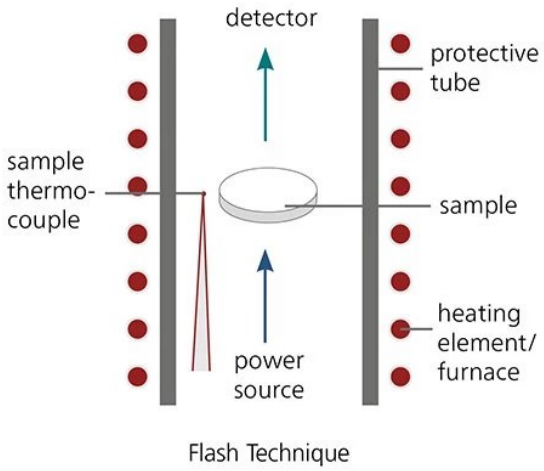

Figure 9: LFA schematic [27]

The thermal diffusivity of the material can be calculated using the following equation (8).

$$\alpha = \frac{0.1388d^2}{0.5t} \tag{8}$$

Where, d is the thickness of the sample and 0.5t is the time to reach the halfway point of the maximum temperature recorded after the energy pulse is applied.

The typical test specimen for an LFA test is approximately 10 to 12.5 mm circular or square disk. The thickness of the specimen depends on the sample, typically 1 to 6 mm, and should be chosen to reach a halfway point of the maximum temperature within 10 to 1000 ms. Thinner samples are recommended at higher temperatures as it minimizes heat loss correction [28].

1.6 Fundamental Concepts in LPBF AM

1.6.1 Basic elements of an LPBF system

Laser Powder Bed Fusion (LPBF), also known as Selective Laser Melting (SLM) or Direct Metal Laser Sintering (DLMS), is a metal AM technology that uses a high-power laser to selectively melt regions of sequentially applied metal powder layers to fabricate three-dimensional (3D) objects [29]. As shown in Figure 10, LPBF works by first spreading a thin layer of metal powder on a build platform. A laser then selectively melts and solidifies the cross section of the part. The build plate then lowers slightly, a new layer of powder is recoated onto the build volume, and the laser melts the next layer of the component. This layer-by-layer fabrication is repeated until the entire part is built.

The core variables related to LPBF are laser parameters, layer thickness, powder characteristics, and atmosphere control. Laser parameters such as laser power, scan speed, hatch distance, and scan strategy play a crucial role in optimizing bulk properties of the printed part. Powder characteristics include material composition, particle size distribution, and particle shape. Layer thickness refers to the height of each powder layer spread on the build platform. Thinner layers can lead to higher resolution parts and better surface finish but increase the build duration. Atmosphere control refers to the maintenance of the build chamber atmosphere, where an inert gas is utilized to maintain oxygen level below a specified threshold and also adjust the gas flow rate over the powder bed for spatter control.

The feedstock powder for LPBF can be spherical or irregular in shape. Spherical powder is commonly used due to its high flowability compared to irregular shaped powder particles. The spherical powder is typically manufactured through a process called gas atomization, in which molten metal is dispersed into fine droplets by a high velocity gas stream. This rapid cooling process results in fine spherical particles, which then get sieved into the required particle size distribution for LPBF.

To prevent oxidation and contamination during the melt process, the build chamber is purged with an inert gas such as Argon or Nitrogen before the build initiation. The build is then processed in a slightly positive pressure of this inert gas. Gas pressure, flow rate,

and oxygen level within the build chamber are all continuously monitored and maintained within acceptable levels as specified by the quality control specifications.

Residual stress can develop due to the rapid heating and cooling cycles present in melting and solidifying the metal powder. The thermal gradients cause expansion and contraction of the material leading to internal stresses that can manifest distortion in the finished part in the absence of appropriate counter-measures. For instance, optimized print parameters and scanning strategies can help reduce residual stresses. Additionally, a heated build plate can also significantly reduce the residual stress development during the print process [30]. The heated build plate reduces the thermal gradient, leading to more uniform cooling and solidification, which also improve the overall dimensional accuracy and mechanical properties of the printed part. Post build heat treatment can also reduce residual stress present within the printed part. It is common to conduct a post build heat treatment before the printed parts are removed from the build plate, to reduce the distortion effects from residual stress.

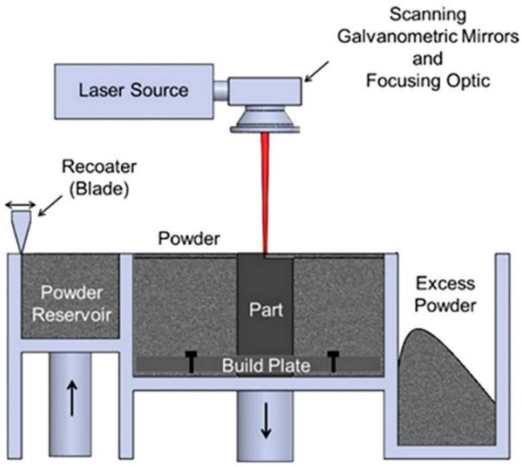

Figure 10: Schematic of a LPBF system [31]

LPBF remains the leading industrial AM technology, as 40% of machine sales revenue is attributed to metal LPBF, while ~10% is derived from polymer LPBF machines [32]. LPBF's popularity can be attributed to its ability to fabricate components of a complex geometry and relatively high resolution compared to other metal AM technologies. A common use for LPBF is rapid prototyping, as the need for expensive

tooling and fixturing is effectively eliminated, which is ideal for custom or small-batch productions.

Theoretically, any metal alloy powder can be utilized in LPBF, but in practicality, not all metals can be processed into a defect-free product. The development of cracks, porosity, and distortion are defects in LPBF that preclude the use of certain alloy systems. Alloys based on the aluminum silicon (Al-Si) binary system represent one class of alloys known to be particularly responsive to LPBF processing [33]. Al-Si alloys have a high fluidity in the liquid phase, are readily weldable, and solidify over a narrow temperature range which facilitates the printing of pore-free specimen. Most work on Al-Si systems involves the alloy AlSi10Mg which contains 10 wt.% silicon and 1 wt.% magnesium. Silicon plays an important role in enhancing mechanical properties of the alloy, through solid solution strengthening and precipitation hardening. Silicon crystals also act as a nucleation site for the formation of primary aluminum grains resulting in a refined grain structure that enhances tensile strength and ductility. Moreover, the high thermal conductivity of Al-Si enables rapid cooling rates resulting in a fine microstructure while alloying Mg into Al-Si enables the precipitation of Mg_2Si, which strengthen the alloy without compromising other mechanical properties [33].

The rapid cooling rates and layer-by-layer fabrication of LPBF often results in anisotropic mechanical properties in the build and transverse directions due to a directional grain structure. Notably, this anisotropy extends to the thermal conductivity of the material as well and must be considered when thermal performance is of concern. Selo et al. [34], have demonstrated that post-build heat treatment processes increase the thermal conductivity of solid AlSi10Mg specimens. Heat treatment processes such as annealing, solution heat treatments, and aging resulted in increased thermal conductivity and eliminated the anisotropy in thermal conductivity present in the as-built specimens (Figure 11). Furthermore, the post processed specimens aligned in thermal conductivity with the cast material standard DIN EN 1706:2010. The change in microstructure was seen to have a direct influence on the thermal conductivity. As shown in Figure 12, the scanning electron microscope (SEM) images of the as-printed microstructure had an anisotropic silicon configuration between the xy and yz-plane. Conversely, the heat-treated specimens

displayed a uniform silicon distribution between the two sectional planes resulting in the isotropic thermal conductivity. Heat treatment also disrupted the silicon network structure into coarser aggregates that enhances heat transfer through the aluminum matrix. Given its desirable response to LPBF and advantageous mechanical and thermal properties, Al-Si alloys are now utilized in a growing number of AM applications in the automotive, aerospace, and energy sectors.

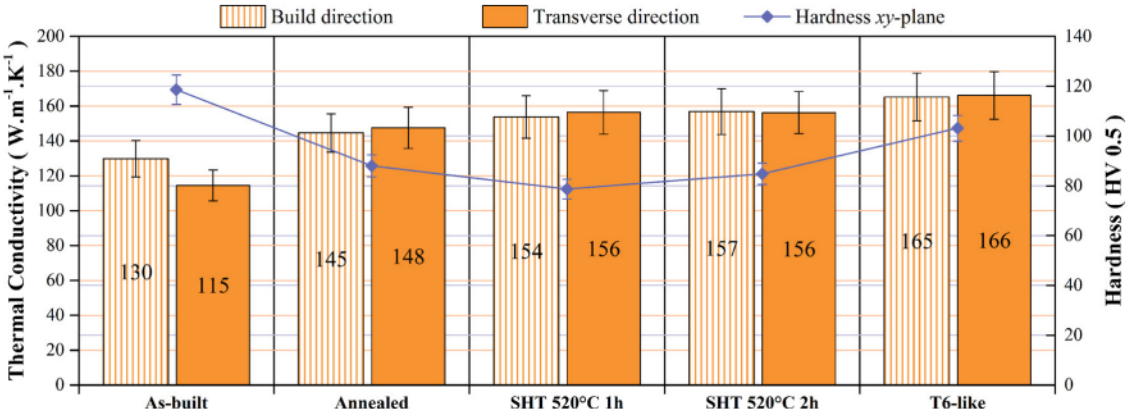

Figure 11: Thermal conductivity of solid specimens before and after heat treatment [34]

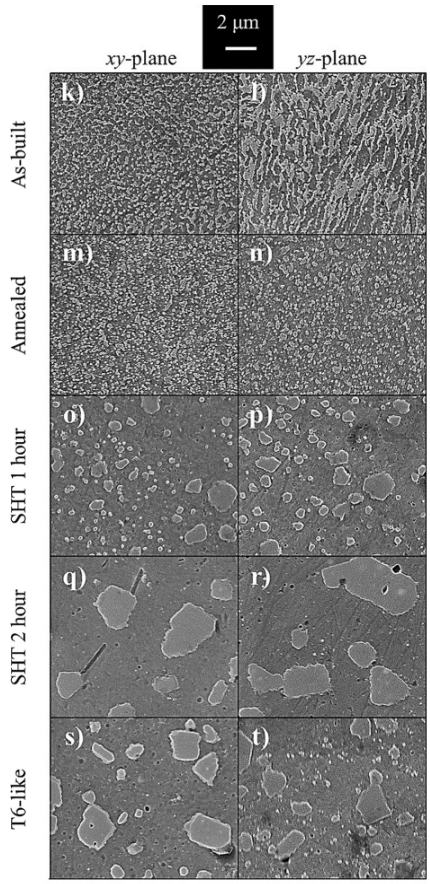

Figure 12:SEM images of AlSi10Mg microstructure after different heat treatments. light grey represents Si-rich areas, and dark gray represents Al-rich areas [34].

1.6.2 Effects of Powder-related Parameters

The packing density of the powder bed has a significant impact on the final density of the printed part [35]. Factors that influence the packing density are particle size, shape, size distribution, agglomeration tendency, etc. Spherical powder particles pack together more efficiently compared to irregularly shaped powder as the latter manifest a higher degree of inter-particle friction that lowers flowability and invokes inconsistencies in spread layer thickness. Smaller powder particles can create a high packing density, but when they become too fine, they tend to agglomerate as the force of attraction between the particles increases with the reduction of size. Thus, the powder particles can clump together dragging adjacent particles with them as shown in Figure 13. Notably, ambient humidity can also cause the powder to agglomerate [36].

Figure 13: Effects of agglomeration on a spread layer of powder in an LPBF system

1.6.3 Effects on Laser-related Parameters

Laser-related parameters for LPBF include laser power, scan speed, hatch spacing (distance between consecutive laser scan paths), and layer thickness. These parameters are used to calculate the energy density input per unit volume by the laser. The energy density (E) is calculated using the following equation (9).

$$E = \frac{Laser\ power}{Scan\ speed \cdot Hatch\ spacing \cdot Slice\ thickness} \tag{9}$$

Increasing or decreasing the input energy density from an optimum setting can lead to an increase in the amount of porosity in the printed product. A relatively low energy density produces lack of fusion porosity, while an excessively high energy density can produce gas-trapped pores. The type of porosity can be identified by the shape of the pore as lack of fusion pores tend to be sharp and irregular as shown Figure 14a, whereas gas-trapped pores tend to be spherical in shape as shown in Figure 14b.

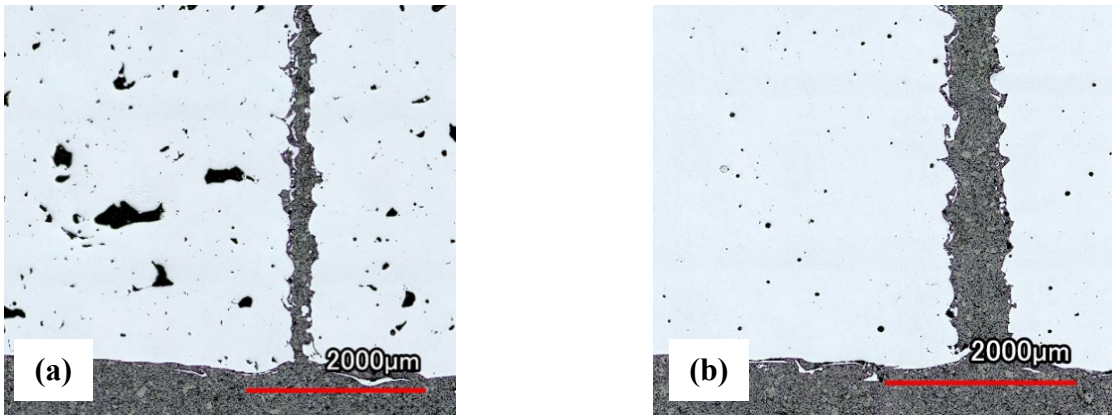

Figure 14: Porosity in LPBF samples.
(a) irregular shaped lack of fusion porosity. (b) spherical shaped gas trapped porosity

1.6.4 Design for AM

AM offers unique advantages over traditional manufacturing methods, including fabricating complex geometry, reducing material waste, part consolidation, on demand manufacturing, and more. To fully leverage these benefits, the design for AM principles should be considered from the beginning of the design process. This ensures that the advantages and constraints are integrated into the design, leading to a component that is optimized for performance, cost efficiency, and manufacture while minimizing the likelihood the defects will be present.

A Practical Guide to Design for Additive Manufacturing by Olaf Diegel et al. [37] outlines several guidelines to consider when designing AM parts. The first is to evaluate the need for AM as in most scenarios, traditional manufacturing methods can manufacture a desired component cheaper and faster. If a compelling business case exists for AM, multiple factors must then be considered. One of which is the need, usage, and design of support structures that restrict deformation of the printed product due to the high residual stresses developed during rapid solidification. Generally, the minimum unsupported overhang angle for LPBF is approximately 45 degrees relative to the build plate. Any surfaces with lower angles would result in poor surface roughness on the downface side as shown in Figure 16. Therefore, selecting a print orientation to minimize the need for support material reduces the cost and labour required to remove supports. In areas where support removal

is challenging or impossible, permanent support structures must be integrated into the design. Ideally the geometry must be modified to eliminate any support structures in hard to machine areas. For example, horizontal holes and channels can be designed to be self supporting with a diamond or teardrop shape (Figure 15). As a general guideline, circular horizontal holes below a diameter of 8 mm can be printed in LPBF without supports [37].

Residual stress can also be problematic at sharp internal and external corners that invoke stress concentrations and at regions where large changes in cross sectional area and/or masses of material transpire. The intensified residual stresses in these regions can lead to cracks and deformation but can be mitigated with optimized design strategies. Simple design solutions include rounding sharp edges, reducing large masses, and eliminating uneven thicknesses. Preheating the build plate is also an effective tactic for lessening residual stress as it reduces the solidification rate and invokes modest degree of in-situ annealing during the build cycle itself.

The cost of an AM part is driven by many factors including the print time itself which can be on the order of days, the amount of raw powder material needed, the number and nature of post-build processing steps, and labour. Addition of useful cosmetics such as logos, instructions and part number in the print model, does not significantly change the print duration, thus the cost remains relatively the same. These additions to the model can aid in identifying the product brand, keep track of stock, and aid in assembly.

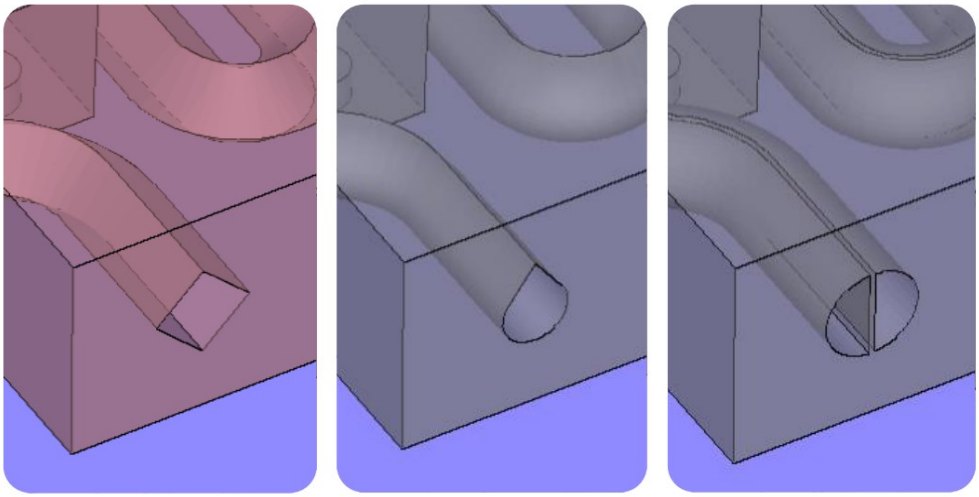

Figure 15: Design concepts for the printing of horizontal channels using LPBF [38]

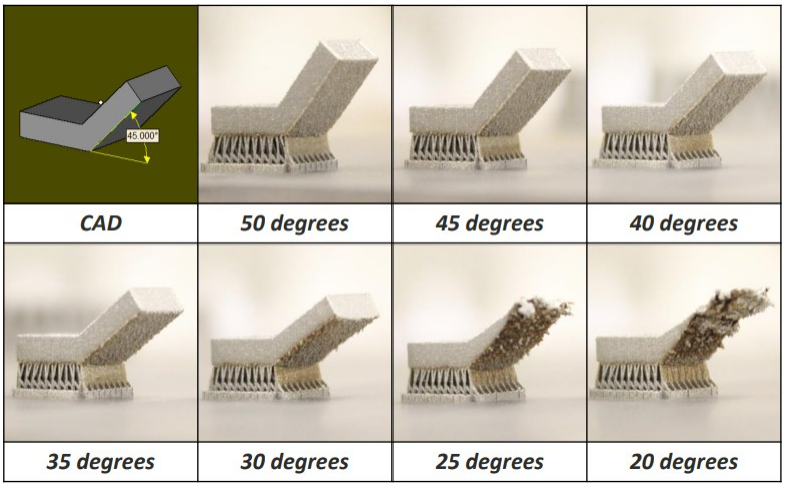

Figure 16: Effects of unsupported angles [38]

1.7 AlSi10Mg Material Properties

The AlSi10Mg powder used in this project is provided by Equispheres. Their performance line of Al-Si was acquired, and it is optimized for part strength. The chemical composition of the powder is shown in Table 1;

Table 1: Chemical composition of AlSi10Mg

Element	Weight %
Al	Balance
Si	10.0
Mg	0.35
Fe	0.04
Ti	0.01
Cu	0.01

1.7.1 Powder Size Distribution

A powder size distribution (PSD) analysis was conducted at Dalhousie's Minerals Engineering Centre. The PSD measures the powder particles' sizes and the particle size frequency in a powder sample. Figure 17, displays the particle size, frequency, and cumulative volume distribution of a sample of the AlSi10Mg powder used in this study that was found to have an average (D50) particle size of 53 µm as well as 10% (D10) and 90% (D90) passing sizes of 38 and 72 µm respectively.

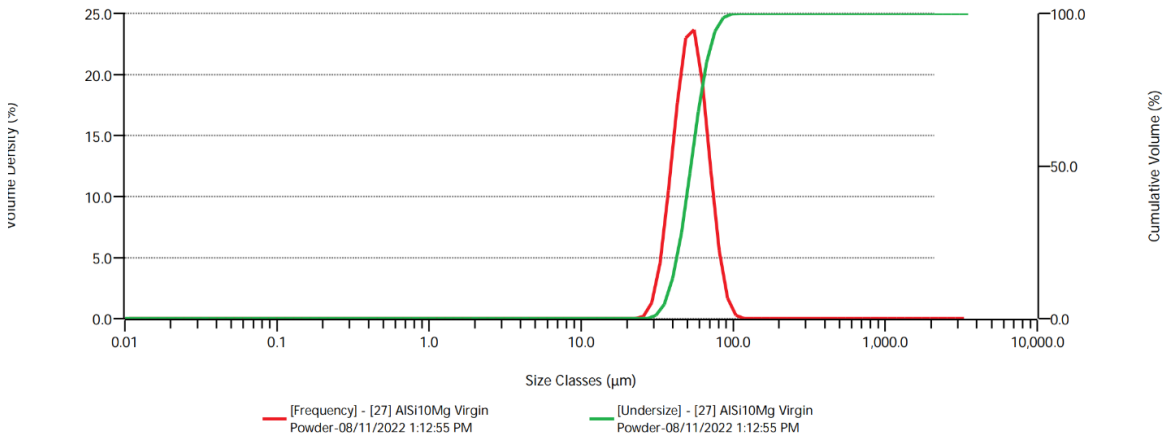

Figure 17: Frequency and cumulative % finer size distributions of AlSi10Mg powder.

1.7.2 Apparent density

Apparent density represents mass of loose powder per unit volume. This is useful when setting up a LPBF build to estimate the amount of powder required for the build. Apparent density was measured using the Arnold density meter shown in Figure 18, which slides loose powder into a cylinder of known volume (20 cm^3), and measures the mass of the powder in the volume to calculate apparent density using Equation (10). The AlSi10Mg powder was tested five times, and the average apparent density was calculated to be 1.50 g/cm^3.

$$Apparent\ Density = \frac{Arnold\ measuring\ method\ mass}{cyclinder\ volume} \quad (10)$$

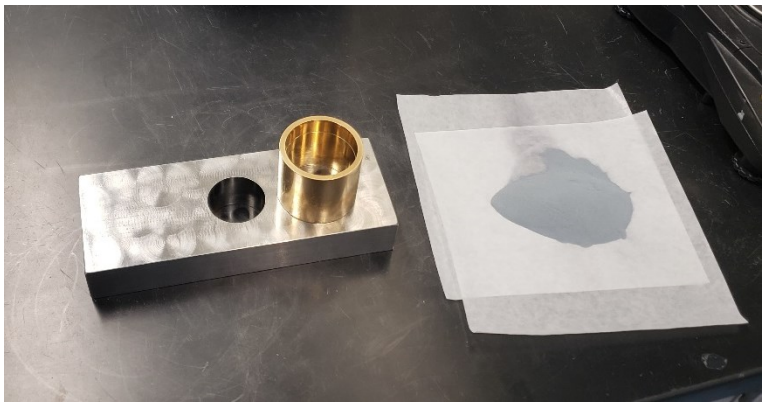

Figure 18: Arnold density measurement apparatus

1.7.3 Tap density

Tap density represents the density of gently packed metallic powder. This was measured by pouring 20g of metal powder into a 25ml graduated cylinder and vibrating the cylinder for approximately 4 minutes on a vibration plate and then measuring the volume of the powder in the graduated cylinder. The AlSi10Mg powder measured a tapped density of 1.586g/cm^3.

1.7.4 Flow rate

The flow rate was measured using a Hall flowmeter shown in Figure 19 with a 0.1" orifice. The hall flowmeter was filled with 20g of powder, and the time required to empty the powder through the orifice was measured to calculate the flow rate. The test was conducted six times to obtain an averaged flow rate of 1.34g/s.

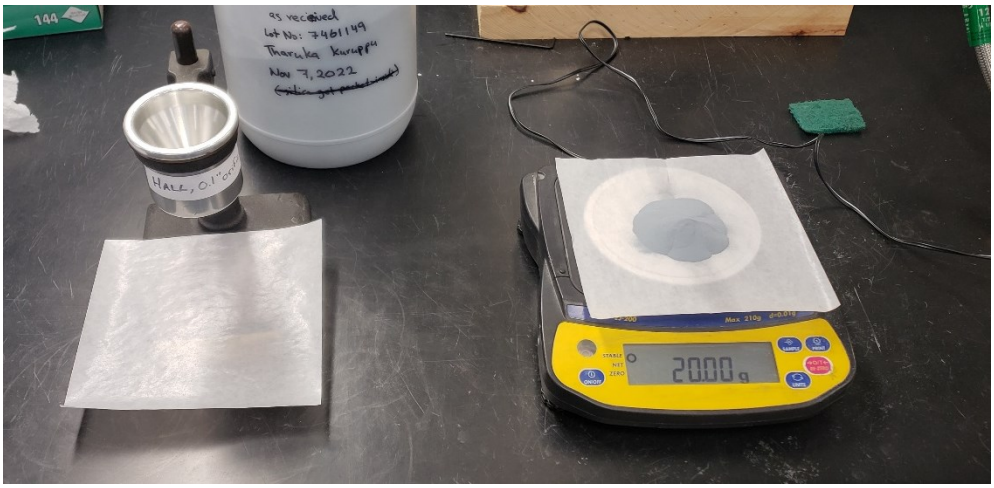

Figure 19: Hall flow meter apparatus

1.7.5 Helium Pycnometry

Helium pycnometry is a precise technique of measuring density of solid materials. It measures the volume of the sample by measuring the displacement of Helium gas. Helium gas is utilized for it small atomic size, which allows it to penetrate fine pores within the surface of the sample, ensuring an accurate volume measurement. The volume of the sample is calculated using Boyle's law (Eq (11)). The sample is placed on to a chamber with known volume and purged with Helium gas. Then test chamber is opened to another chamber with know volume, and the pressure difference and volumes of the chambers are used to calculate the volume occupied by the test specimen.

$$P_1V_1 = P_2V_2 \tag{11}$$

A sample of the AlSi10Mg powder was used to measure its density. Three test samples were extracted and tested, and the test results are shown in Table 2. The helium pycnometry results show that the average density of the solid AlSi10Mg particles was 2619 kg/m^3.

Table 2: Helium pycnometry results of AlSi10Mg powder sample

Sample ID	Mass (g)	Temp (°C)	Density g/cm^3	StDev (g/cm^3)
AlSi10Mg	2.6786	25.600	2.620	0.001
AlSi10Mg	2.6786	25.700	2.618	0.001
AlSi10Mg	2.7871	25.100	2.619	0.001

1.7.6 Laser Flash Analysis of AlSi10Mg

LFA analysis of AlSi10Mg was conducted to measure the thermal diffusivity of the material and calculate its thermal conductivity. Five LFA test specimens were printed in an Aconity mini LPBF machine using recommended print parameters from the material provider (Equispheres) and machined to 10x10x3 mm rectangular plates as per American Society for Testing and Materials (ASTM) standard E1461 – 13 (Appendix A).

The thermal diffusivity of each sample was determined using a Netzsch LFA 427 device (Figure 20) located at the High-Temperature Thermal Analysis Laboratory at Dalhousie University. The thickness of each sample was measured at room temperature. Since the test was conducted at room temperature, thermal expansion of the material was not a factor in determining the thermal diffusivity. To ensure maximum energy absorption from the laser pulse, a thin layer of graphite was sprayed on each side of every sample.

Five laser pulse shots were run on each sample, and the mean temperature and thermal diffusivity were measured. The summary of the LFA results are graphed in Figure 21. Excluding the outlier observed in sample 5, the nominal thermal diffusivity of AlSi10Mg was measured to be 45.19 mm^2/s. Utilizing this value, the thermal conductivity of AlSi10Mg was calculated to be 117 W/mK.

Figure 20: Netzsch LFA 427 system

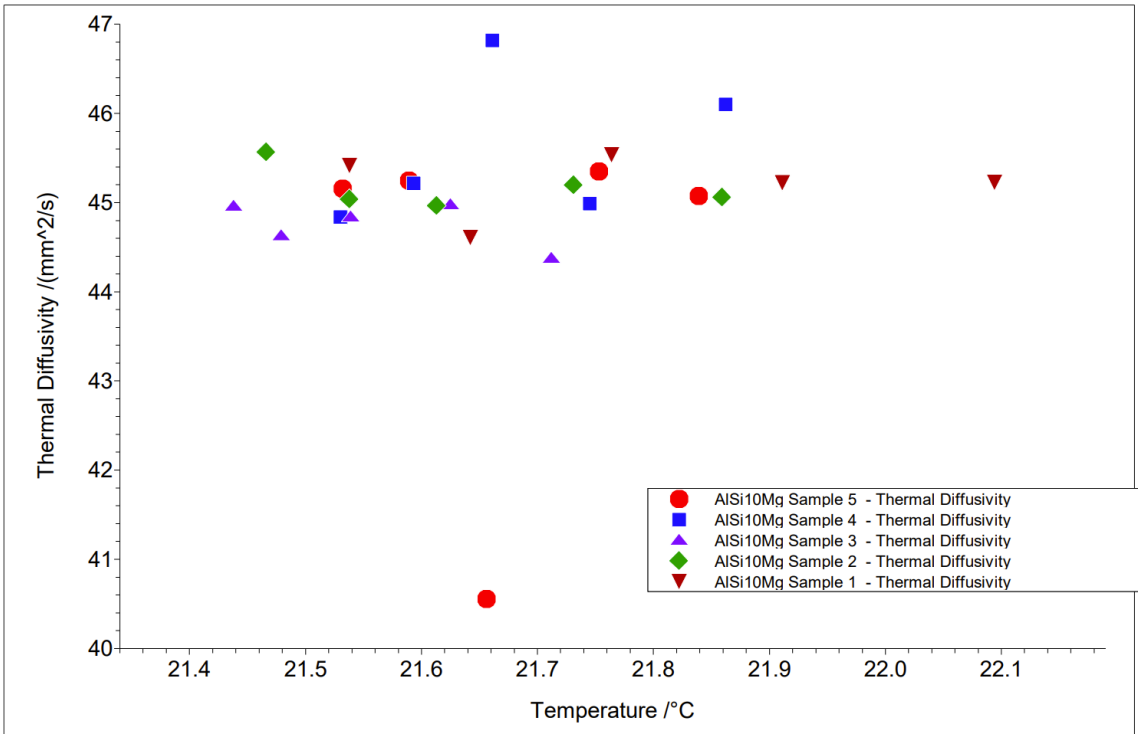

Figure 21: LFA results

1.7.7 AlSi10Mg Density

To calculate the density of AlSi10Mg, five density specimens were printed and tested. The density specimens were printed on the Renishaw RenAM 500S flex LPBF machine, using the recommended print parameters for AlSi10Mg provided by Renishaw. Additional information regarding the LPBF machine is presented in section 4.1. The specimens were 10x10x10 mm cubes with a 45-degree chamfer at the bottom (Figure 22), to facilitate easy part removal from the build plate.

Figure 22: AlSi10Mg Density Specimens

The density of each specimen was measured using the Archimedes oil infiltrated density measurement method. Initially, the mass of each sample was measured in a dry state. The samples were then submerged in oil under vacuum for one hour to ensure that surface-connected pores were fully infiltrated with oil. After this, the mass of each sample was measured again in air and while submerged in water. These mass measurements were used to calculate the density of each specimen using equation (12).

$$\rho_{specimen} = \frac{m_{dry} \times \rho_{water}}{m_{oil} - m_{water}} \tag{12}$$

The average density of the AlSi10Mg specimens was found to be 2.61 g/cm³. This material property was used in the numerical simulations conducted in this research to ensure that the simulations align with the AlSi10Mg heat exchanger printed.

Chapter 2 Reverse Engineering and Redesign of an Aerospace Heat Exchanger for LPBF

2.1 Reverse Engineering the Conventional Heat Exchanger

Reverse engineering of the conventional heat exchanger was the first step in the development of an AM-based counterpart. This included an accurate assessment of the physical shape of the conventional unit and understanding how it functioned in service. Initially, a digital model of the traditional heat exchanger was established to extract dimensional and positional information on critical features of the geometry. Here, 3D laser scanning was utilized to obtain a point cloud of the device as shown in Figure 23(a). The geometry was captured using a Hexagon Romer Absolute Arm Compact, with a HP-L-8.9 laser scanner attachment and translated into a point cloud using Hexagon PC-DMIS software. To best capture the geometry, the laser exposure levels were adjusted appropriately, and multiple overlapping scans from different angles were captured. This point cloud was referenced to then create a complete computer-aided design (CAD) model, as shown in Figure 23(b). The point cloud was exported into SolidWorks, and then sketches were drawn referencing the point cloud to create the CAD model. A coordinate measuring machine (CMM) was then employed to capture higher resolution data on all critical features including the locations of fluid inlets and outlets as well as mounting holes shown in Figure 24. To measure the internal geometry of the inlets and outlets, a negative of each feature was molded using Reprorubber quick setting putty (Figure 25a). A Mitutoyo PH-A14 profile projector was then utilized to measure the profile of each negative at a higher resolution, as shown in Figure 25(b). This method enabled the accurate measurement of chamfer angles and fillets (Figure 26) which would otherwise be challenging to assess. Measurements from the profile project, were then used to update the CAD model and develop complete engineered drawings of the inlets and outlets.

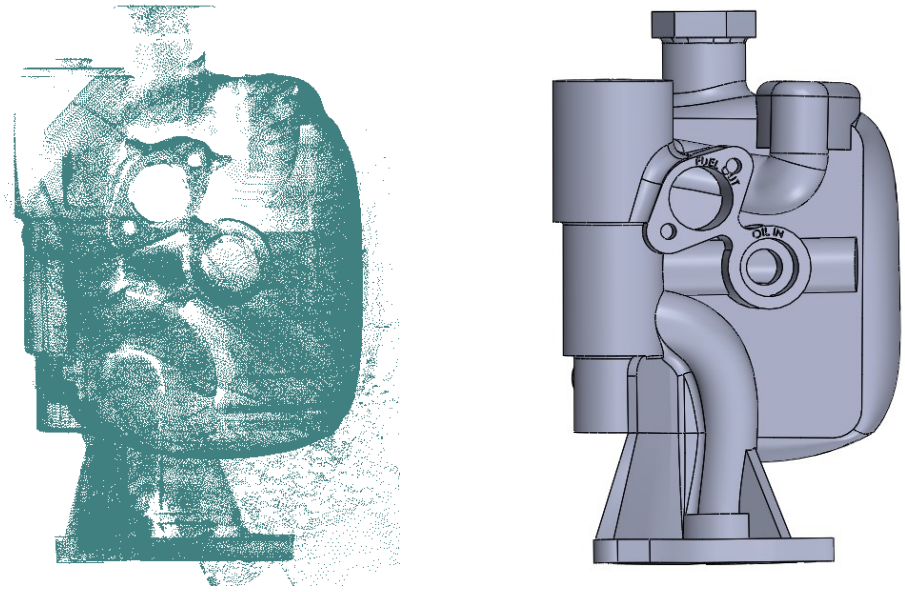

(a) Point cloud data from the laser

(b) CAD model of the Traditional heat exchanger

Figure 23: Development of the traditional heat exchanger CAD

The internal structure of the heat exchanger was then examined by sectioning the unit with a band saw (Figure 27). This revealed that the core was premised on a two-pass serrated extended surface concept, where the fuel and oil pass perpendicular to each other. It also confirmed that the core was manufactured by brazing stamped sheet metal strips and then welding it onto the casted body. Sectioning also enabled a complete view of the thermally regulating valve region facilitating accurate measurement and examination of its internal geometry (Figure 28). The valve itself was an integrated sub-assembly designed to maintain the fuel temperature below a specified threshold by regulating the flow of hot oil into the heat exchanger core. When the fuel temperature exceeded the specified temperature threshold, the oil channel to the heat exchanger core would be obstructed to thereby reduce hot oil flow into the core. This would then reduce the heat transfer within the core to regulate the fuel temperature. The geometry of the valve housing was quantified using caliper measurements of the internal diameters and depths of each section as well as the thread depths and diameters. Additionally, thread gauges were employed to measure the pitch of all threads. The corresponding threads for the AM heat exchanger were then selected based on these measurements.

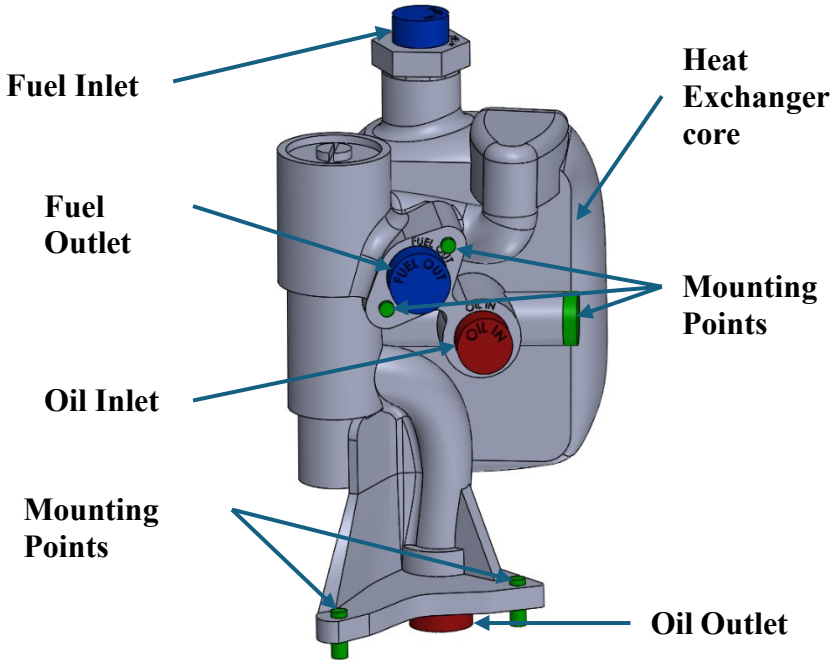

Figure 24: Critical features of the Heat exchanger

(a) Negative molds of the inlets and outlets

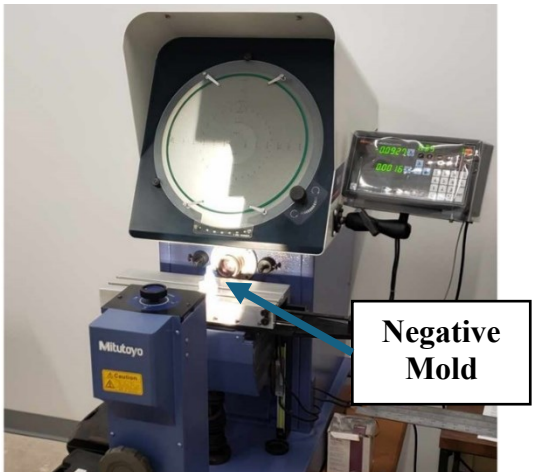

(b) Negative mold in the profile projector machine

Figure 25: Profile Projector technique utilized to measure the inlets and outlets

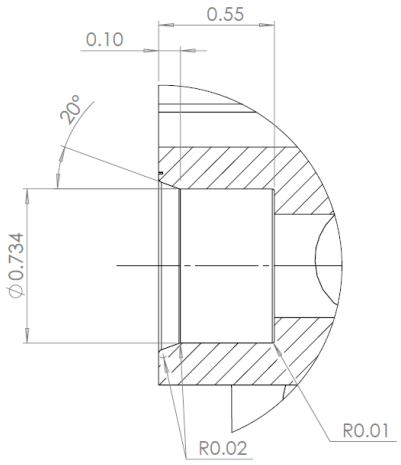

Figure 26: Engineered drawing data acquired from the profile projector

(Dimensions are in inches)

(a) Oil flow path (b) Fuel flow path

Figure 27: Sectional cut outs of the heat exchanger core

Figure 28: Sectional cut out of the thermal regulating valve area

2.2 AM Heat Exchanger Overall Geometry

The AM heat exchanger was designed using SolidWorks and nTop. SolidWorks was used to parametric define the overall geometry of the heat exchanger and nTop was used to design and integrate the lattice with the overall geometry. The lattice was designed in nTop, due to its implicit modeling capabilities, which enables the software to create complex structures that are difficult to model in parametric design software.

The first step in designing the AM heat exchanger was to identify critical features that are essential to be replicated for its functionality and compatibility with existing aircraft engines. The inlets, outlets, and mounting points geometry and position shown in Figure 24, were referenced from the traditional heat exchanger.

Selecting an appropriate bottom surface for the AM heat exchanger is crucial to ensure proper adhesion to the build plate and support subsequent features above it. A wide, flat surface is preferred as it results in a strong adhesion to the build, provides good heat dissipation, and provides a good foundation for building the component with minimal

support structures. In the context of the AM heat exchanger, the oil outlet face was selected as the bottom surface. This is due to the flat surfaces of the oil outlet, along with the two mounting points, which create a robust base. All the other critical features are aligned above it and can be fabricated with minimal support structures.

The temperature-regulating valve system was integrated into the AM design so that it could operate similarly to the traditional heat exchanger. Upon inspecting the valve system from the sectional cut-outs shown in Figure 28, the concentric cylinders features are printable in limited orientations without any support structures. The optimal print orientation was determined to be with the valves parallel to the build direction, to mitigate the use of support structures and eliminate the need for any custom tooling required to post machine these features. Furthermore, chamfers were added to overhanging features shown in Figure 29 to optimize the geometry for LPBF.

For the design of the heat exchanger core housing, an inverse teardrop shape was selected (Figure 30). This shape was selected as the external down skin surface would then be self-supporting and the internal surface would be supported by the lattice as shown in *Figure 31*. The absence of overhanging surfaces simplified the manufacturing process and reduces material waste, as well as the time and effort required for post-processing. Teardrop profile channels were incorporated to connect the heat exchanger core and the temperature regulating valve system. Such profiles were self-supporting and ensured minimal flow disruption compared to permanent supports in the channels, thus minimizing the likelihood of excessive pressure drop in service. Since the fuel inlet to the temperature regulating valve system was located at the top, a two-pass fuel flow configuration was selected to accommodate the design. Similarly, a two-pass configuration was selected for the oil flow within the heat exchanger core. Since the inverse teardrop shape was somewhat symmetrical in the build direction, the oil flow was introduced to the heat exchanger core at the bottom, to minimize poor circulation within the heat exchanger core. Furthermore, an oil drain port was added to the heat exchanger core. The placement of the drain port was strategically positioned to allow drainage when the unit is mounted onto the aircraft engine. Therefore, when assembled the drain port points downwards, ensuring that the oil can be completely removed from the core.

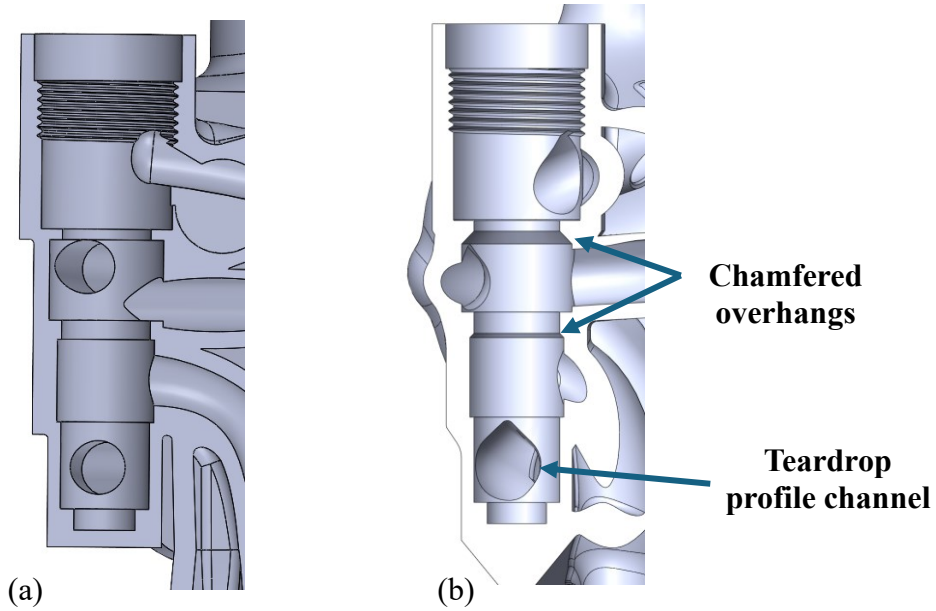

Figure 29: Traditional vs AM thermally regulated valve geometry.
(a) sectional view of the traditional manufactured thermally regulated valve. (b) Sectional view of the AM optimized thermally regulated valve.

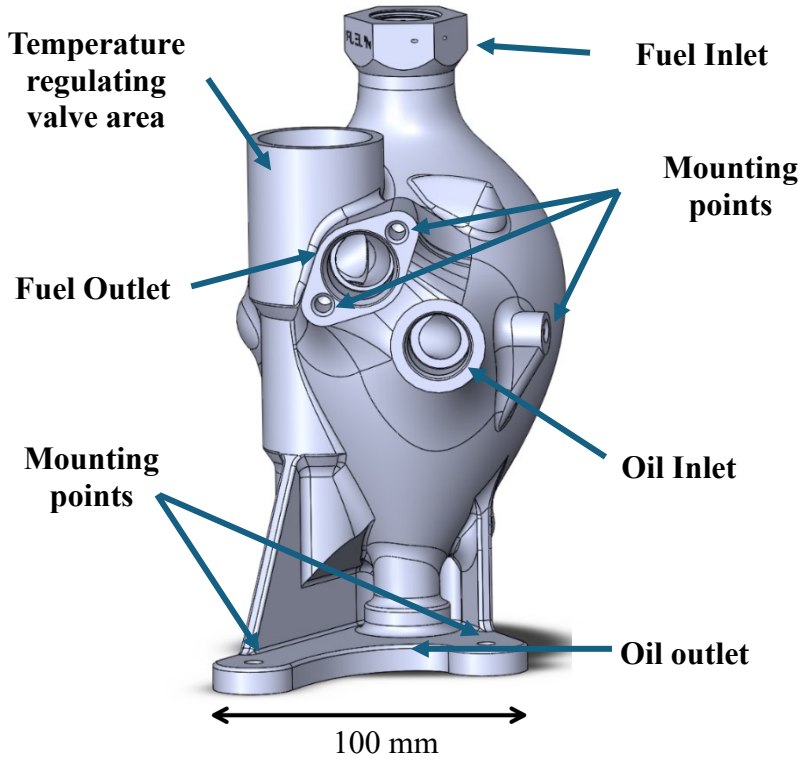

Figure 30: Overall geometry of the AM heat exchanger

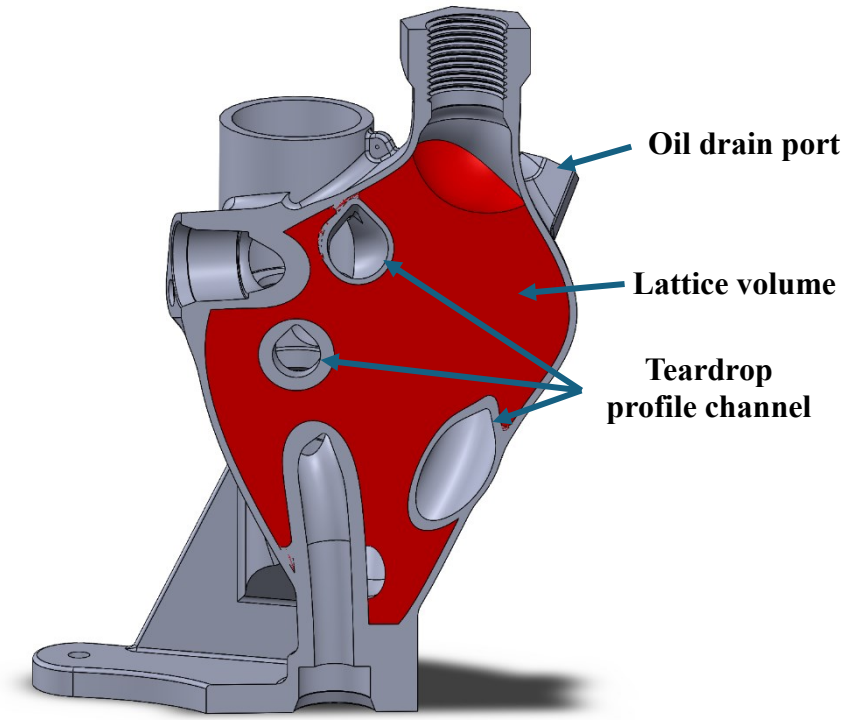

Figure 31: Sectional view of the AM heat exchanger geometry

2.3 TMPS Lattice

Triple Periodic Minimal Surface (TPMS) lattices are a class of surfaces characterized by their continuous, smooth surfaces that extend periodically in three dimensions. The first TPMS was published by H. A. Schwarz in 1865 with the discovery of Schwarz's Diamond (Schwarz D) surface [39]. Experiments with soap films led to the discovery of minimal surfaces, as they naturally form locally minimize surface area for a given boundary. In 1970, Alan Schoen, further explored these surfaces leading to the identification and classification of several types of TPMS structures that are now commonly used in Engineering and material science [39]. Even though these TPMS lattices have been in existence for a long time, their manufacturability is relatively new, as AM, and implicit design software, has only now empowered companies with a capacity to fabricate these complex geometries.

TPMS lattices are generated using implicit mathematical functions to define the surface of the periodic lattice. Common TPMS lattice structures include gyroid, diamond, Schwarz,

Split P, and Neovius surfaces. These surfaces can be defined using the following equations shown in Table 3.

Table 3: TPMS lattice equations

Lattice type	**Equation**	**Eq no.**
Gyroid	$\sin(x)\cos(y) + \sin(y)\cos(z) + \sin(z)\cos(x)$	(13)
Schwarz	$\cos(x) + \cos(y) + \cos(z)$	(14)
Diamond	$\sin(x) \times \sin(y) \times \sin(z) + \sin(x) \times \cos(y) \times \cos(z) + \cos(x) \times \sin(y) \times \cos(z) + \cos(x) \times \cos(y) \times \sin(z)$	(15)
Lidinoid	$\sin(2x) \times \cos(y) \times \sin(z) + \sin(2y) \times \cos(z) \times \sin(x) + \sin(2z) \times \cos(x) \times \sin(y) - \cos(2x) \times \cos(2y) - \cos(2y) \times \cos(2z) - \cos(2z) \times \cos(2x) + .3$	(16)
Split P	$1.1 \times (\sin(2x) \times \sin(z) \times \cos(y) + \sin(2y) \times \sin(x) \times \cos(z) + \sin(2z) \times \sin(y) \times \cos(x)) - 0.2(\cos(2x) \times \cos(2y) + \cos(2y) \times \cos(2 \times z) + \cos(2z) \times \cos(2x)) - 0.4(\cos(2x) + \cos(2y) + \cos(2z))$	(17)
Neovius	$3(\cos(x) + \cos(y) + \cos(z)) + 4\cos(x) \times \cos(y) \times \cos(z)$	(18)

2.3.1 TPMS Lattice Selection

nTop^{TM} software was utilized to design and integrate the lattice into the heat exchanger model. While many lattice possibilities exist, only those that inherently separate the fluid volume into two separate domains (as required for the two fluid heat exchangers of interest) were considered. Lidinoid and Neovius TPMS lattices contain closed volumes, where loose powder can get trapped. Hence, they were immediately eliminated from the list of viable options. For those that remained, surface area to weight ratio and pressure drop properties were compared to select the lattice that was most suitable for the targeted application.

First the surface area to volume ratio was compared. To compare each lattice with each other, the solid volume, lattice wall thickness, and the bounding box of the lattice were equalized between the selected concepts. The bounding box of the lattice was fixed at 20x20x20 mm, the lattice wall thickness at 1 mm, and the solid volume at approximately 2328 mm^3. The lattice unit cell size was varied to obtain a consistent solid volume. The evaluated test specimens are shown in Figure 32. As shown in Table 4, the Diamond TPMS lattice contained the highest surface area to volume ratio, followed by Gyroid, Split P, and Schwarz respectively.

Table 4: Surface area to volume ratio comparison of different TPMS options

Lattice Type	Unit Cell Size (mm)	Surface area (mm^2)	Solid volume (mm^3)
Gyroid	10×10×10	5385	2326
Diamond	12.3×12.3×12.3	5500	2328
Schwarz	8.8×8.8×8.8	4810	2331
Split P	17.2×17.2×17.2	5264	2327

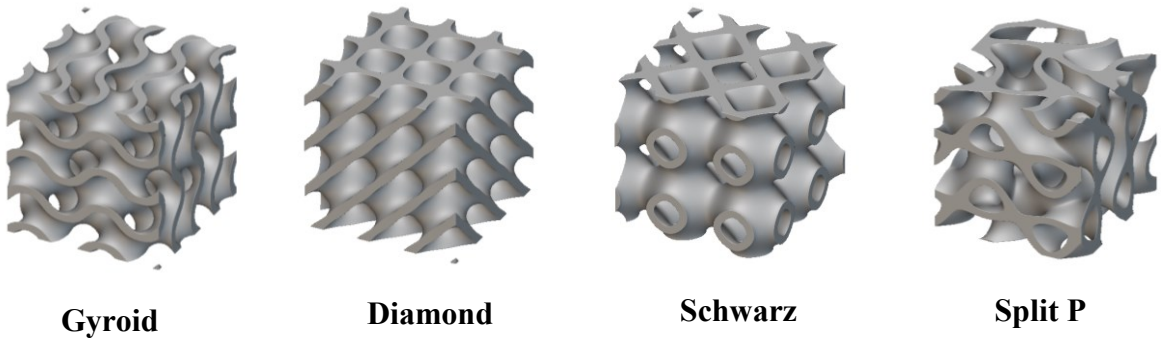

Figure 32 : TPMS lattice options evaluated for AM heat exchanger design.

Furthermore, the pressure drop was also evaluated as it is another critical property that can influence the performance of a heat exchanger. A lower pressure drop is preferred as it would reduce the energy demand on pumps and ensure efficient fluid flow through the heat

exchanger. Each lattice was evaluated by conducting a fluid flow simulation and measuring the pressure drop between the inlet and outlet. For this purpose, a cylindrical test specimen was designed with an inner diameter of 46 mm and a lattice length of 50 mm. The cross section of the test specimens are shown in Figure 33. The simulation was conducted in Ansys Discovery, where an inlet mass flow rate of 0.2 kg/s of water and an outlet pressure of 0 Pa was specified. As shown in Table 5, Diamond lattice resulted in the lowest pressure drop, followed by Gyroid, Split P and Schwarz respectively.

Table 5: TPMS lattice pressure drop simulation results

Lattice Type	Unit Cell Size (mm)	Pressure Drop (Pa)
Gyroid	10x10x10	338
Diamond	12.3x12.3x12.3	265
Schwarz	8.8x8.8x8.8	818
Split P	17.2x17.2x17.2	490

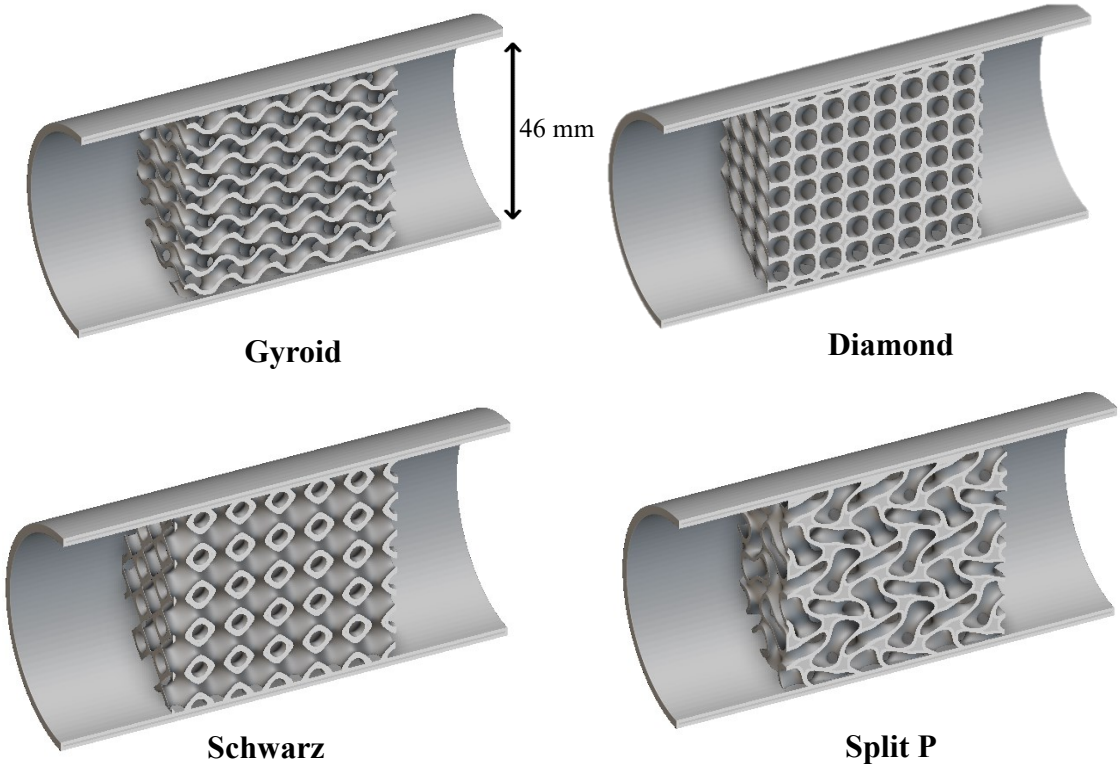

Figure 33: Sectional view of the pressure drop simulation test specimens

Based on the evaluations, the Diamond TPMS lattice was identified as the most suitable for heat exchanger applications. It demonstrated the highest surface to volume ratio, which is crucial for enhancing convection heat transfer and the lowest pressure drop, which would reduce the load on the pumps relative to the other evaluated lattices. Consequently, the Diamond TPMS lattice provides an optimal balance between high thermal performance and low pressure drop, making it the preferred choice for the additively manufactured heat exchanger design.

2.3.2 Lattice Cell Size

Lattice cell size refers to the dimensions of the repeating unit cell. Adjusting the cell size can significantly influence the fluid flow as well as pressure drop and convective heat transfer characteristics. Smaller cell sizes typically increase the surface area but also lead to higher flow resistance. To determine the optimal size, a fluid flow simulation was conducted in Ansys Discovery. The objective was to identify the unit cell size that would result in a pressure drop <24 kPa for the oil domain and <10 kPa for the fuel domain.

The pressure drop can be reduced by increasing the channel size or reducing the waviness of the channel to decrease the resistance to flow. This can be achieved by increasing the unit cell size, which enlarges the cross-sectional area of each fluid path, or by stretching the unit cell in the direction of flow to reduce the waviness of the flow path. Since the fluid flow is predominantly in the build direction, stretching the unit cell in the Z direction reduces the overhang radius, making it more suitable for LPBF processes.

Additionally, the lattice wall can be offset towards one side to further increase the volume in one fluid domain while reducing the volume in the other, as shown in Figure 35. In this case, the lattice wall was offset towards the fuel domain because the fuel has a lower viscosity and a lower pressure drop requirement compared to the oil. This adjustment allows for better management of fluid dynamics and thermal performance, tailored to the specific properties of the working fluids.

The fluid flow simulation utilized the fluid properties shown in Table 10.

From the fluid flow simulation, streamlines were analyzed to identify areas with poor circulation. Poor circulation regions were identified by the lower number of streamlines present in the fluid region. Based on these insights, the baffles that direct the fluid flow within the heat exchanger core were modified as shown in Figure 34, to increase flow coverage, thereby improving the overall fluid circulation. The optimization of the fluid flow through baffles also leads to reduced pressure drop and enhanced performance of the heat exchanger. However, due to the need for supporting critical features and the use of no support material, some regions within the fluid domains still exhibited lower fluid circulation as shown in Figure 37 and Figure 38.

It was also observed that the 10x10x20 mm unit cell size recorded a lower pressure drop in the fuel volume compared to the 10x10x30 mm. The smaller unit cell had better fluid circulation and utilized more of its fluid volume, which enable it to use more flow paths, thereby reducing the overall flow resistance (Figure 36).

As demonstrated in Table 6, a 12.5x12.5x30 mm unit cell size with a 0.5 mm mid-surface offset resulted in a pressure drop within the required limits, thus selecting it for the AM heat exchanger design.

Table 6: Summary of pressure drops modeled for different unit cell concepts

Unit Cell Size	**Oil Domain Pressure drop (Pa)**	**Fuel Domain Pressure drop (Pa)**
10x10x10	44409	8175
10x10x20	29853	7351
10x10x20 – with 0.5 mm offset	25736	13827
10x10x30	27743	9055
10x10x30 – with 0.5 mm offset	24890	15052
12.5x12.5x30 – with 0.5 mm offset	23894	9229

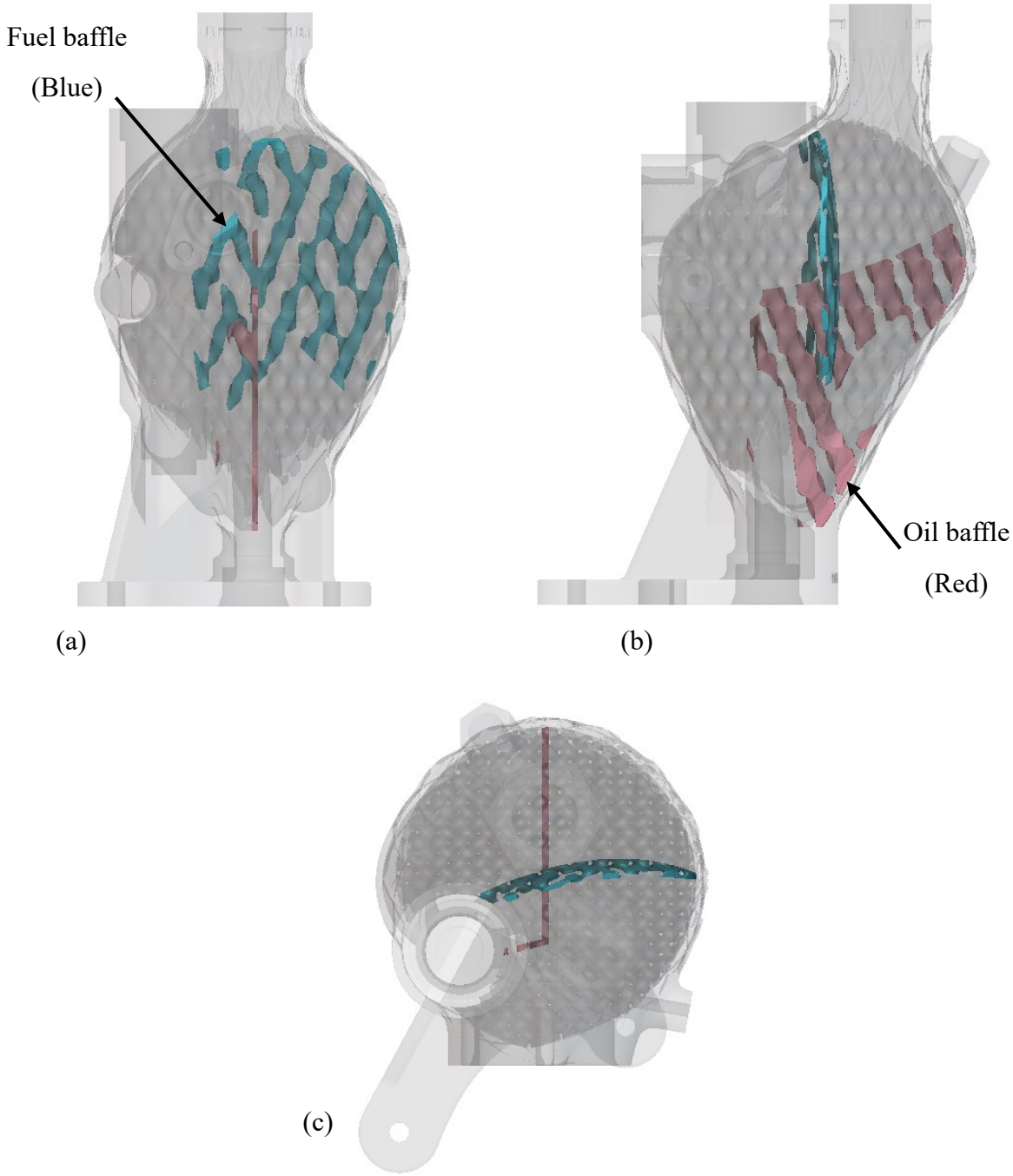

Figure 34: Orthographic views of the baffles inside the heat exchanger core. (a) Front view, (b) Left view, (c) Top view.

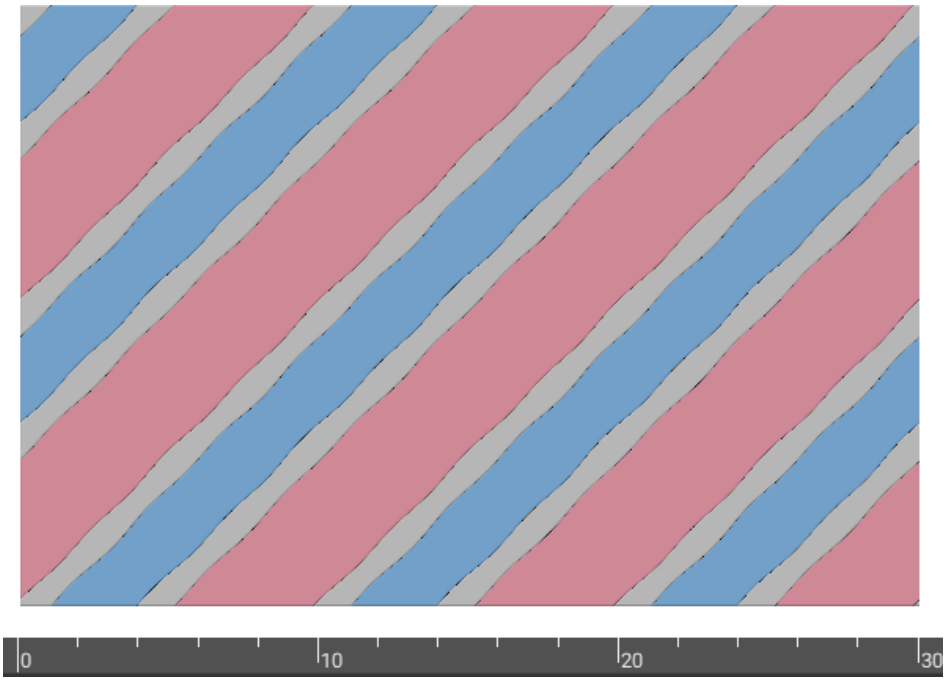

Figure 35: Example of a lattice wall offset.
The lattice wall is offset towards the blue region by 0.5 mm

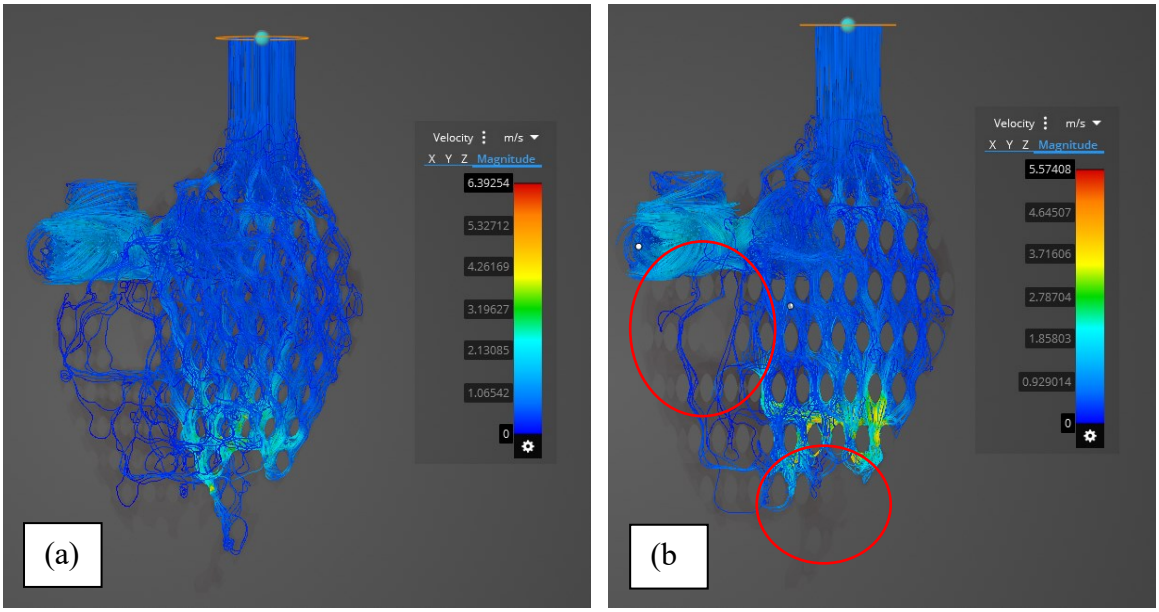

Figure 36:Fuel flow streamline comparison;
(a) velocity streamlines of the 10x10x20 mm unit cell size lattice, (b) velocity streamlines of the 10x10x30 mm unit cell size lattice. The red circled area highlights low fluid flow regions present in the image (b) that is not present in image (a)

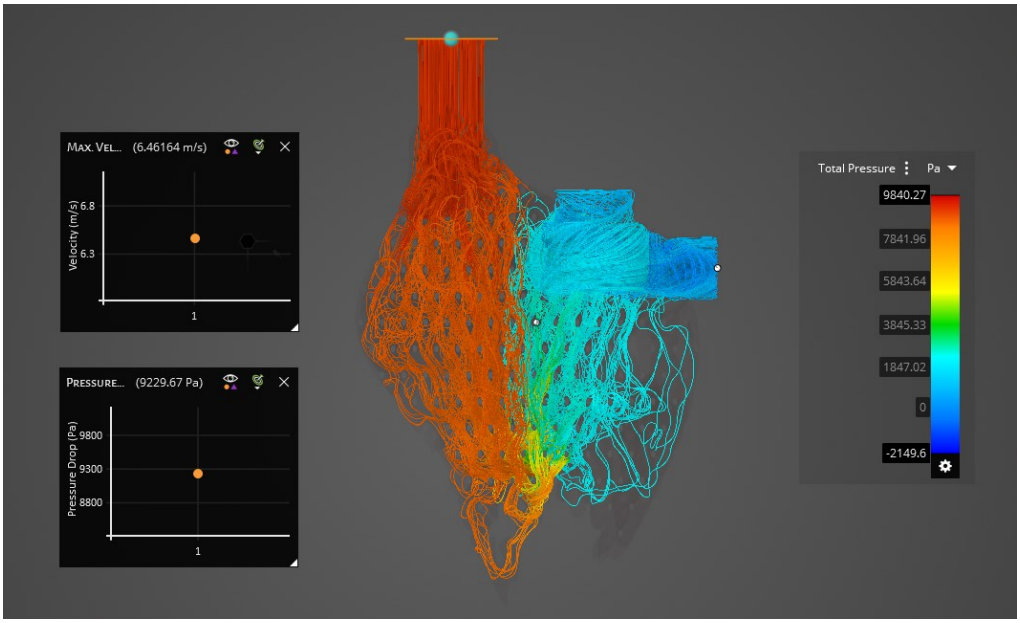

Figure 37: Fuel flow simulation results of the 12.5x12.5x30 mm cell size with a 0.5 mm mid surface offset

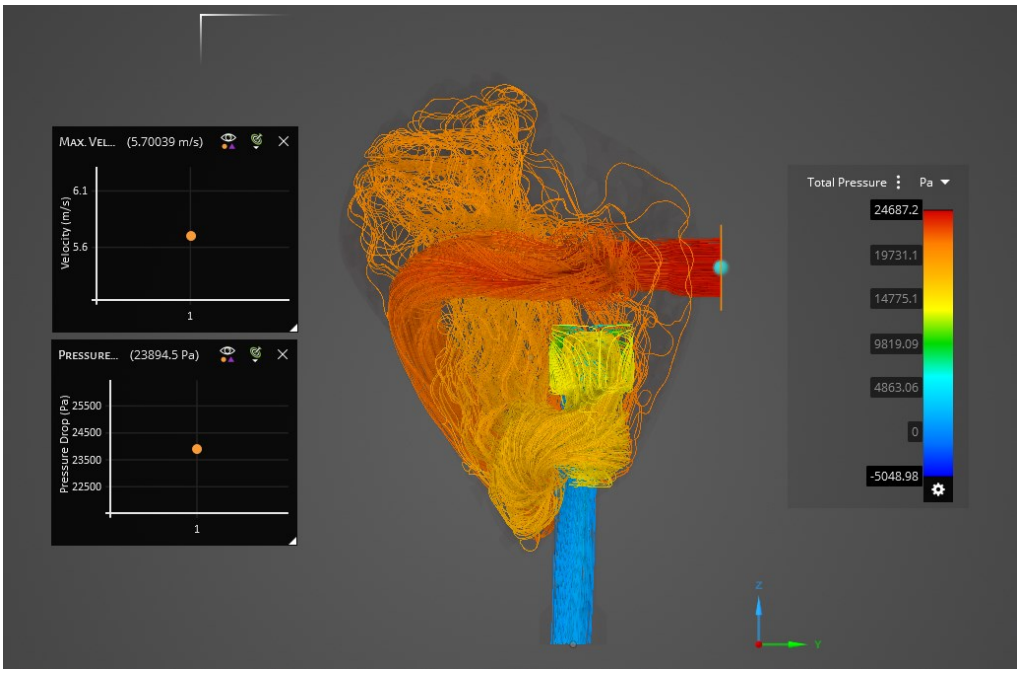

Figure 38: Oil flow simulation results of the 12.5x12.5x30 mm cell size with a 0.5 mm mid surface offset

2.3.3 Lattice Printability Assessment

To assess printability of the 12.5x12.5x30 mm unit cell size diamond TPMS lattice with a 0.5 mm mid surface offset, a leak test specimen was designed and printed (Figure 39a). The test specimen was designed where one of the volumes within the lattice can be enclosed by blocking the opening at the top of the specimen as shown in Figure 39(b). Therefore, by attaching an inflated ballon to the opening of the specimen as shown in Figure 40, a leak test could then be conducted by examining if an attached ballon deflated over time. Five test specimens were printed where the lattice wall thickness was specified to be 0.3, 0.4, 0.5, 0.6 and 0.75 mm. The test specimens were printed in a Renishaw 500 S Flex system, with AlSi10Mg powder using recommended print parameters from Renishaw. All test specimens passed the leak test as the ballons retained their starting pressure for more than 2 days. Additionally, a visual inspection was conducted on the downskin surfaces of the lattice and for any recoater damage, and no significant issues were observed. This successful printability assessment demonstrated that the lattice structures could be reliably printed with wall thicknesses as thin as 0.3 mm without leaks or significant surface defects.

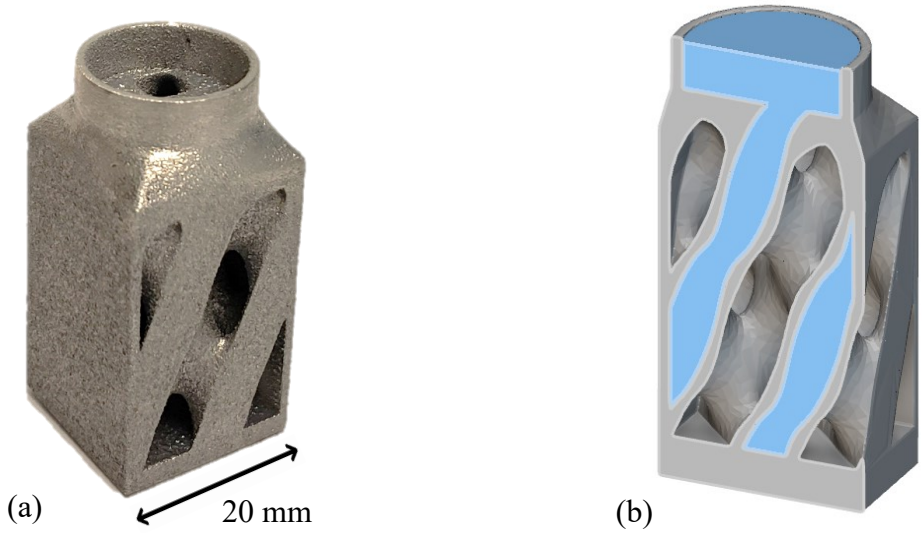

Figure 39: Images of the leak test specimen.
(a) Printed part and (b) Cross sectional view.

Figure 40: Leak test setup

2.4 Print Geometry Generation

In preparing the print model for manufacturing, several considerations were made to facilitate post processing steps. Firstly, extra material was added to all features that would need to be machined. Even though LPBF can produce high resolution components, the surface finish and resolution of AM would not be suitable for hydraulic fittings or standard threads. Therefore, an additional 0.5 mm of material was included on all surfaces that required machining. This allowance ensured that any surface irregularities or deviations from the nominal dimensions could be corrected during the machining process, resulting in precise final dimensions. Furthermore, an addition of 5 mm was added to the bottom surface that interfaced with the build plate, to ensure adequate material remained on the part for machining after removing the component off the build plate with a bandsaw. Figure 41 highlights the surfaces where extra material was added.

A ribbing texture was added to the heat exchanger core, as a cosmetic detail and to emphasize the design freedom in LPBF. To acknowledge contributions from companies and academic groups involved in this project, their respective logos were added to the print model to serves as a form of recognition for the collaborators.

The export file from nTop was a mesh file format(stl). To capture the intricate details of the component, it was initially meshed with a maximum allowable deviation of 0.5 mm. However, this resulted in a mesh that consisted of more than 13 million faces, and a file size >650 MB. Files of this size increase the computational demand when slicing and potentially fail to generate appropriate slice files depending on the capability of the computer. Therefore, the mesh was simplified using a 0.025 mm threshold. This reduced the number of faces in the mesh while keeping the distance between the input and output meshes below the specified threshold. The resulting mesh consisted of 892,156 faces and a file size of 44 MB. As shown in Figure 42, the simplified mesh maintained a similar geometrical profile to the initial mesh, while utilizing a fraction of its initial face count.

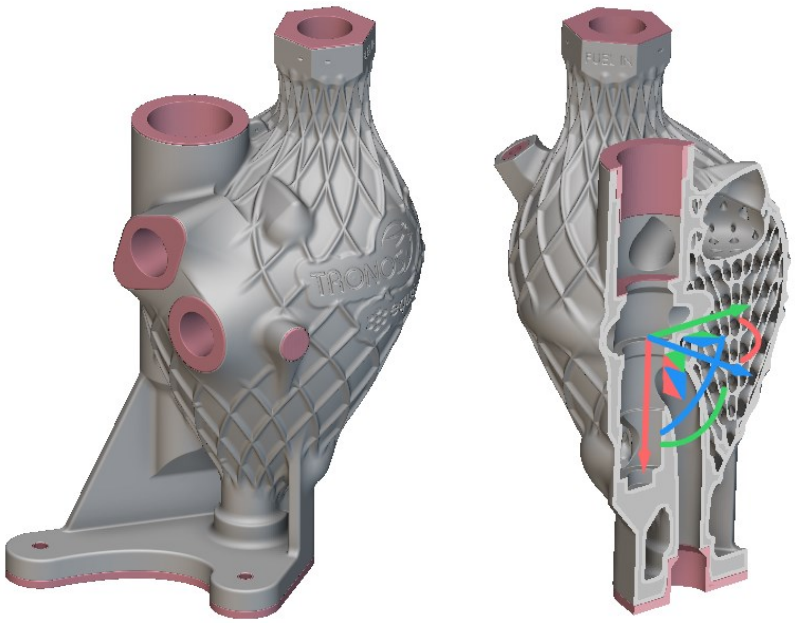

Figure 41: Extra material locations on the AM heat exchanger.
The surfaces in red indicate the specific locations where extra material was added to the print model.

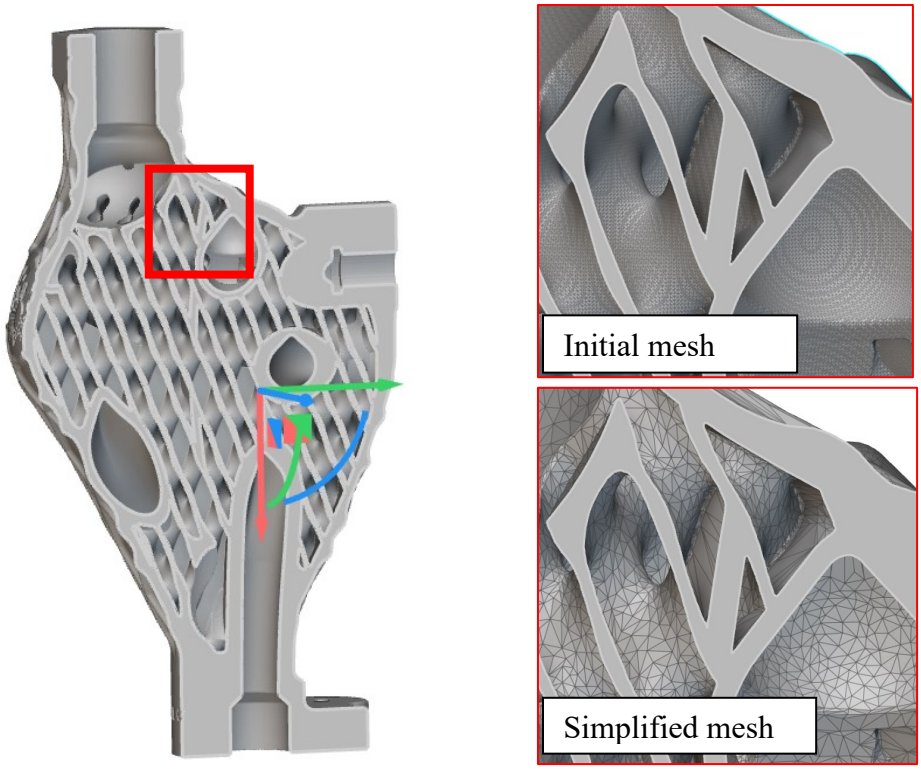

Figure 42: Comparison of the initial and simplified mesh concepts considered.

Chapter 3 Numerical Analysis

The numerical analysis aims to evaluate the thermal and fluid dynamics performance of the AM heat exchanger design. The traditional heat exchanger was also simulated to establish a reference for the target performance for the AM counterpart. Using CFD tools, various operating conditions and design parameters were simulated to visualize and analyze the thermal interactions within the heat exchanger. This analysis provided valuable insights for optimizing design parameters and ensuring the AM heat exchanger meets the required thermal performance specifications.

3.1 Conventional geometry

To simulate the thermal performance of the conventional heat exchanger, a computer-aided design (CAD) of the conventional design was created using SolidWorks. The original component consisted of stagnated finned features with small gaps between each strip, as shown in Figure 43(a). This configuration proved challenging to create a high-quality volume mesh for simulation due to the complexity of the full model and the increase in computation demand when meshing. Hence, a simplified heat exchanger core design was utilized as shown in Figure 43(b). To further simplify the geometry, the simulation was focused on the heat exchanger core, thus removing any solid material outside the core, as shown in Figure 43(c) compared to Figure 24.

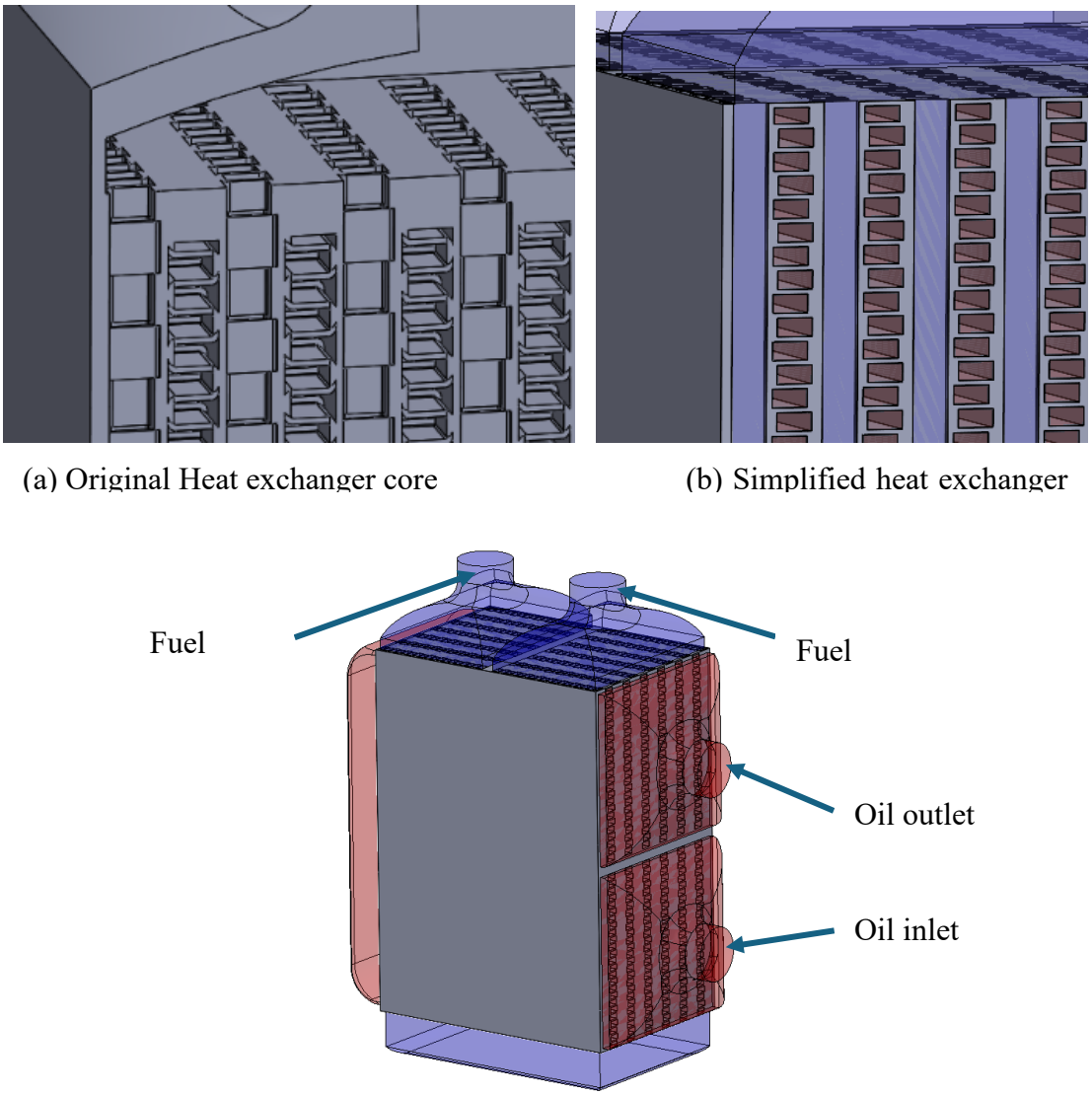

Figure 43: Conventional heat exchanger core visualization.

3.1.1 Conventional Geometry Meshing

The fault-tolerant meshing workflow in Ansys Fluent Meshing [40] was utilized to develop the volume mesh for simulation. A wrap extraction method with a poly volume fill was used to extract each domain for meshing. Curvature and proximity mesh controls were used and a minimum element size of 0.4 mm was selected to create a high-resolution mesh as shown in Figure 44. The resulting volume mesh quality is summarized in Table 7.

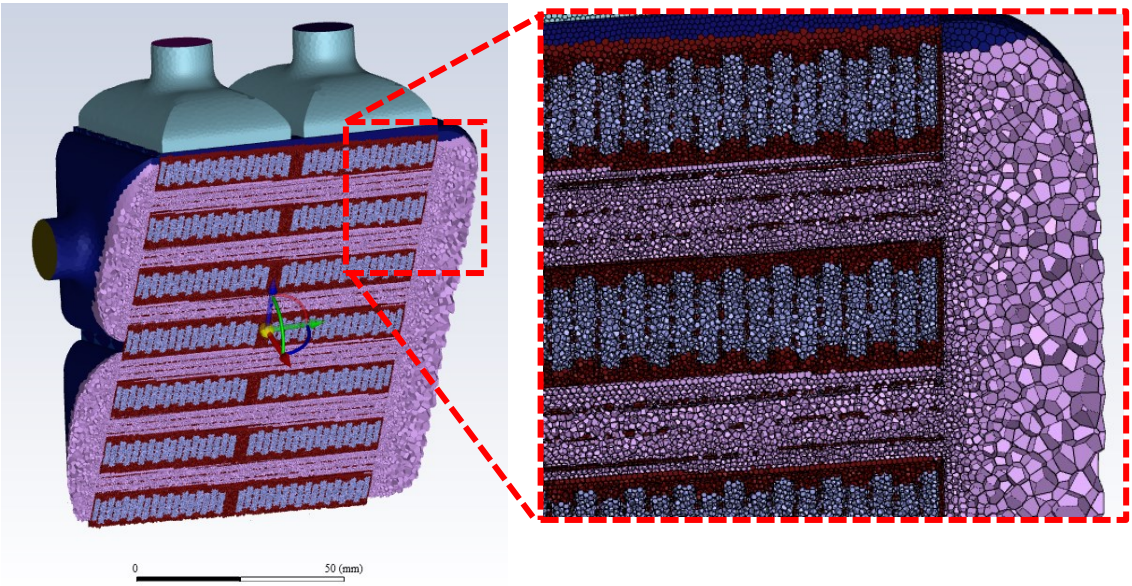

Figure 44: Sectional view of the conventional heat exchanger volume mesh

Table 7: Summary of the conventional heat exchanger mesh quality

Number of cells	9 579 733		
Orthogonal quality	Avg: 0.89	Min: 0.02	Max: 0.99
Orthogonal cell count	Quality<0.100: 207 cells	Quality<0.04: 3 cells	
Skewness	Avg: 0.11	Min: 0.002	Max: 0.98
Aspect ratio	Avg: 2.69	Min: 1.34	Max: 206.87

3.2 AM Geometry

To simulate the performance of the AM heat exchanger, the fluid volumes within the heat exchanger were modeled. As shown in Figure 45, separate meshes for the solid, oil, and fuel domains were created. Two different configurations of the heat exchanger were created where the lattice wall thickness varied between 0.75 mm and 1.0 mm.

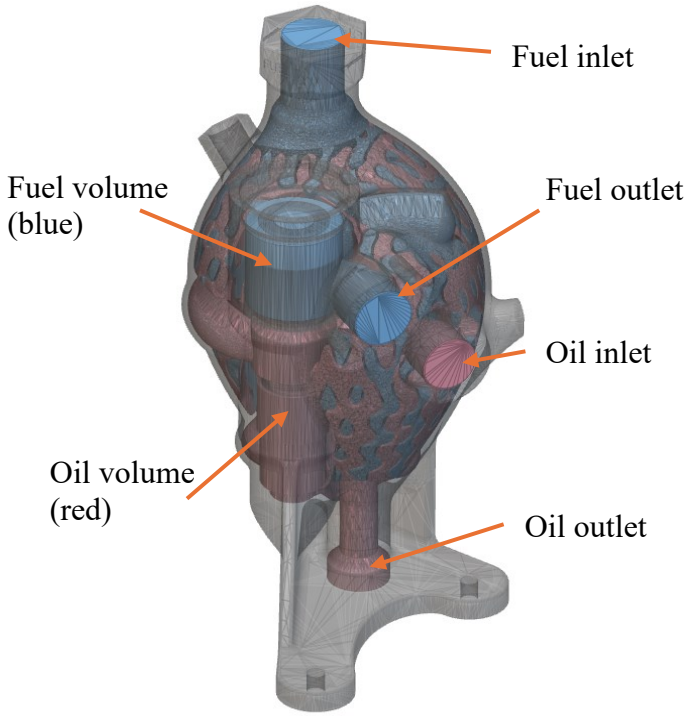

Figure 45: schematic representation for the AM heat exchanger geometry and its features.

3.2.1 AM Geometry Meshing

The AM geometry was meshed using the fault-tolerant meshing workflow in Ansys Fluent meshing. To evaluate the effect of wall thickness on the fuel outlet temperature, 1.00 and 0.75 mm lattice wall thickness AM heat exchangers were simulated.

Multiple configurations of mesh controls were tested to obtain a viable mesh. However, the setup that resulted in a workable mesh for the 0.75 mm thickness wall lattice heat exchanger was a mesh using polyhedral volume infill with a minimum element size of 0.75 mm for curvature and proximity controls (Figure 46). The 1.00 mm lattice wall thickness heat exchanger was meshed using a polyhedral hex-core volume infill, with a minimum element size of 1.19 mm for the curvature and proximity controls (Figure 47). The resulting volume mesh quality is summarized in Table 8 and Table 9.

Ideally, a smaller element size would be preferred to enhance the resolution of the mesh and better capture near wall behaviour of the fluid. However, attempts at smaller element

sizes resulted in a mesh failure due to the increased computational demand and the inherent complexity of the AM design.

Table 8: Summary of the mesh quality of 1.0 mm heat exchanger

Number of cells	1 035 686		
Orthogonal quality	Avg: 0.79	Min: 0.01	Max: 1
Orthogonal cell count	Quality<0.100: 699 cells	Quality<0.04: 39 cells	
Skewness	Avg: 0.21	Min: 0	Max: 0.99
Aspect ratio	Avg: 4.60	Min: 1	Max: 815.26

Table 9: Summary of the mesh quality of 0.75 mm heat exchanger

Number of cells	2 391 811		
Orthogonal quality	Avg: 0.88	Min: 0.002	Max: 0.99
Orthogonal cell count	Quality<0.100: 609 cells	Quality<0.04: 22 cells	
Skewness	Avg: 0.12	Min: 0.001	Max: 0.99
Aspect ratio	Avg: 3.23	Min: 1.36	Max: 3696.34

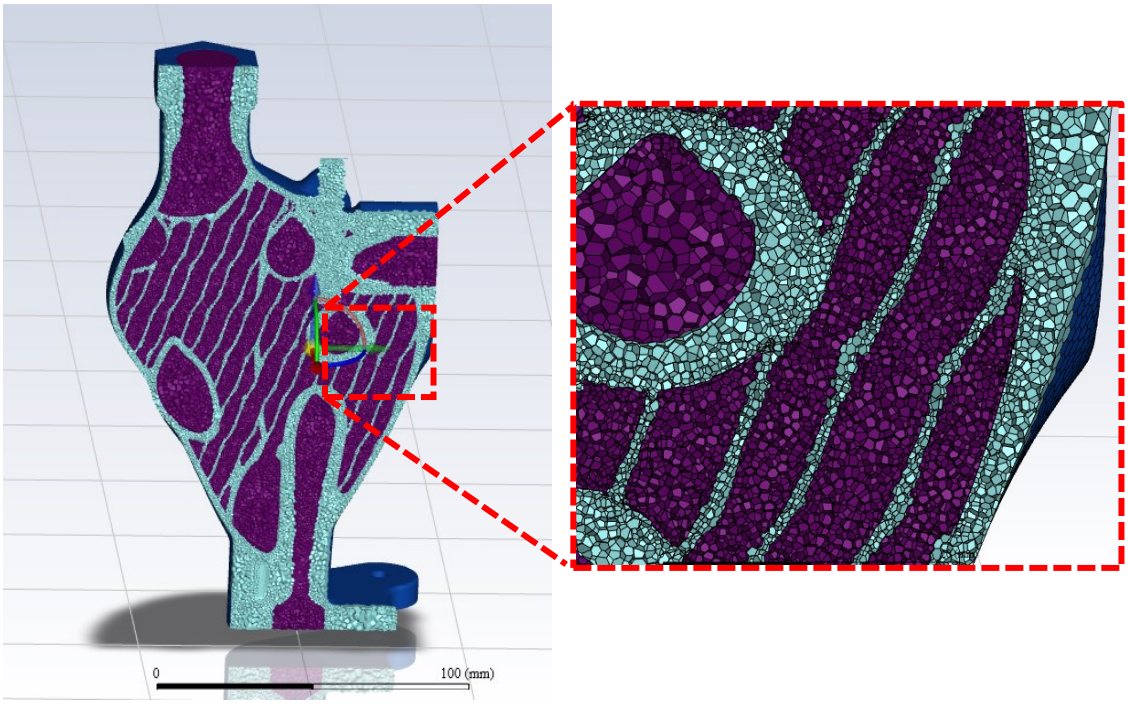

Figure 46: Volume mesh preview of the 0.75 mm lattice wall thickness using polyhedral volume infill

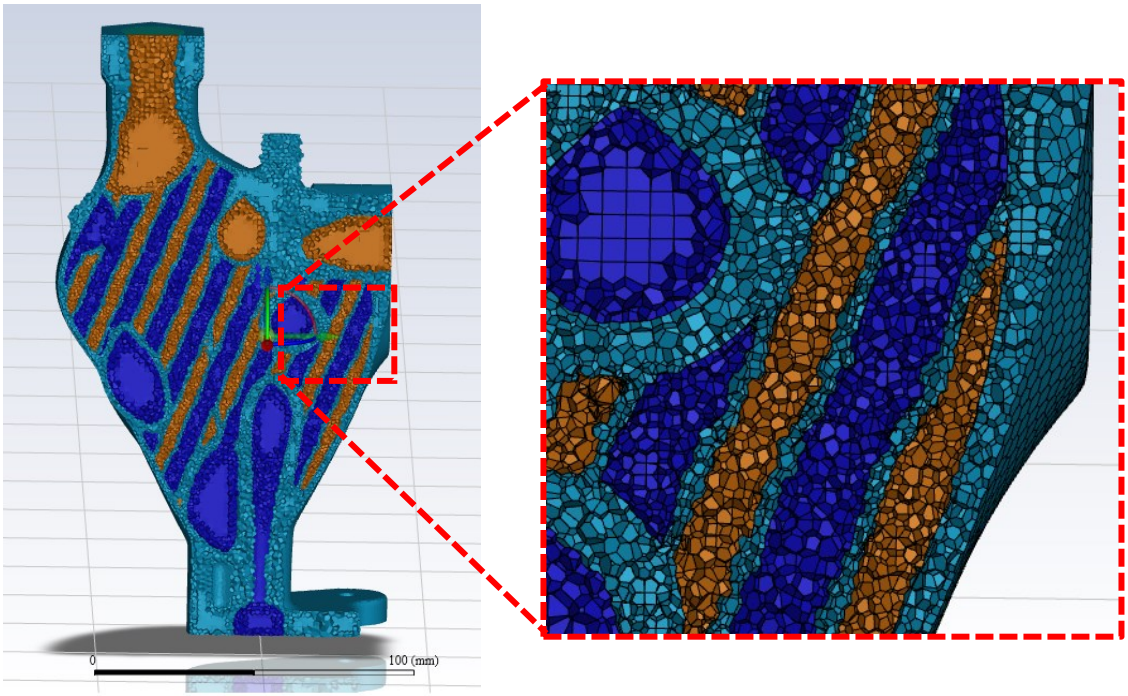

Figure 47: Volume mesh preview of the 1.00 mm lattice wall thickness using poly-hexcore volume infill

3.3 Governing Equations

The conjugate heat transfer simulation was performed by solving the mass, momentum and energy equations. The Reynolds numbers of the fluids ranged from approximately 500 - 3888 which are within the turbulent regime as shown in section 3.5.3, hence utilizing turbulent physics. The k-omega SST viscous model with low-Reynolds correction was employed to better handle the transition from laminar to turbulent flow.

The governing equations were averaged using the Reynolds-Averaged Navier–Stokes (RANS) approach. The mean flow, mean temperature, and temperature variance fields are defined using the following equations (19), (20), and (21):

$$\frac{\partial \bar{u}_i}{\partial x_i} = 0 \tag{19}$$

$$\frac{\partial \bar{u}_i}{\partial t} + \frac{\partial (\bar{u}_i \bar{u}_j)}{\partial x_j} = -\frac{1}{\rho}\frac{\partial \bar{p}}{\partial x_i} + v\frac{\partial^2 \bar{u}_i}{\partial {x_i}^2} + \frac{1}{\rho}\left[\frac{\partial\left(-\overline{u_i' u_j'}\right)}{\partial x_i}\right] + \bar{S}_i \tag{20}$$

$$\frac{\partial \bar{T}}{\partial t} + \frac{\partial (\bar{u}_j \bar{T})}{\partial x_j} = \left(\frac{v}{Pr}\right)\frac{\partial^2 (\bar{T})}{\partial x_j^2} + \frac{1}{\rho}\left[\frac{\partial\left(-\overline{T' u_j'}\right)}{\partial x_j}\right] + \bar{S}_T \tag{21}$$

In the above system of equations, $\bar{u}_i$ represents the ensemble averaged (mean) velocity, $\bar{p}$ is the mean pressure, and $\bar{T}$ stands for the mean temperature. $\bar{S}_i$ and $\bar{S}_T$ represent the source terms related to momentum and thermal energy equations, respectively and ρ, v, and P_r denote the fluid properties of density, kinematic viscosity and Prandtl number, respectively. u' and T' represent the fluctuating velocity and temperature, respectively. The so-called Reynolds stress tensor and turbulent heat flux vectors are denoted by $\rho\overline{u_i' u_j'}$ and $\rho\overline{T' u_j'}$ respectively.

The Reynolds stress appeared in the governing equations as the result of ensemble averaging of the governing equation needs to be modeled to close the system of governing equations. As such, the inherent randomness of the fluid flow translates to the Reynolds stress in the RANS equation. The Boussinesq hypothesis introduces the concepts of the

eddy viscosity to approximate the Reynolds stress term. The Boussinesq hypothesis describes the connection between Reynolds stress, velocity gradient and turbulent viscosity using the following equations (22), (23).

$$-\overline{u_i' u_j'} = v_t \left(\frac{\partial u_i}{\partial x_j} + \frac{\partial u_j}{\partial x_i} \right) - \frac{2}{3}(k)\delta_{ij} \tag{22}$$

$$-\overline{T' u_j'} = \alpha_t \left(\frac{\partial \bar{T}}{\partial x_j} \right) \tag{23}$$

The $\boldsymbol{k-\omega}$ SST model is used to model the Reynolds stress tensor and close the system of governing eruptions. The k-Omega SST model with Low Re-corrections was used to define the viscosity of the fluid. The k-Omega SST model is widely known for its versatility and adaptability across a wide range of flow regimes. It is a two-equation eddy-viscosity model, which is a hybrid model of Wilcox $\boldsymbol{k-\omega}$ and the $\boldsymbol{k-\varepsilon}$ models. It utilizes the $\boldsymbol{k-\omega}$ model near the wall and the $\boldsymbol{k-\varepsilon}$ model in the free stream. The $\boldsymbol{k-\omega}$ SST model is defined through the following equations (24), (25).

$$\frac{\partial k}{\partial t} + \bar{u}_j \frac{\partial k}{\partial x_j} = P_k - \beta^* k\omega + \frac{\partial}{\partial x_j}\left[(\nu + \sigma_k \nu_t) \frac{\partial k}{\partial x_j} \right] \tag{24}$$

$$\frac{\partial \omega}{\partial t} + \bar{u}_j \frac{\partial \omega}{\partial x_j} = \alpha S^2 - \beta \omega^2 + \frac{\partial}{\partial x_j}\left[(\nu + \theta_\omega \nu_t) \frac{\partial \omega}{\partial x_j} \right] + 2(1 - F_1)\sigma_{\omega 2} \frac{1}{\omega} \frac{\partial k}{\partial x_i} \frac{\partial \omega}{\partial x_i} \tag{25}$$

Where $\boldsymbol{k}$ and $\boldsymbol{\omega}$ is the turbulent kinetic energy and specific dissipation rate respectively, and P, S, F, α and β are closure coefficients.

After solving the transport equations for k and omega, the values of eddy viscosity and eddy diffusivity are found through appropriate correlations introduced for k-Omega SST

model leading to closure of governing equations for mass, momentum, and heat transfer (Equations (19), (20), and (21)).

3.4 Simulation Setup and Boundary Conditions

The Conjugate heat transfer simulation was conducted using the commercial package Ansys Fluent 2023 R2. The software was run on an Intel Core i7-10700F CPU, with a Nvidia GeForce RTX 3060 and 64 GB of DDR4 RAM. Simulation was run with 14 processors and double precision accuracy for numerical handing.

Inlet parameters such as mass flow rate and temperature were specified according to industry partner's specifications. The fuel and oil outlet pressure were set to 0 Pa. The outlet temperature was calculated using the surface integral function of the area-weighted average of its respective outlet surfaces.

3.4.1 Simulation Material Properties

The hot fluid in the heat exchanger is the lubrication oil in the aircraft engine, and the cold fluid is the fuel. One of the more common types of fuel used in aerospace is Jet A1. Ansys fluent database material properties were used for Jet A1 fuel. For the lubrication oil, a combination of MIL-L-23699 military specification and engine oil properties found in the Ansys Fluent database was used.

Equispheres provided the AlSi10Mg powder used to manufacture the AM Heat exchanger. The density and thermal conductivity of the material in a printed state were measured, and the heat capacity was obtained by Xometry [41] for their AlSi10Mg material properties.

The AM aluminum alloy properties used for the simulation were a combination of analysis conducted internally and material properties published by Xometry for their AlSi10Mg material properties. Additionally, Ni625 and copper material properties from the Ansys fluent database were used to simulate different material configurations of the AM heat exchanger.

For the conventionally manufactured heat exchanger simulation, aluminum material properties found in the Ansys Fluent database were used. Table 10 summarizes the material properties used in the simulations.

Table 10: Summary of the material properties utilized in numerical simulations.

Material	**Density (kg/m^3)**	**Thermal conductivity (W/m K)**	**Heat Capacity (J/kg K)**	**Viscosity (kg/m s)**
Aluminum (Traditional heat exchanger)	2719	202.4	871	-
AlSi10Mg	2610	116.62	915	-
Ni625	8442	9.75	411	-
Copper	8978	387.6	381	-
Jet A1 fuel	768	0.12	2067	0.0009
Oil	1000	0.15	1845	0.005

3.5 Results Analysis

The aim of the current simulation study was to evaluate the performance of the AM heat exchanger and compare it with the conventionally manufactured counterpart. A parametric study was also conducted on the AM heat exchanger to analyse the effect of different combinations of materials and wall thicknesses. The performance requirement defined by the industry partner, was to obtain a fuel outlet temperature greater than 32 °C, as this ensured that the thermally regulating valve integrated into the heat exchanger would regulate the temperature within its working regime.

3.5.1 Quantitative Results

To obtain a reference for evaluating the performance of the AM heat exchanger design, the conventional unit was simulated first. The simulation resulted in a fuel outlet temperature of 37.3 °C. The temperature contour of the traditional heat exchanger is shown in Figure 48.

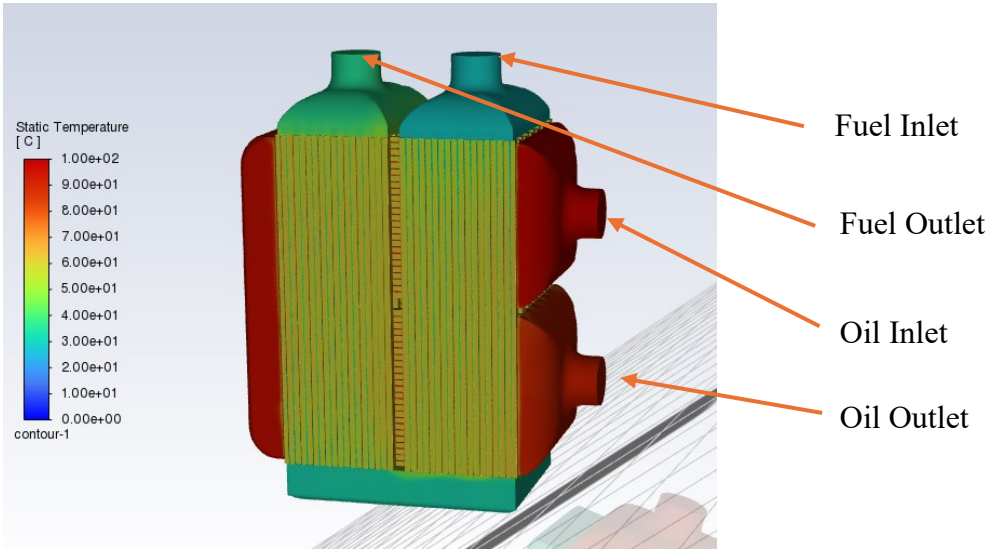

Figure 48: Simulation of the simplified traditional heat exchanger.

The AM Heat exchanger was simulated with varying lattice wall thickness and materials to evaluate the sensitivity of the design that influences the fuel outlet temperature. The fuel outlet temperature was monitored to ensure the solution convergence is obtained. The summary of the simulation results is shown in Table 11. All configurations resulted in a fuel outlet temperature greater than 32 °C, meeting its thermal performance requirement. Figure 49 shows the temperature contour of the 0.75 mm lattice wall thickness AlSi10Mg AM heat exchanger.

The oil flow rate was also varied on the 0.75 mm lattice wall thickness design to examine its effects on the fuel outlet temperature. The oil inlet flow rate was increased by increments of 5%, and the fuel outlet temperature was recorded. The results are shown in Figure 50. These results indicated a positive correlation between the oil flow rate and the fuel outlet temperature, as expected in a fuel-heated oil-cooled heat exchanger setup. An increased flow rate leads to a higher convection coefficient, which enhances the heat transfer rate

resulting in a higher outlet temperature. Notably, despite the incremental increases in oil flow rate, the change in fuel outlet temperature remained relatively small. Furthermore, increasing the oil flow rate, would result in higher pressure drop. Therefore, while increasing the oil flow rate can enhance heat transfer, it also introduces a trade-off with increased pressure drop. The 0.75mm lattice wall thickness AlSi10Mg configuration was selected to manufacture due to its similar heat transfer performance to the conventional designed and its lightweight material property compared to the other evaluated materials.

Table 11: AM heat exchanger simulation fuel outlet temperatures.

Wall thickness (mm)	**Material**	**Fuel outlet temperature (°C)**
1.00	Copper	36.5
1.00	AlSi10Mg	36.1
1.00	Ni625	35.2
0.75	Copper	37.6
0.75	AlSi10Mg	37.2
0.75	Ni625	36.3

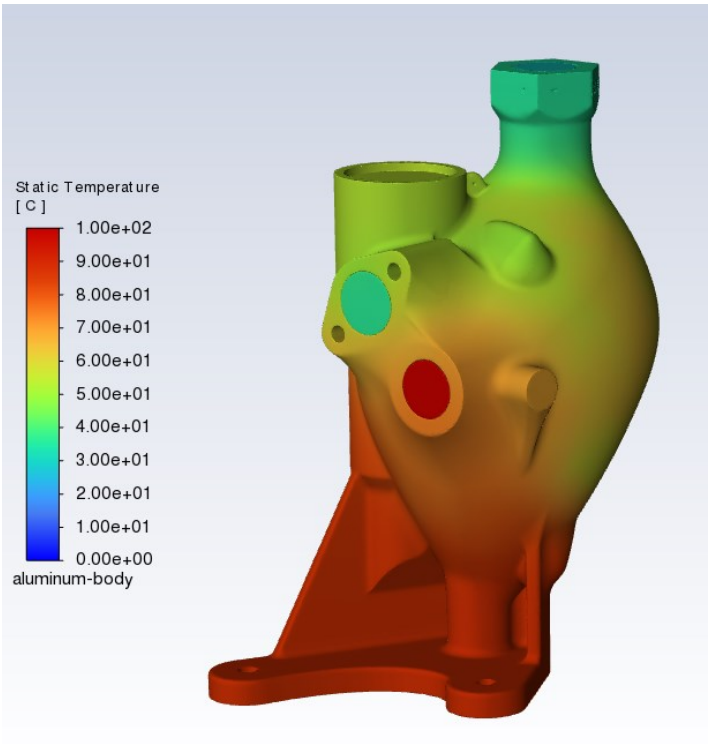

Figure 49: Temperature contour of the 0.75 mm lattice wall thickness AM heat exchanger.

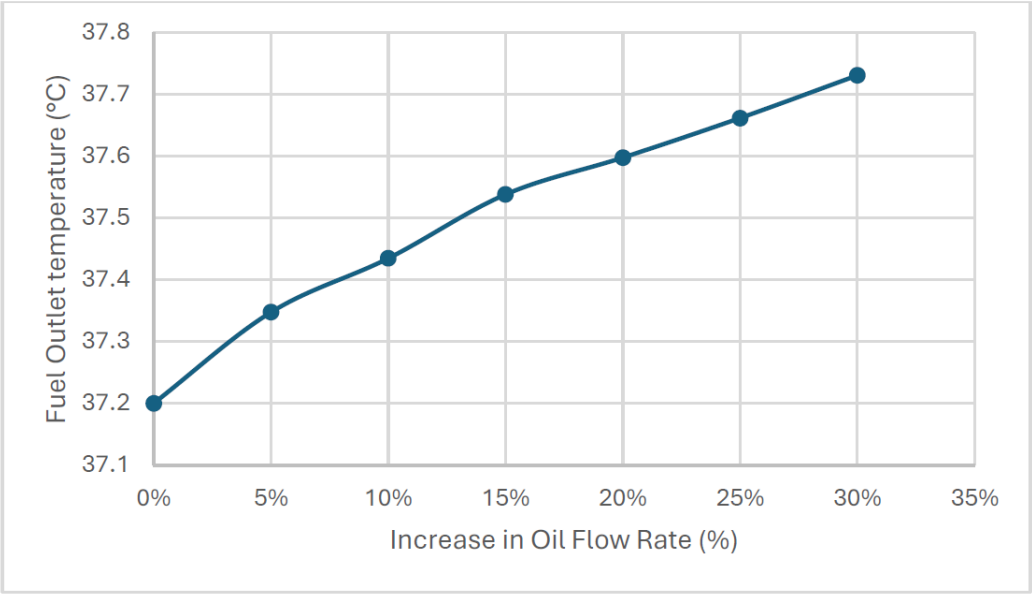

Figure 50: The plot illustrates the correlation between the oil flow rate and the simulated fuel outlet temperature.

3.5.2 Qualitative Results

To gain physical insights on the three-dimensional flow inside the heat exchanger, multiple cross-sectional views were analyzed. These cross-sectional views were taken along the XY, XZ, and YZ planes, as shown in Figure 51, and provided distinct perspectives of the flow within the heat exchanger. The blue area in the cross-section images represents the fuel region, while red indicates the oil region passing through the heat exchanger. The arrow in Figure 52(a) indicates the fuel flow passage, and the arrow in Figure 52(b) indicates the oil flow passage through the lattice core.

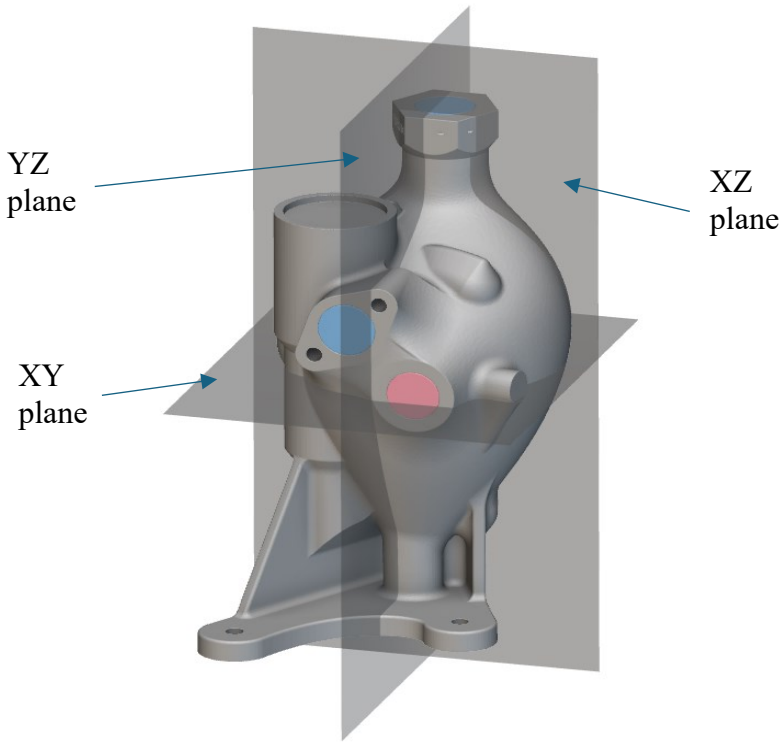

Figure 51: Cross section plane locations.

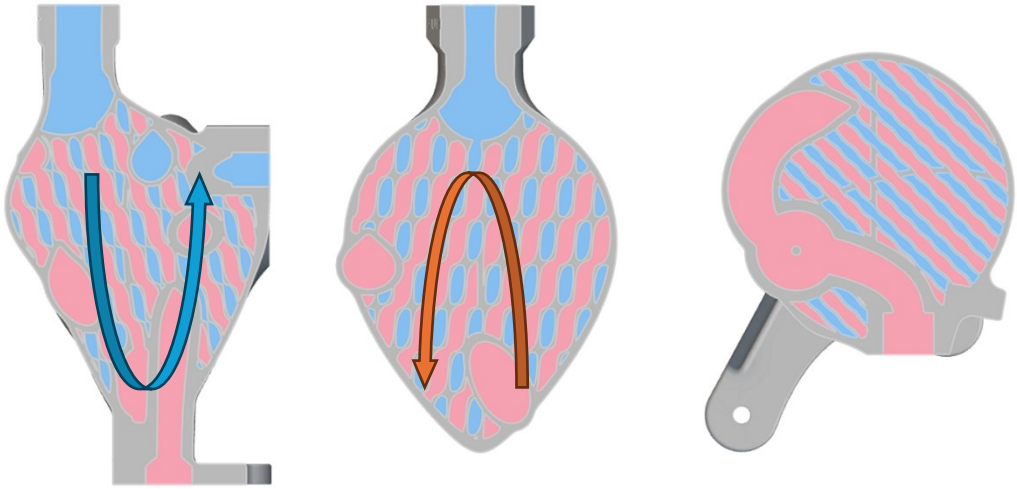

(a) YZ sectional view (b) XZ sectional view (c) XY sectional view

Figure 52: Cross sectional views of the AM heat exchanger.

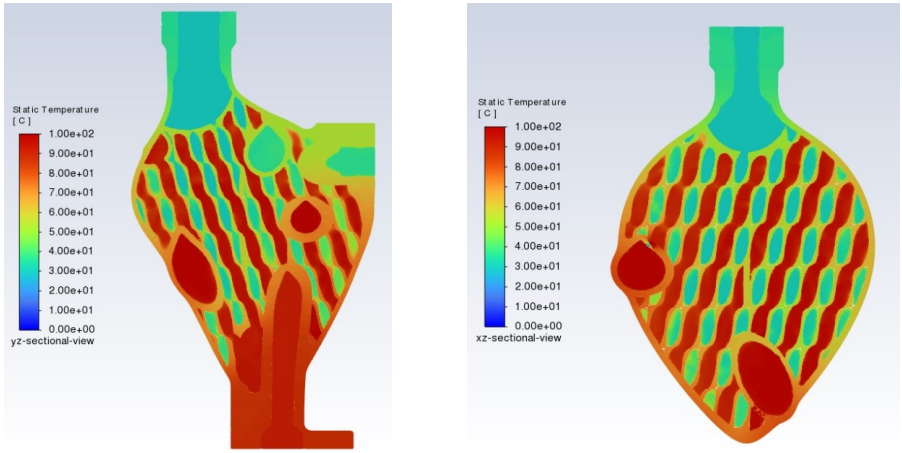

(a) YZ cross-section (b) XZ cross-section

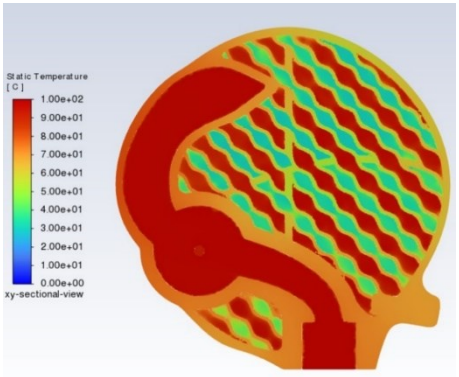

(c) XY cross-section

Figure 53: Cross section views of the temperature contour.

A closer examination of the YZ cross-sectional view (Figure 53a) reveals an effective thermal energy exchange with a moderate gradient, suggesting efficient heat conduction. The higher velocity regions correspond to a uniform temperature distribution, displaying enhanced heat transfer through forced convection.

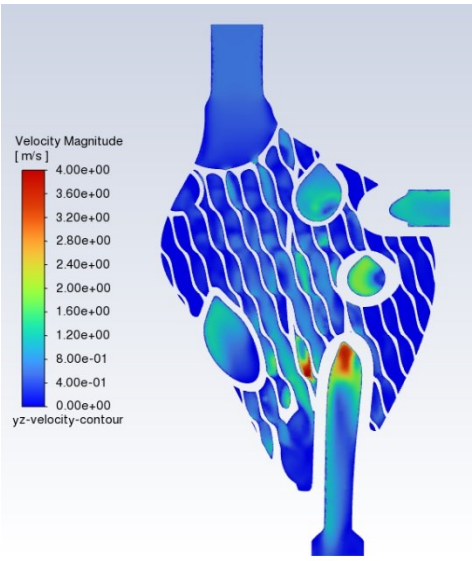

(a) YZ cross-section view

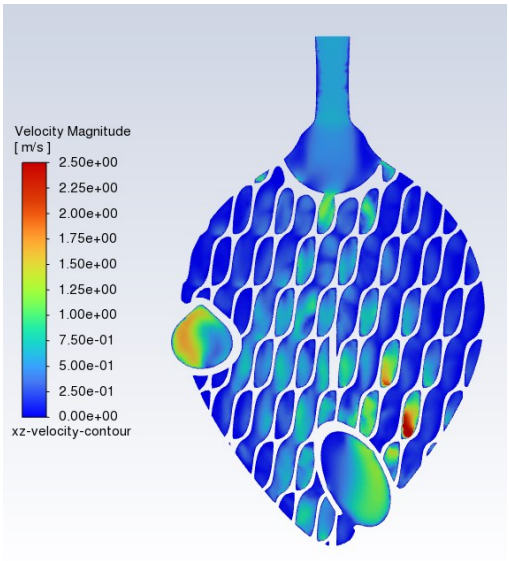

(b) XZ cross-section view

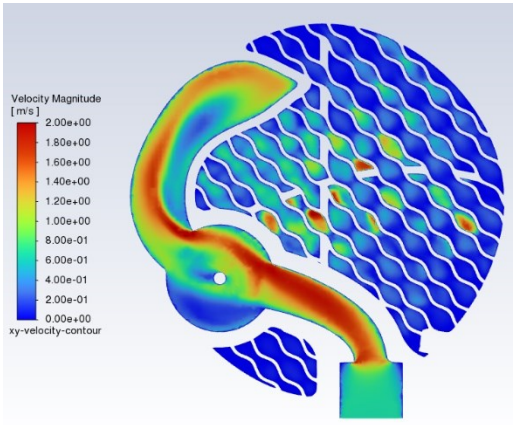

(c) XY cross-section view

Figure 54:Cross section views of the velocity magnitude contour.

The velocity (Figure 54) and vorticity (Figure 55) contours reveal insightful details about the fluid flow patterns, mixing, and effect of turbulence within the heat exchanger. Predominantly, there is a significant concentration of fluid flow in the central regions of the heat exchanger, as depicted by the high velocity and vorticity magnitudes, indicative of accelerated fluid movement. The vorticity contours support a dynamic environment where the interplay of rotational flow forces enhances thermal mixing, thus enhancing the heat transfer process. Conversely, the peripheral areas which are closer to solid surfaces exhibit a decrease in both flow velocity and vorticity, which suggests subdued turbulence and, consequently, less efficient thermal convection. Although the fuel temperature around the outer parameter is relatively higher than the fuel fluid in the center of the lattice core, the heated fuel is not optimized for convection heat transfer due to the low vorticity and velocity.

The poor circulation and uneven flow distribution could be improved through strategic design modifications that promote more uniform flow characteristics across the entire cross-sectional area of the heat exchanger.

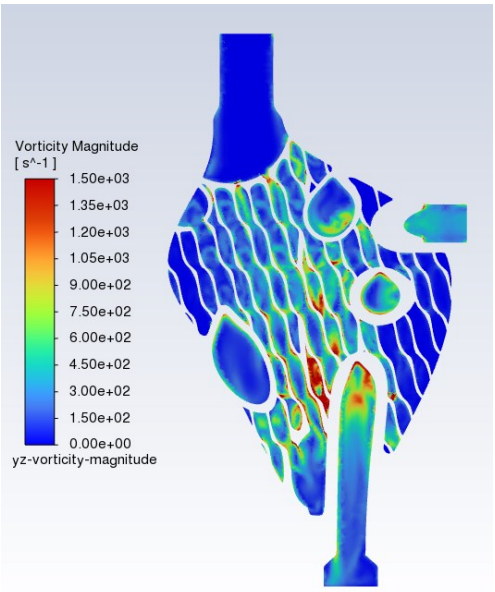

(a) YZ cross-section view

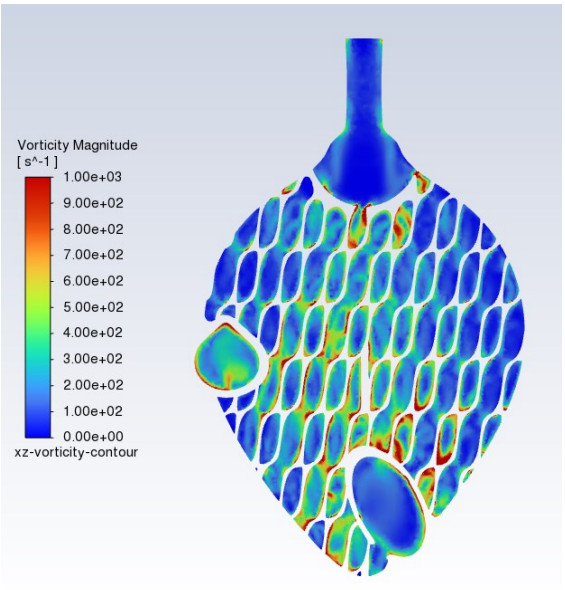

(b) XZ cross-section view

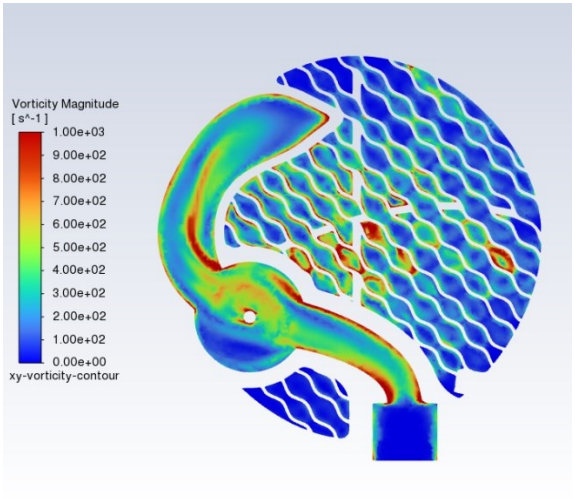

(c) XY cross-section view

Figure 55: Cross section views of the vorticity magnitude contour.

3.5.3 Thermal Resistance Analysis

Thermal resistance is defined as a measure of a material's resistance to heat flow. In the context of a heat exchanger, this attribute quantifies the resistance to heat flow on the fluid and solid materials while considering factors such as material properties, geometry, and operational conditions.

The total thermal resistance can be calculated through equations (26), (27), and (28):

$$R"_{Total} = R"_{oil} + R"_{fuel} + R"_{solid} \tag{26}$$

$$R"_{fluid} = \frac{1}{h_{fluid}} \tag{27}$$

$$R"_{solid} = \frac{L}{k} \tag{28}$$

Where h is the convection heat transfer coefficient of the fluid material, L is the thickness of the lattice, and k is the thermal conductivity of the lattice material.

The geometry of the lattice varies depending on the z height of it. Therefore, the thermal resistance of the system varies due to the change in geometry and velocity of the fluid. Hence the thermal resistance of the oil and fuel was calculated at two separate transitional regions. Due to the unique geometry of the lattice, two transitional regions were selected for analysis as shown in Figure 56.

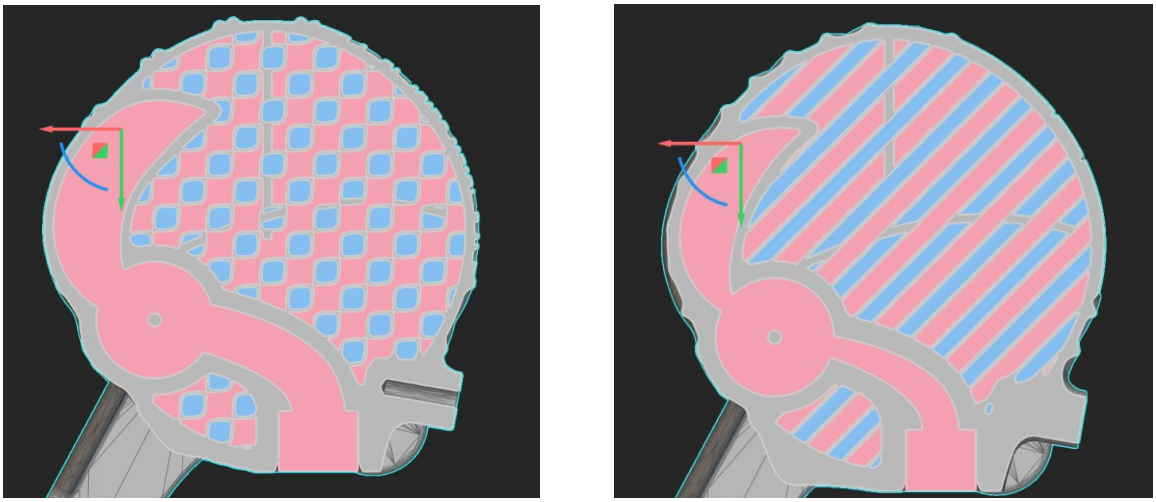

(a) Square cross-sectional area of the lattice

(b) rectangular sectional area of the lattice

Figure 56: Cross sectional view of the lattice.

To calculate the convection heat transfer coefficient of the fluids, the Reynolds number was calculated to identify if the fluid was laminar or turbulent. For laminar flow regions, the appropriate Nusselt number (Nu) was used assuming uniform heat flux to calculate the convection heat transfer coefficient. The Reynolds number (Re), hydraulic diameter (D_h) and the average velocity ($\bar{v}$) were calculated using equations (29), (30), and (31).

$$\mathrm{Re} = \frac{\rho \bar{v} D_h}{\mu} \tag{29}$$

$$D_h = \frac{4\,A_c}{P} \tag{30}$$

$$\bar{v} = 0.7\, v_{max} \tag{31}$$

Where ρ, $\bar{v}$, D_h, A_c and P is the density of the material, average velocity, hydraulic diameter of the geometry, cross-section area, and perimeter, respectively.

The maximum velocity of the oil within the square and rectangular sections was approximately 0.65 and 0.5 m/s respectively from simulation results. Thus, the Reynolds number of the oil fluid on the square and rectangular regions was calculated to be 543 and 534, respectively. Hence, the oil fluid was laminar in both sections of the lattice.

Assuming constant heat flux, a Nusselt number of 3.61 for the square section and 6.49 for the rectangular section was utilized to calculate thermal resistance of 1.15×10^{-2} and $6.42 \times 10^{-3}\ \frac{m^2 k}{W}$ respectively using equation (32).

$$h = \frac{k\ \mathrm{Nu}}{D_h} \tag{32}$$

For the fuel domain, the maximum velocity of the fuel within the square and rectangular sections was approximately 1.4 and 1.2 m/s, respectively from simulation results. Accordingly, the Reynolds numbers are 3759 and 3888 for the square and rectangular sections, respectively. In this case, the fuel flow was turbulent within the lattice. Hence,

the Nusselt equation for turbulent flow was utilized to calculate the convection heat transfer coefficient. The Nusselt equation for turbulent flow was as follows (equations (33) and (34)).

$$\mathrm{Pr} = \frac{C_p \mu}{k} \tag{33}$$

$$\mathrm{Nu} = 0.023\, R_e^{\frac{4}{5}}\, \mathrm{Pr}^{\frac{1}{3}} \tag{34}$$

Where Pr , C_p, μ, k are the Prandtl number, heat capacity, viscosity, and thermal conductivity of the material respectively. Utilizing the Nusselt number, the thermal resistance of the fuel was calculated to be 7.56×10^{-4} and $8.89 \times 10^{-4} \frac{m^2 k}{W}$ at the square and rectangular sections of the lattice. Subsequently, the thermal resistance of the lattice wall was calculated for each configuration considered as shown in Table 12.

When evaluating the thermal resistance of the heat exchanger, it was evident that the thermal resistance of the solid material used to fabricate the heat exchanger was significantly smaller than that of the fluid domains. Consequently, any enhancements to improve the heat transfer by altering the solid material properties would have a negligible impact on the total thermal resistance of the system. This was shown by the relatively minor changes in fuel outlet temperature when adjusting the wall thickness and material of the AM heat exchanger in simulation results.

Table 12: Thermal Resistance on the heat exchanger lattice

Material	**Thickness (mm)**	**Thermal resistance** $(\frac{m^2k}{W})$
Copper	0.75	1.93×10^{-6}
Copper	1.00	2.58×10^{-6}
AlSi10Mg	0.75	6.43×10^{-6}
AlSi10Mg	1.00	8.57×10^{-6}
Ni625	0.75	7.69×10^{-5}
Ni625	1.00	1.02×10^{-4}

3.6 Results Discussion

The simulation results and thermal resistance calculations provided valuable insight into the thermal performance and identified potential room for improvement within the AM heat exchanger design. The AM heat exchanger was simulated with copper, AlSi10Mg, and Ni625 as construction materials. Among these, copper exhibited the highest fuel outlet temperature due to its higher thermal conductivity. However, the fuel outlet temperature of heat exchangers made from AlSi10Mg and Ni625 were merely ~1.5 °C lower than the copper unit, for both 0.75 mm and 1.0 mm lattice wall thickness configurations. This small difference indicated that the thermal conductivity of the heat exchanger had a minimal impact of the fuel outlet temperature. Similarly, the comparison between the 1 mm and 0.75 mm lattice wall thickness simulations showed a temperature deviation of approximately 1 °C. The 0.75 mm wall thickness configuration resulted in a slightly higher fuel outlet temperatures as the conduction heat transfer within the solid material was higher due to the lowered thickness of the lattice wall. This further emphasized that minor variations to the lattice wall thickness also have a minimal impact on the fuel outlet

temperature. This was due to the relatively low thermal resistance of the lattice wall compared to the fluid domains.

Thermal resistance calculations indicated that the predominant thermal resistance was the fluid domains, primarily the oil domain, followed by the fuel domain. Notably, the total thermal resistance of the heat exchanger was equivalent to the thermal resistance within the oil domain. Hence, any improvements in the thermal resistance of the lattice wall would have a negligible impact on total thermal resistance. Therefore, to improve the heat exchanger performance, the thermal resistance of the oil domain must be reduced. This could be achieved by increasing the convection heat transfer coefficient of the oil, reducing the fluid domain's hydraulic diameter by modifying the lattice geometry, or increasing the average fluid flow velocity to achieve turbulent flow.

Furthermore, the simulation results from the varied oil flow rate also indicated a minimal increase in the fuel outlet temperature. When analyzing the cross-sectional views of the AM heat exchanger, it displayed a relatively high velocity and vorticity magnitude in the central region of the lattice core and poor circulation along the outer perimeter of the lattice core. Hence, modifying the geometry to obtain a uniform distribution of the high velocity and vorticity magnitude would result in a more efficient heat transfer between the fluids. Consequentially, increasing the fluid flow velocity and reducing the lattice cell size would increase the pressure drop between the inlet and outlet, hence revisiting the pressure drop requirements to ensure the updated design meets its requirements.

The AM AlSi10Mg heat exchanger with a 0.75 mm wall thickness had a similar fuel outlet temperature to the conventional heat exchanger and meets the minimum temperature requirement. Even though copper had a higher efficiency, AlSi10Mg is a significantly lower-density material, resulting in a lower-weight component, thus being more appropriate for aerospace applications.

Chapter 4 Manufacturing of AM Heat Exchanger

4.1 LPBF system

The AM heat exchanger was manufactured in a Renishaw RenAM 500S Flex LPBF machine at Tronosjet (Slemon Park, PEI, Canada). The RenAM 500S Flex was equipped of a single 500 W ytterbium fiber laser, and an open loop powder handling system. The powder silo was located at the top of the machine as shown in Figure 57, which facilitates the use of materials with lower flowability, such as aluminum alloys, by minimizing the risk of clogged valves or tubing. The system employed Argon (Alphagaz 1 Argon, UN 1006) as the inert gas to maintain an optimal build environment. The RenAM 500S Flex offered a build volume of 250x250x350 mm, providing ample space for producing complex and sizeable components like the heat exchanger in question.

Figure 57: RenAM 500 Flex machine

4.2 Build Setup

The first step of the manufacturing process in AM, is the creation of the laser scan slices. It is important to understand the critical features and post processing step(s) required to finalize the components, as the build layout can aid or constrain certain features from being fabricated. Since the AM heat exchanger was designed for LPBF, the design was optimized to be able to print with minimal supports, where only the fuel outlet and the oil inlet required pin supports shown in Figure 58(b). A sectioned AM heat exchanger was also added to the build as there was sufficient space and provides a better view into the heat exchanger core. Since the heat exchanger was >190 mm tall, tensile, density, and metallography test specimens were also included to utilize the vacant space on the build plate.

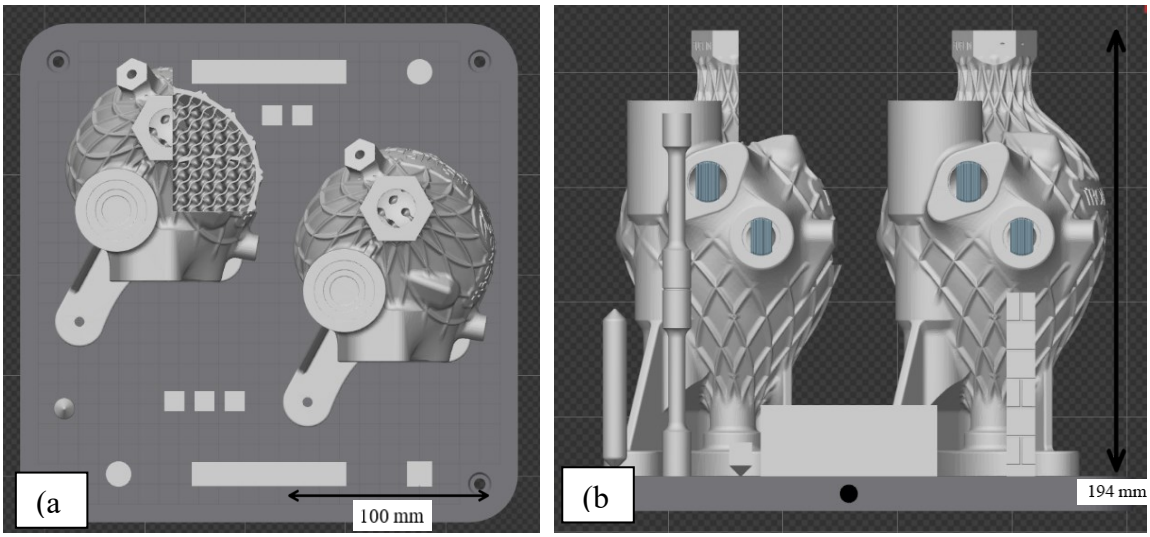

Figure 58: AM heat exchanger print layout.
(a) The top view of the build layout. (b) Front view of the build layout

Due to the complexity of the AM heat exchanger, it was decided that most of the machining features would be machined while the part was still attached to the build plate, as the part was easier to fixture inside the milling machine. Therefore, the parts were oriented and positioned as shown in Figure 58(a) to facilitate the machining operations. The vertical

tensile bars and the metallography bar were positioned at the outer perimeter of the build plate, as they would be cut off using a hacksaw without cutting the AM heat exchangers.

For machining the AM heat exchanger, the milling machine required a set of planes or datums from the build to locate the position and orientation of the part and then translate the position data to the tool to machine the required surfaces. The flat surfaces present on the AM heat exchanger were not sufficient to develop XZ or YZ planes, as the print surface was too rough. A longer surface area was required to generate a better average of the point to create an accurate surface that aligned with the CAD. The horizontal tensile bar blocks were orientated parallel to the flat surface of the fuel outlet face within the slice. Thus, enabling the option to utilize the longer flat surface of the tensile bar block to develop a plane that was parallel to the fuel outlet face (Figure 59).

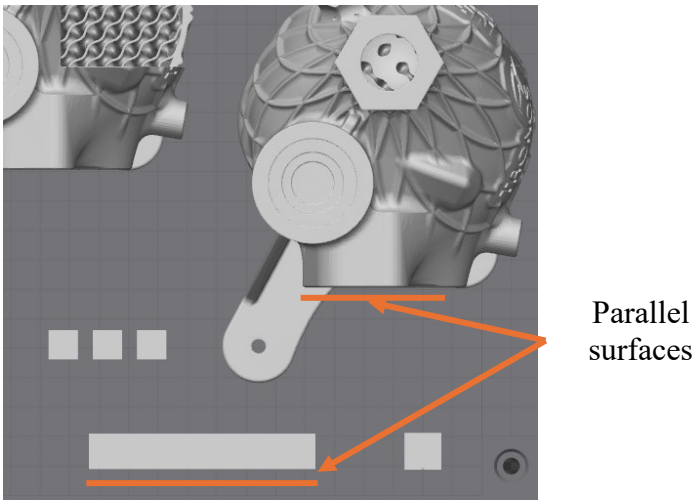

Figure 59: Displays the surface parallel to the fuel outlet face

Therefore, the selected build layout allowed for all the machining operations to be conducted while the part was still attached to the build plate. The resulting slice file consist of 6467 layers at 30um layer height, with an estimate build duration of 100hrs 41mins. The build completed successfully as shown in Figure 60.

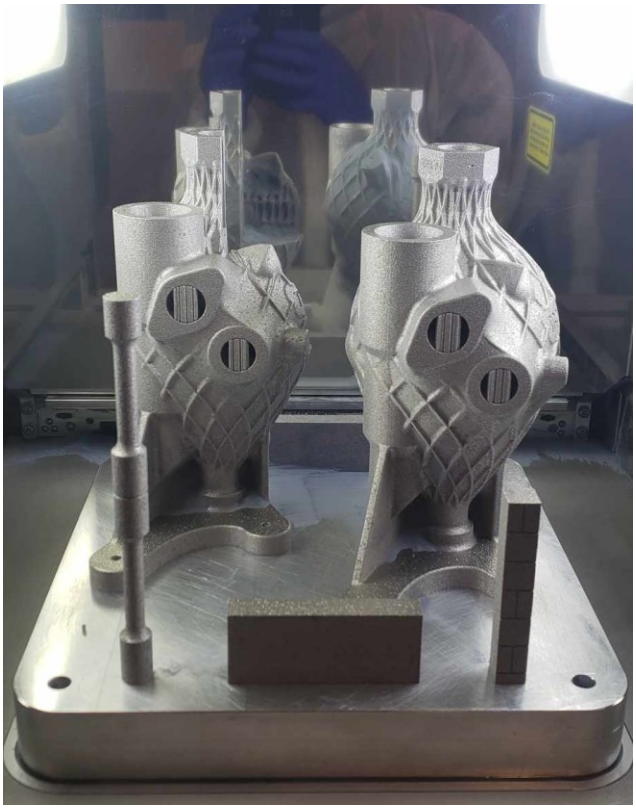

Figure 60: Post print image of the AM heat exchanger in the RenAM 500S Flex machine

4.3 Post Processing

Once the print was completed and removed from the LPBF machine, the build was further depowdered by manually agitating the build plate and using compressed air on a downdraft table. The build plate was orientated upside down while rigorously shaking and lightly tapping it using a mallet.

After depowdering, the build was stress-relieved to reduce residual stresses accumulated during the print process. This was completed in a Nabertherm LH 216/13 furnace for 2 hours at 300 °C followed by furnace cooling to room temperature. The stress relief reduces part deformation caused by residual stress when removed from the build plate.

Machining was then completed in a Deckel Maho DMU 80 monoblock 5-axis Computer Numerical Control (CNC) milling machine at Tronosjet. A CNC G-code was developed using Fusion360 for this purpose. The origin of the work coordinate system was positioned

at the intersection of the central axis and the top surface (including the extra material added for machining) of the thermal valve bore (Figure 62). The XY plane was set parallel to the bottom surface, and the XZ plane was orientated parallel to the fuel outlet face of the heat exchanger. Since the build plate was machined to a flatness of 0.002 inches, it was used to reference the XY plane. The horizontal test specimen was reference to identify the XZ plane, as it was positioned parallel to the fuel outlet face. The build plate was fixtured in the milling machine using four parallels to lift the build up and bolted on to the worktable as shown in Figure 61.

All machined surfaces were first given rough pass leaving 0.2 mm of stock material on the surface. This was followed by a finish pass where the remaining material was removed. This two step machining process reduced the likelihood of milling chatter or vibration marks on the finish surface, resulting in a smoother and dimensionally accurate surface. The fuel inlet, oil drain port and temperature valve threads were machined to specifications using a thread mill tool. The 10-32 threads on the fuel outlet surface and the mounting point were machined using a screw thread insert (STI) tap, and helicoils were installed for increased wear-resistance. The toolpaths of the first setup are shown in Figure 62. The engineering drawings of the AM Heat exchanger is shown in Appendix B.

The heat exchangers were then removed from the building using a horizontal bandsaw. To machine the bottom surface and the oil outlet port, the heat exchanger was fixtured horizontally as shown in Figure 63. Since the heat exchanger has two machined threads with precise known positions relative to its geometry, it was used to fixture and orientate the component within the CNC mill. Two threaded on one end studs were used to fix the component on a machined steel block, and a plastic 3D printed molded clamp was used to clamp the heat exchanger down to the steel block. The 3D printed mold was printed using Polylactic Acid (PLA) filament in an Ultimaker S5 fused filament fabrication (FFF) machine. The oil outlet, bottom surface and the two through holes, were machined with a rough and finish pass to ensure precise dimensionality and surface finish. The machining toolpaths are shown in Figure 64. Once all machining was completed, the heat exchanger was purged with compressed air to remove any machining chips. The post processed heat exchanger (Figure 65) weight 0.882 kg, whereas the conventional design weight 1.118 kg.

Therefore, the AM heat exchanger was approximately 20% lighter than the conventional counterpart.

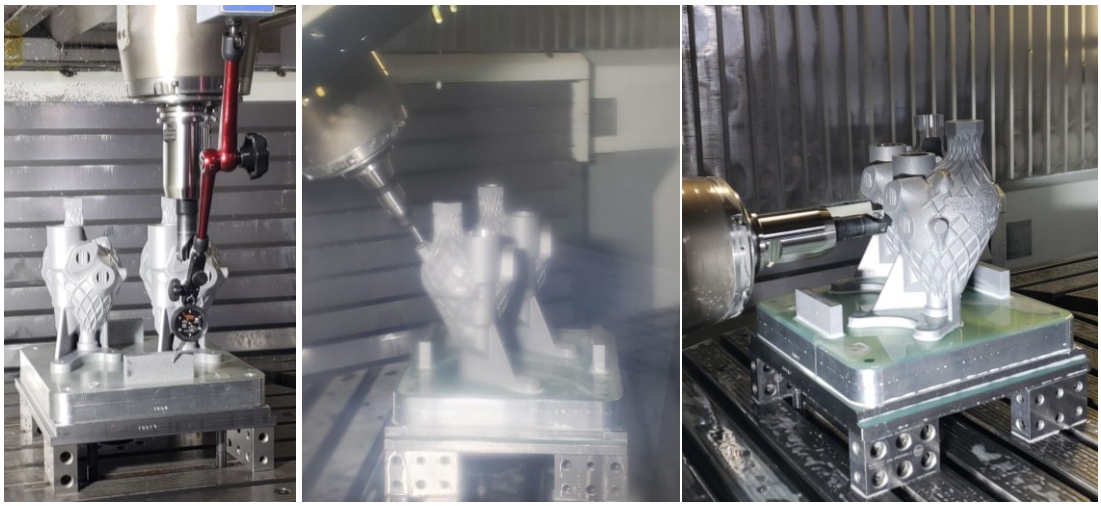

Figure 61: AM Heat exchanger machining setup 1

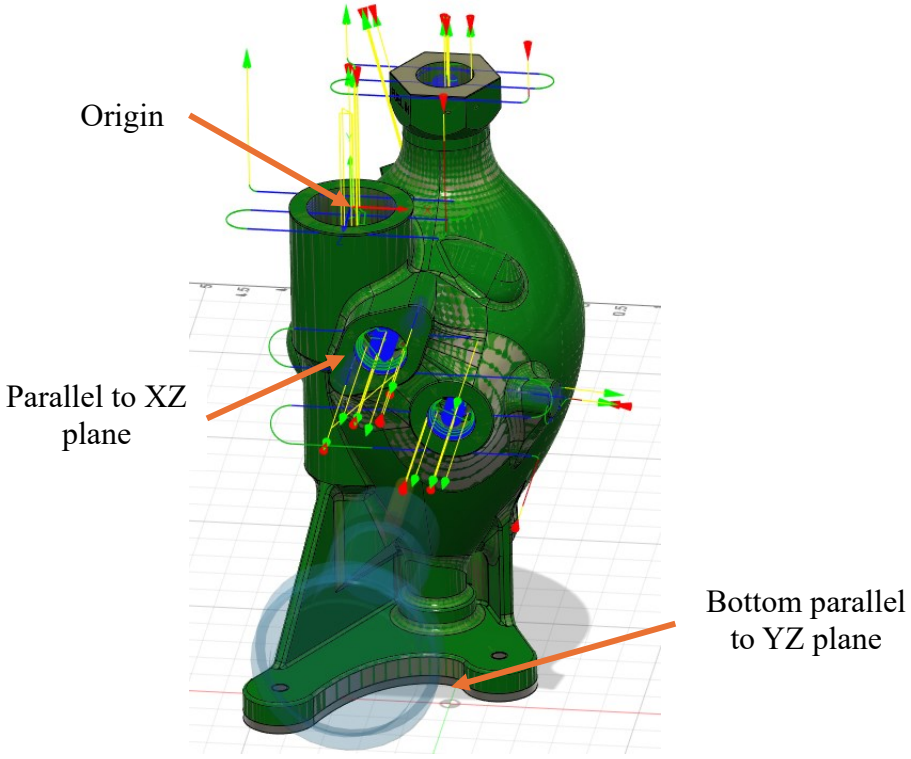

Figure 62: Visualization of the machining toolpaths in setup 1

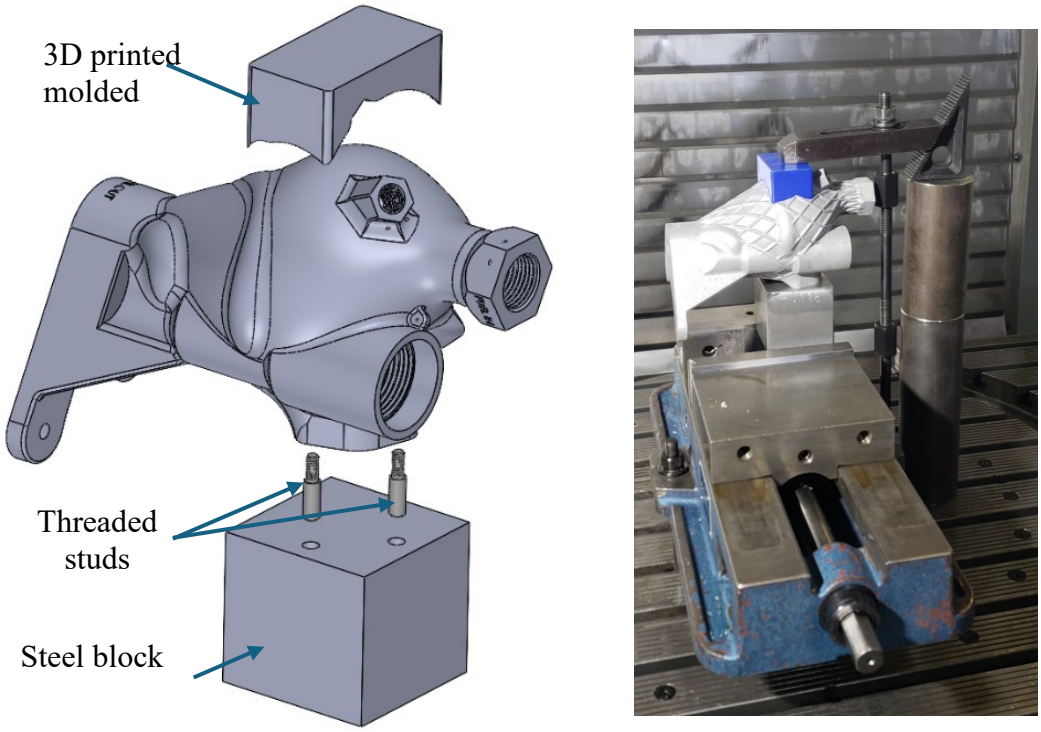

Figure 63: Machining setup 2 fixturing

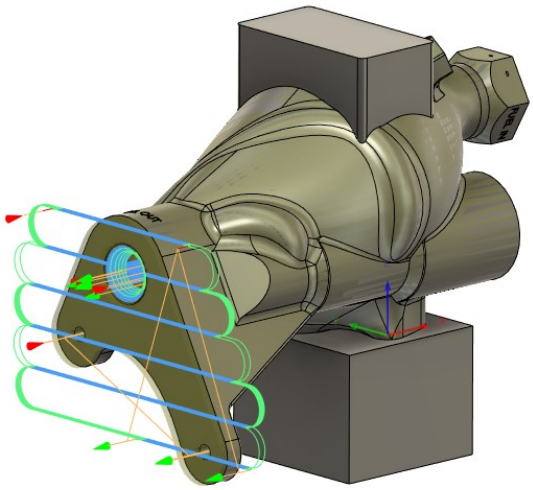

Figure 64: Visualization of the machining toolpaths in setup 2

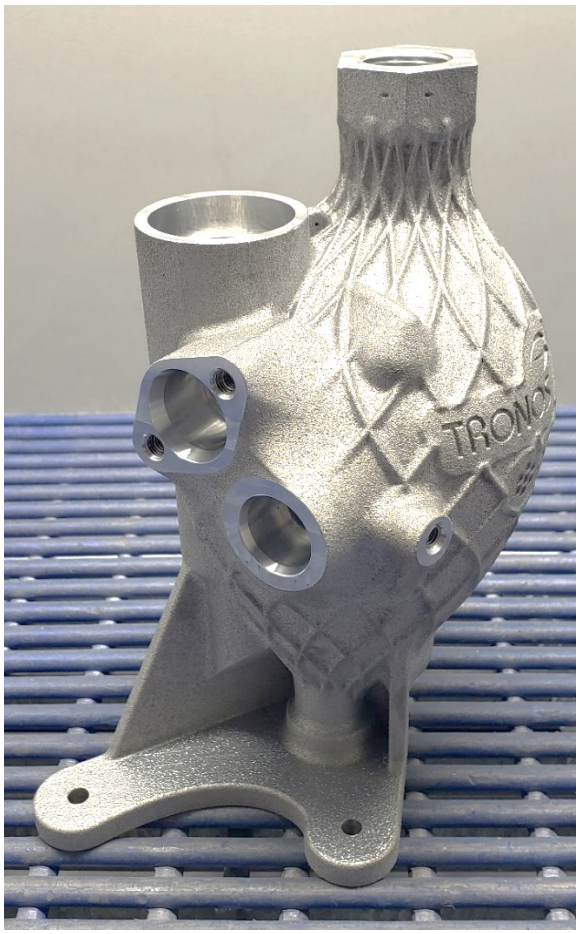

Figure 65: Machined AM heat exchanger

4.4 Dimensional Inspection

To ensure the dimensional accuracy of the machined AM heat exchanger, a dimensional inspection was performed. A 3D laser scan was conducted on the machined AM heat exchanger to capture its geometry. The laser scanner performs poorly on dark or reflective surfaces. Since the AM heat exchanger consisted of very reflective machined surfaces, a coat of vanishing white scanning spray was applied which creates a temporary optically ideal surface for laser scanning. The part was then scanned using a Hexagon Romer Absolute Arm Compact, with a HP-L-8.9 laser scanner attachment (Figure 66). The part deviation analysis was conducted using Hexagon PC-DMIS software (Figure 67). The results showed that approx. 75% of scanned points were within 0.1 mm of the CAD model.

This high level of accuracy indicates that the majority of the critical features closely matched the design specifications.

Figure 66: Laser scan setup of the AM heat exchanger

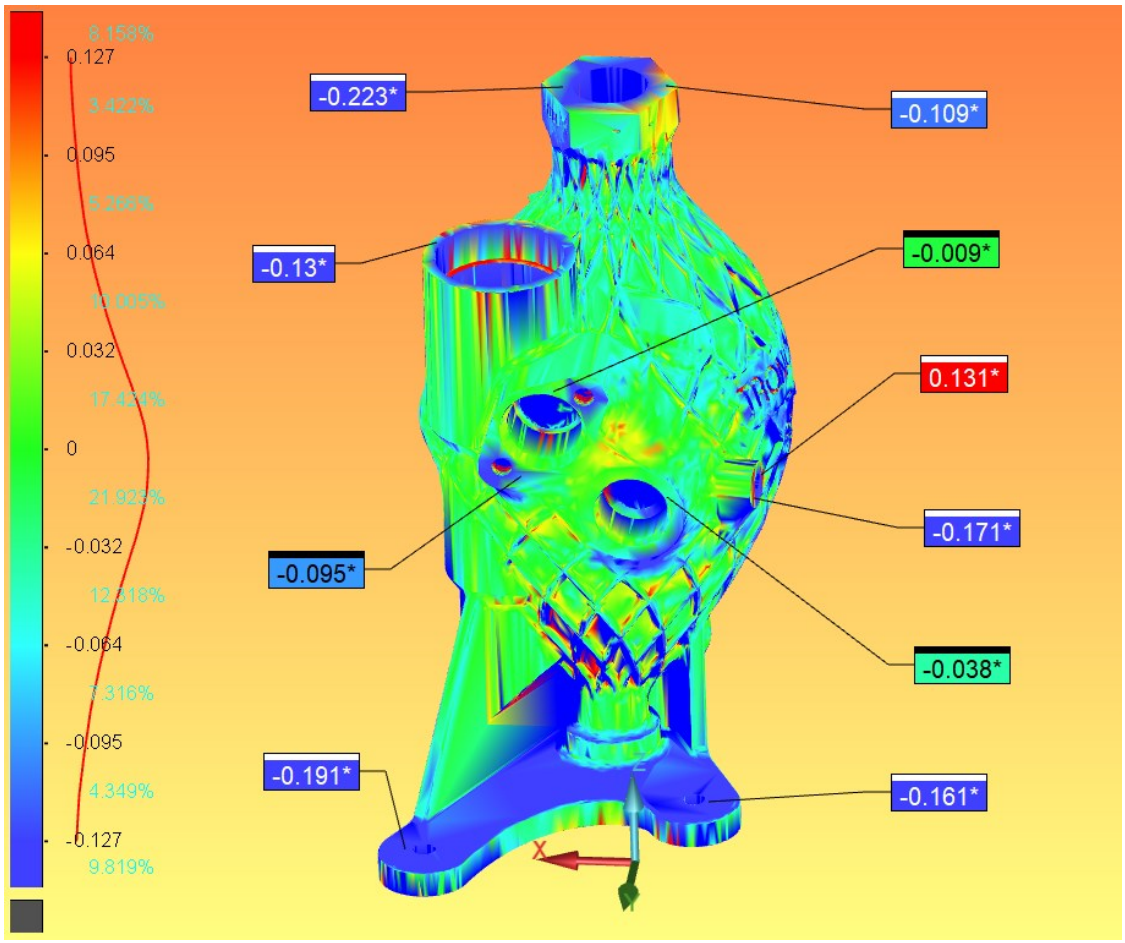

Figure 67: Deviation analysis between CAD and scan data

Chapter 5 Conclusions

This study presents a comprehensive redesign, numerical heat transfer analysis, and fabrication of a direct replacement aerospace heat exchanger. The primary objective was to leverage the capabilities of LPBF to enhance the performance and manufacturability of the device. This research demonstrated the feasibility and potential of using LPBF for manufacturing complex thermal systems like heat exchangers. Additionally, it provides a detailed design process for creating AM heat exchangers, offering a foundation for further exploration and optimization in this field. The following conclusions were reached on each phase of the development cycle:

1. AM Heat exchanger design:
   i. The external geometry of the heat exchanger was optimized by utilizing an inverse teardrop-shaped design to mitigate the need for external supports.
   ii. Gyroid, Diamond, Schwarz, and SplitP TPMS lattices were evaluated to identify the most suitable lattice geometry for the heat exchanger core. The diamond TPMS lattice exhibited the highest surface-to-volume ratio and the lowest pressure drop compared to the other lattices, making it the optimal choice for the AM heat exchanger core.
   iii. Fluid flow simulations were conducted to select the appropriate lattice cell size and baffle configuration that resulted in the required pressure drop for the heat exchanger application. A cell size of 12.5×12.5×30 mm was selected as it resulted in a pressure drop that is within the limits of the performance requirements of the application.
2. Heat transfer numerical analysis:
   i. The AlSi10Mg material with a lattice wall thickness of 0.75 mm resulted in similar thermal performance to the conventional heat exchanger.
   ii. Results indicated that the thermal resistance of the fluid domain was significantly higher than that of the solid material, suggesting that material choice had a minimal impact on fuel outlet temperature at steady state conditions.
3. Heat exchanger fabrication:

i. The complex AM heat exchanger was successfully printed from AlSi10Mg in a Renishaw RenAM 500S Flex LPBF system.
ii. Critical features that required a high precision in size and/or location were successfully machined to match those of the conventionally fabricated heat exchanger.
iii. The dimensional accuracy of the finished AM component was inspected using a 3D laser scanner, which revealed that approximately 75% of the scanned points were within 0.1 mm of the CAD model affirming a high fidelity to design specifications.
iv. The re-designed AM heat exchanger was 20% lighter than its conventional counterpart.

5.1 Future Work

Future work on the AM heat exchanger involves crucial steps to validate the performance and qualification of the manufacturing process. In terms of performance validations, the component must be tested as per the validation process utilized for the conventional component. This involves the physical testing of the AM heat exchanger to validate the pressure drop and thermal performance is within the requirements for the aircraft application. Additionally long-term testing under simulated operating conditions should be conducted to assess the durability and reliability of the heat exchanger over time. This includes thermal cycling, mechanical loading, and exposure to typical aerospace environmental conditions.

Furthermore, the manufacturing process must be qualified and certified before the heat exchanger can be installed in an aircraft engine. This includes the qualification of the LPBF system, material, print parameters, and post processes involved in manufacturing process. Due to the complex internal geometry, the depowdering process requires further attention to ensure the residual powder is removed to an acceptable level. The residual powder could be inspected through a computed tomography (CT) scan of the post processed component, or by designing a test component that replicates the internal geometry of the AM heat exchanger and sectioning the component and inspecting the internal geometry to validate

the powder removal process. Additionally, the outlet fluid can be monitored over an extended period and analyzed for any remaining powder particles. This approach could be used to confirm that residual powder levels have been reduced to an acceptable level.

By addressing these areas, future research can enhance the applicability and performance of AM heat exchangers, promoting their adoption in aerospace and other high-performance industries.

References

[1] Renishaw, "RenAM 500 metal additive manufacturing (3D printing) systems," Renishaw, [Online]. Available: https://www.renishaw.com/en/renam-500-metal-additive-manufacturing-3d-printing-systems--37011.

[2] GE Additive, SmarTech Publishing, "The additive journey: the time is now," 2022.

[3] U.S. Department of Energy, "High Intensity Thermal Exchange through Materials, and Manufacturing Processes," U.S. Department of Energy- Advanced Research Programs Agency, [Online]. Available: https://arpa-e.energy.gov/technologies/programs/hitemmp.

[4] S. Goguelin, "Better Heat Exchangers with Additive Manufacturing," ALL3DP, 18 08 2021. [Online]. Available: https://all3dp.com/1/better-heat-exchangers-with-additive-manufacturing/.

[5] GE Additive, "GE9X Additive Parts".

[6] S. A. Niknam, M. Mortazavi and D. Li , "Additively manufactured heat exchangers: A review on opportunities and challenges," *The International Journal of Advanced Manufacturing Technology,* pp. 601-618, 2020.

[7] T. Schnabel, M. Oettel and B. Mueller, "Design for additive manufacturing: Guidelines and case studies for metal applications.," Fraunhofer Institute for Machine Tools and Forming Technology IWU., 2017.

[8] K. Volchek and S. Pfau, "Revolutionizing heat exchangers with additively manufactured gyroids," 6 04 2023. [Online]. Available: https://heat-exchanger-world.com/revolutionizing-heat-exchangers-with-additively-manufactured-gyroids/.

[9] P. Zelinski, "3D-printed heat exchanger uses gyroids for better cooling: The Cool Parts Show #43. Additive Manufacturing.," 2022. [Online]. Available:

https://www.additivemanufacturing.media/articles/3d-printed-heat-exchanger-uses-gyroids-for-better-cooling-the-cool-parts-show-43.

[10] N. Baobaid, M. . I. Ali and K. A. Khan, "Fluid flow and heat transfer of porous TPMS architected heat sinks in free convection environment.," *Case Studies in Thermal Engineering,* 2022.

[11] Puntozero, "Liquid-cooled cold plate for automotive power electronics," 2023. [Online]. Available: nTop. (2023). Cold plate automotive power electronics. nTop. Retrieved from https://www.ntop.com/resources/case-studies/cold-plate-automotive-power-electronics/.

[12] M. M. Moradmand and A. Sohankar, "Numerical and experimental investigations on the thermal-hydraulic performance of heat exchangers with Schwarz-P and gyroid structures," *International Journal of Thermal Sciences,* 2024.

[13] Weldaloy, "Weight Reduction Critical to Improved Jet Engine Fuel Efficiency," [Online]. Available: https://weldaloy.com/press-release/weight-reduction-improved-aviation-fuel-efficiency/.

[14] C. A. Mouton, J. D. Powers, D. M. Romano, C. Guo, S. Bednarz and C. O'Connell, "Fuel Reduction for the Mobility Air Forces," *RAND Corporation,* 2015.

[15] H. M. Beresford, C. Boynton and L. Ranson, "Cabin Weight And Waste Cuts Help Sustainability Drive," 25 05 2023. [Online]. Available: https://aviationweek.com/air-transport/airlines-lessors/cabin-weight-waste-cuts-help-sustainability-drive.

[16] AviationOutlook, "How Changes in Aircraft Design and Components Reduce Fuel Consumption," 21 07 2023. [Online]. Available: https://aviationoutlook.com/how-changes-in-aircraft-design-and-components-reduce-fuel-consumption/.

[17] R. K. Shah and . D. P. Sekulic, Fundamentals of Heat Exchanger Design, John Wiley & Sons, Inc, 2003.

[18] Alfa Laval, "Gasketed plate heat exchangers," Alfa Laval Lund AB, Lund, Sweden, 2021.

[19] R. O'Hara and M. Vlahinos, "Unlock Breakthrough Heat Exchanger Designs with Gyroids," Ansys, 22 01 2020. [Online]. Available: https://www.ansys.com/blog/heat-exchanger-designs-gyroids.

[20] Q. Li and H. Zhou, "Heat Transfer Calculation," in *Theory and Calculation of Heat Transfer in Furnaces*, Elsevier , 2017, pp. 132-170.

[21] Linseis, "Guarded Hot Plate," Linseis, 2020. [Online]. Available: https://www.linseis.com/en/methods/guarded-hot-plate-ghp/.

[22] S. Tarasovs, O. Bulderberga, D. Zeleniakiene and A. Aniskevich, "Sensitivity of the Transient Plane Source Method to Small Variations of Thermal Conductivity," *International Journal of Thermophysics,* vol. 42, p. 173, 2021.

[23] Linseis, "Dilatometer Dilatometry – expansion measurement – DIL," Linseis, [Online]. Available: https://www.linseis.com/produkte/dilatometer/.

[24] Linseis, "DIL L75 Laser Highest Precision Laser-Dilatometer," Linseis, [Online]. Available: https://www.linseis.com/en/products/dilatometer/dil-l75-laser/.

[25] Linseis, "DIL L75 PT Horizontal dilatometer for research applications," Linseis, [Online]. Available: https://www.linseis.com/produkte/dilatometer/l75-pt-horizontal/.

[26] ASTM E1269-24, "Standard Test Method for Determining Specific Heat Capacity by Differential Scanning Calorimetry," ASTM, 2024.

[27] NETZSCH, "Light/Laser Flash Analyzer," NETZSCH, [Online]. Available: https://analyzing-testing.netzsch.com/en/products/thermal-diffusivity-and-conductivity.

[28] ASTM E1461-13(2022), "Standard Test Method for Thermal Diffusivity by the Flash Method," ASTM, 2022.

[29] I. Yadroitsev, . I. Yadroitsava and A. Du Plessis, "Basics of laser powder bed fusion," in *Fundamentals of Laser Powder Bed Fusion of Metals*, Elsevier, 2021, pp. 15-38.

[30] L. Ramineni, A. Almotari, M. Ali, A. Algamal and A. Qattawi, "Residual Stress Mapping in Heat-Assisted Additive Manufacturing of IN 718: An X-Ray Diffraction Study," *Journal of Materials Enigneering and Performance,* vol. 33, pp. 4124-4135, 2024.

[31] B. Bevans, C. Barrett, T. Spears, A. Gaikwad, A. Riensche, Z. Smoqi, H. S. Halliday and P. Rao, "Heterogeneous sensor data fusion for multiscale, shape agnostic flaw detection in laser powder bed fusion additive manufacturing," *Virtual and Physical Prototyping,* vol. 18, 2023.

[32] M. Munsch, M. Schmidt-Lehr, E. Wycisk and T. Führer, "AMPOWER REPORT 2024," AMPower, 2024.

[33] J. R. Davis, "Aluminum and Aluminum Alloys, Alloying: Understanding the Basics," ASM International, 2001.

[34] R. R. J. Sélo, S. C. Smith, I. Maskery, I. Ashcroft and C. Tuck, "On the thermal conductivity of AlSi10Mg and lattice structures made by laser powder bed fusion," *Additive Manufacturing,* vol. 34, 2020.

[35] H. H. Zhu, J. Y. H. Fuh and L. Lu, "The influence of powder apparent density on the," *Machine Tools & Manufacture,* vol. 47, pp. 294-298, 2007.

[36] C. Weiss, J. Heslenfeld, J. Saewe, S. Bremen and C. L. Häfner, "Investigation on the influence of powder humidity in Laser Powder Bed Fusion (LPBF)," *Procedia CIRP,* vol. 111, pp. 115-120, 2022.

[37] O. Diegel, A. Nordin and D. Motte, A Practical Guide to Design for Additive Manufacturing, Springer, 2020.

[38] D. Bentley, "A Deep Dive into Metal 3D PrintingA Deep Dive into Metal 3D Printing," Protolab, 2020.

[39] A. H. Schoen, "Infinite periodic minimal surfaces without self-intersections," *NASA Technical Note D-5541,* 1970.

[40] Ansys, "New Fluent Meshing Workflow Quickly Wraps Non-Watertight, Dirty Geometries," 25 06 2019. [Online]. Available: https://www.ansys.com/blog/fluent-meshing-workflow-wraps-non-watertight-geometries.

[41] Xometry, *Data Sheet Aluminium AlSi10Mg.*

Appendix A: LFA Test Specimen Engineering Drawing

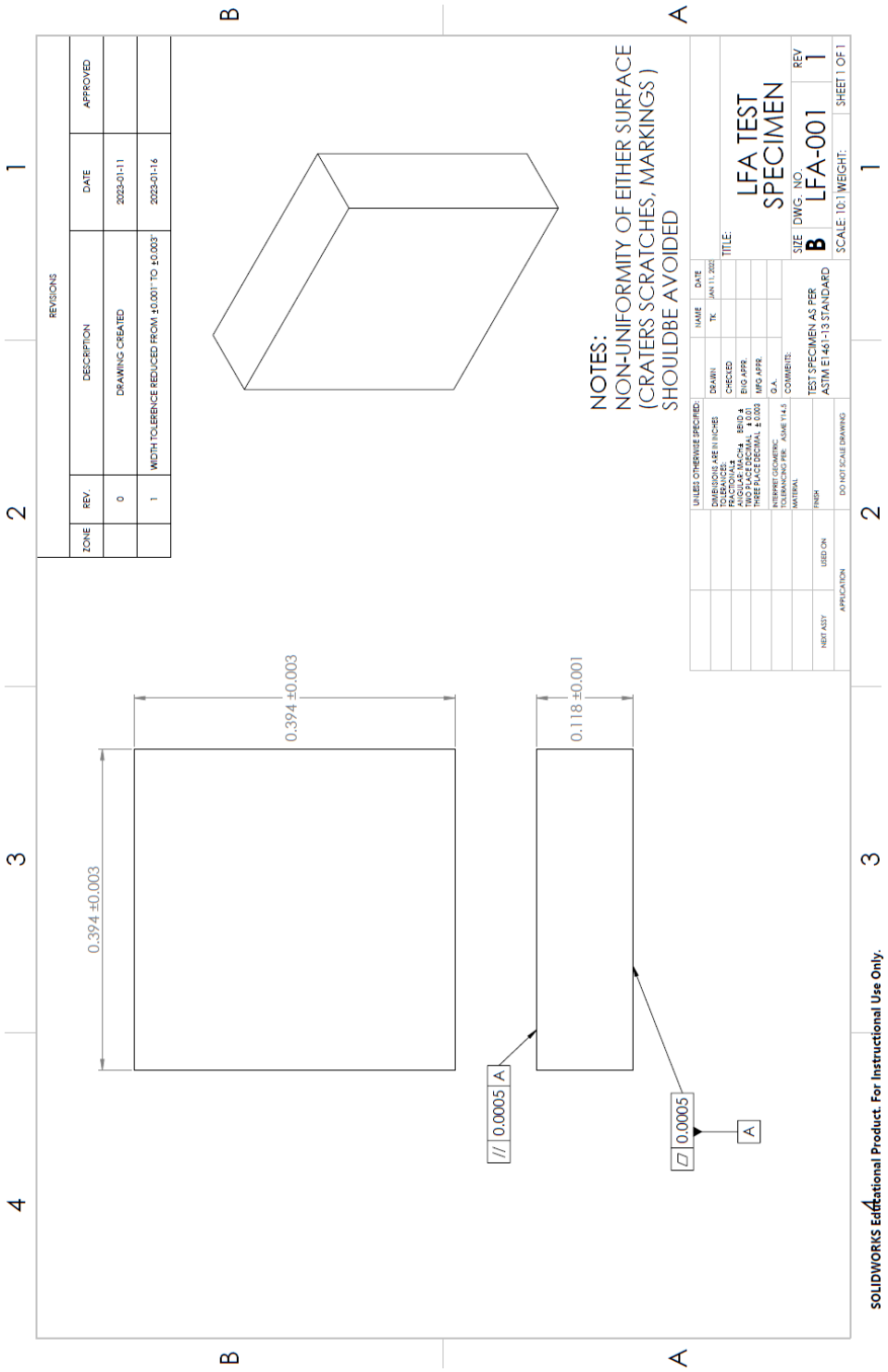

Appendix B: AM Heat Exchanger Engineering Drawing

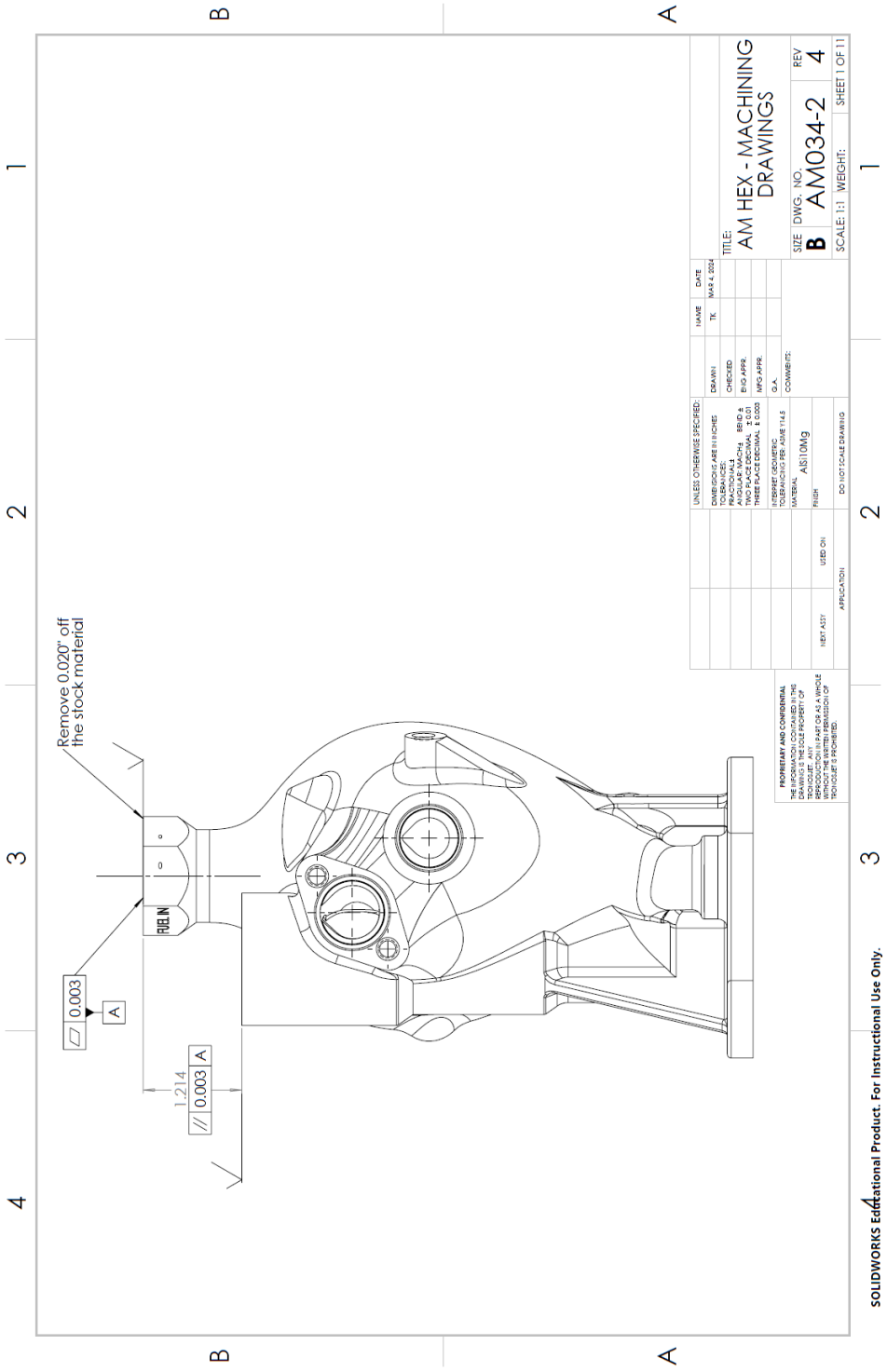

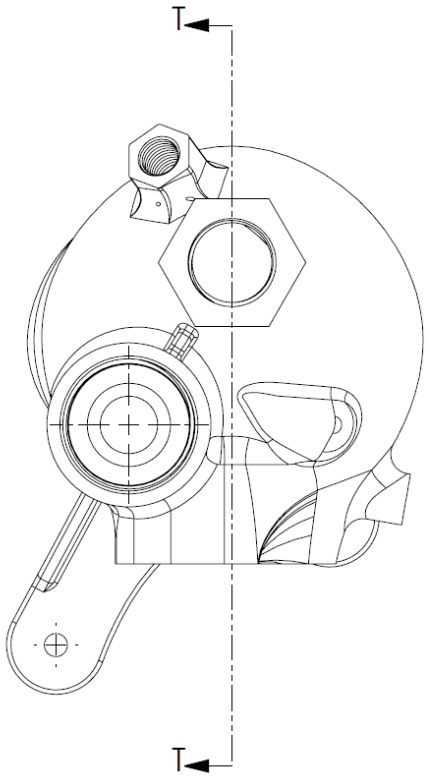

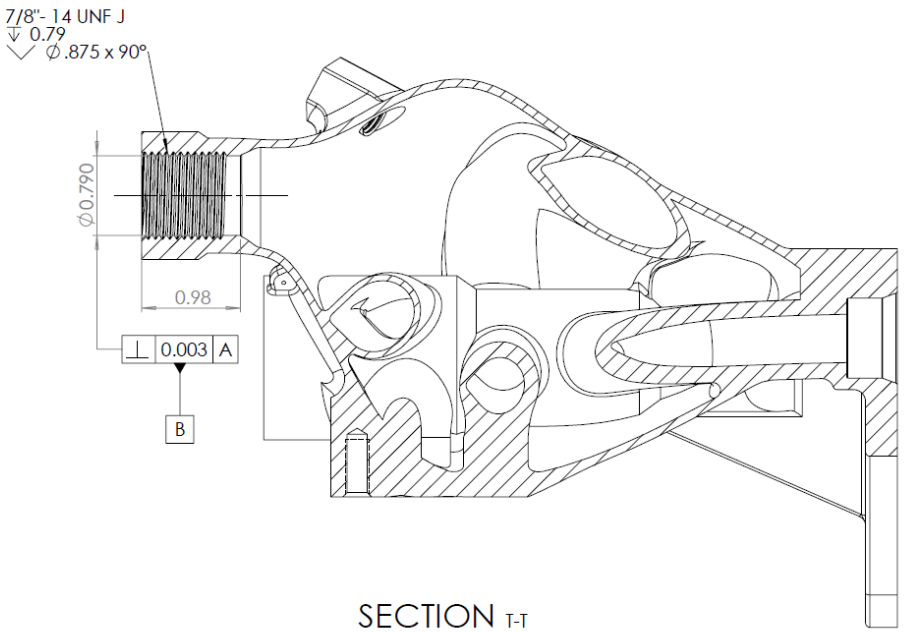

SECTION T-T

		UNLESS OTHERWISE SPECIFIED:		NAME	DATE
		DIMENSIONS ARE IN INCHES TOLERANCES: FRACTIONAL ± ANGULAR: MACH ± BEND ± TWO PLACE DECIMAL ± 0.01 THREE PLACE DECIMAL ± 0.005	DRAWN	TK	MAR 4, 2024
			CHECKED		
			ENG APPR.		
			MFG APPR.		
		INTERPRET GEOMETRIC TOLERANCING PER: ASME Y14.5	Q.A.		
		MATERIAL AlSi10Mg	COMMENTS:		
NEXT ASSY	USED ON	FINISH			
APPLICATION		DO NOT SCALE DRAWING			

TITLE:
AM HEX - MACHINING DRAWINGS

SIZE	DWG. NO.	REV
B	AM034-2	4

SCALE: 1:1 | WEIGHT: | SHEET 2 OF 11

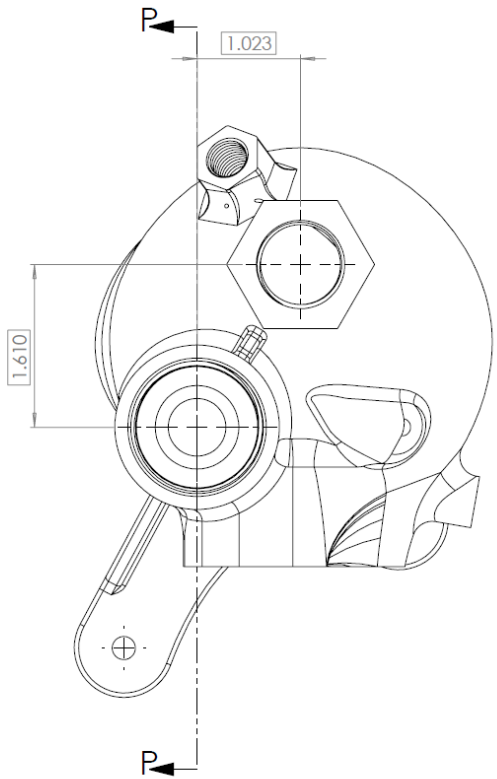

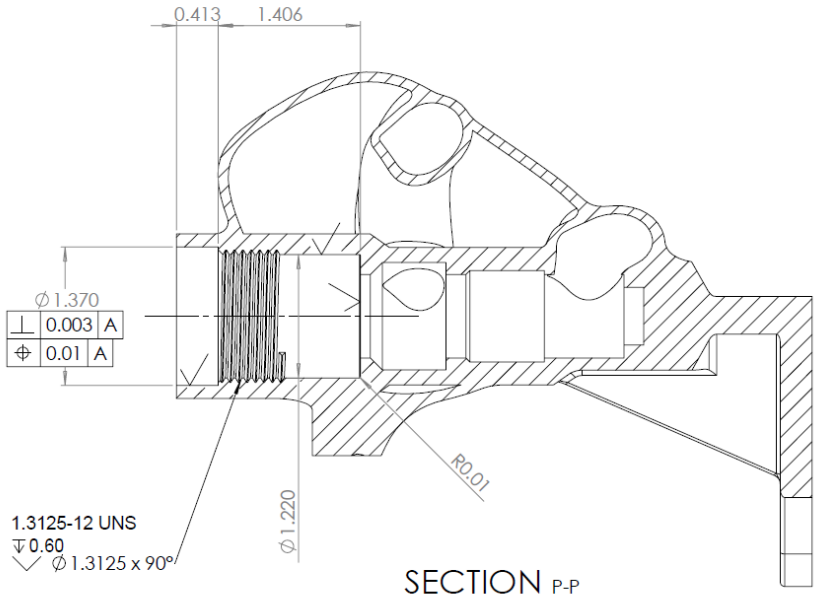

SECTION P-P

		UNLESS OTHERWISE SPECIFIED:		NAME	DATE
		DIMENSIONS ARE IN INCHES TOLERANCES: FRACTIONAL ± ANGULAR: MACH ± BEND ± TWO PLACE DECIMAL ± 0.01 THREE PLACE DECIMAL ± 0.003	DRAWN	TK	MAR 4, 2024
			CHECKED		
			ENG APPR.		
			MFG APPR.		
		INTERPRET GEOMETRIC TOLERANCING PER: ASME Y14.5	Q.A.		
		MATERIAL AlSi10Mg	COMMENTS:		
NEXT ASSY	USED ON	FINISH			
APPLICATION		DO NOT SCALE DRAWING			

TITLE: AM HEX - MACHINING DRAWINGS

SIZE	DWG. NO.	REV
B	AM034-2	4

SCALE: 1:1 | WEIGHT: | SHEET 3 OF 11

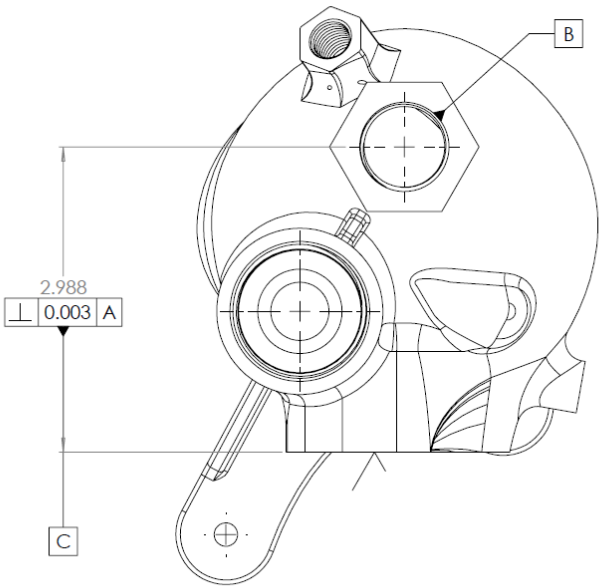

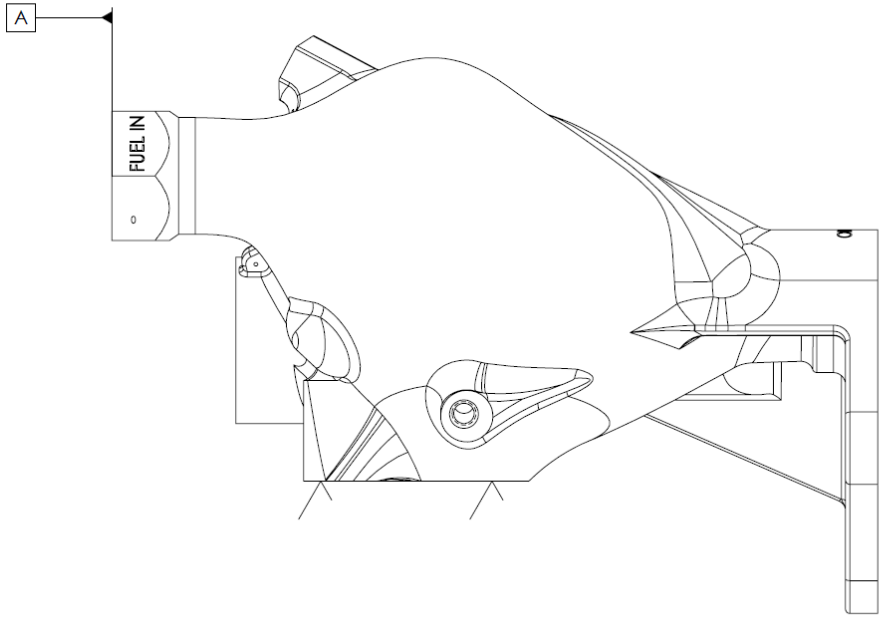

		UNLESS OTHERWISE SPECIFIED:		NAME	DATE
		DIMENSIONS ARE IN INCHES TOLERANCES: FRACTIONAL ± ANGULAR: MACH ± BEND ± TWO PLACE DECIMAL ± 0.01 THREE PLACE DECIMAL ± 0.003	DRAWN	TK	MAR 4, 2024
			CHECKED		
			ENG APPR.		
			MFG APPR.		
			Q.A.		
			COMMENTS:		
		INTERPRET GEOMETRIC TOLERANCING PER: ASME Y14.5			
		MATERIAL AlSi10Mg			
NEXT ASSY	USED ON	FINISH			
APPLICATION		DO NOT SCALE DRAWING			

TITLE:
AM HEX - MACHINING DRAWINGS

SIZE	DWG. NO.	REV
B	AM034-2	4

SCALE: 1:1 | WEIGHT: | SHEET 4 OF 11

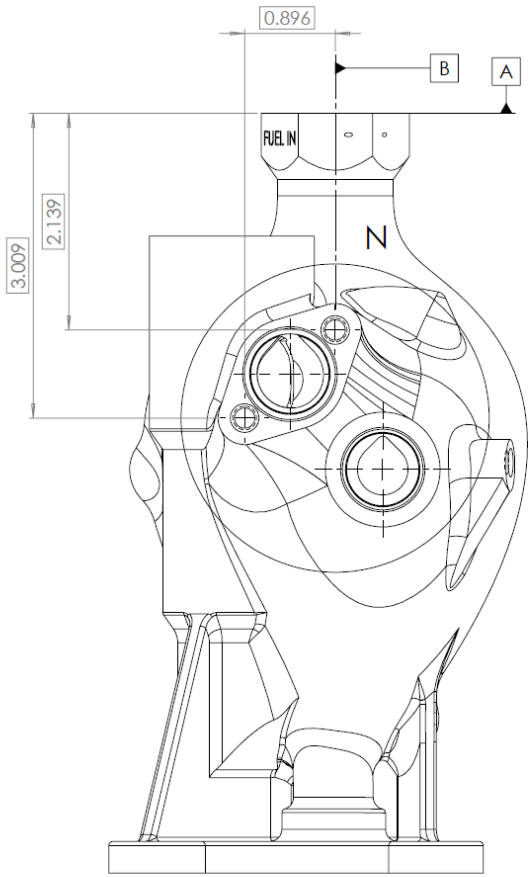

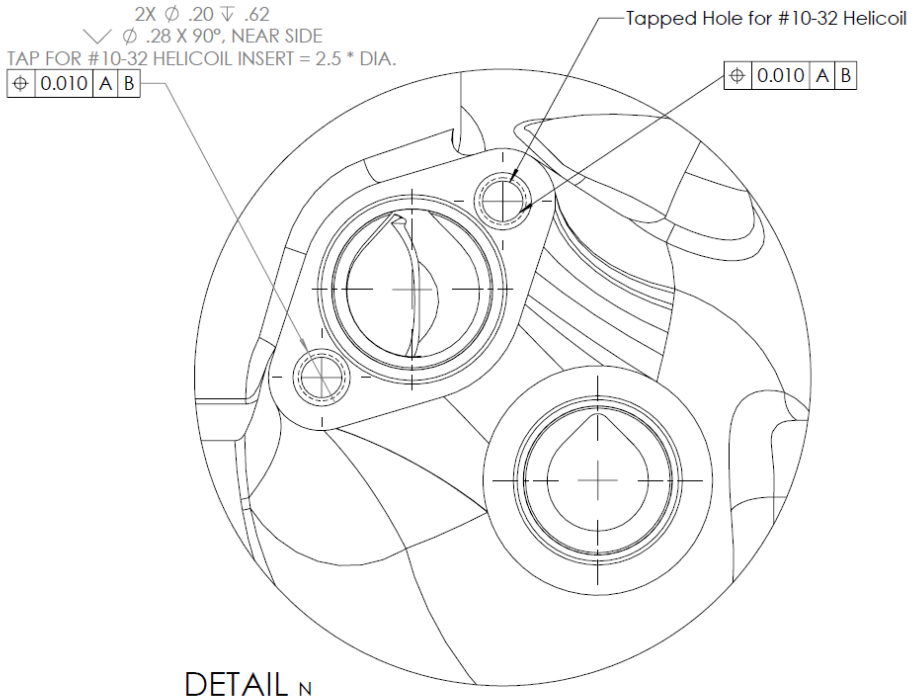

DETAIL N

SCALE 2 : 1

		UNLESS OTHERWISE SPECIFIED:		NAME	DATE
		DIMENSIONS ARE IN INCHES TOLERANCES: FRACTIONAL ± ANGULAR: MACH ± BEND ± TWO PLACE DECIMAL ± 0.01 THREE PLACE DECIMAL ± 0.005	DRAWN	TK	MAR 4, 2024
			CHECKED		
			ENG APPR.		
			MFG APPR.		
		INTERPRET GEOMETRIC TOLERANCING PER: ASME Y14.5	Q.A.		
		MATERIAL AlSi10Mg	COMMENTS:		
NEXT ASSY	USED ON	FINISH			
APPLICATION		DO NOT SCALE DRAWING			

TITLE:
AM HEX - MACHINING DRAWINGS

SIZE	DWG. NO.	REV
B	AM034-2	4
SCALE: 1:1	WEIGHT:	SHEET 5 OF 11

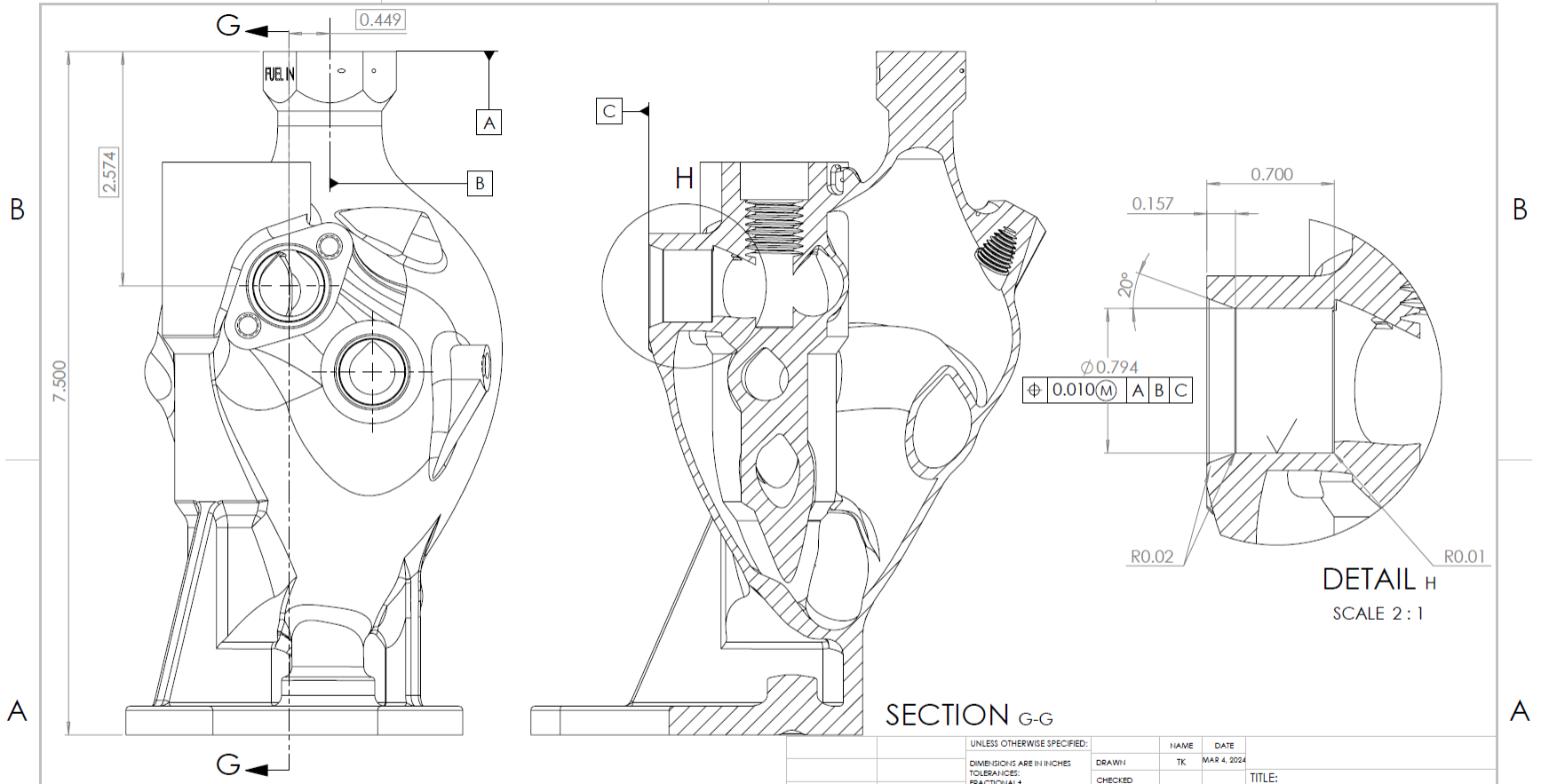

		UNLESS OTHERWISE SPECIFIED:		NAME	DATE
		DIMENSIONS ARE IN INCHES TOLERANCES: FRACTIONAL ± ANGULAR: MACH ± BEND ± TWO PLACE DECIMAL ± 0.01 THREE PLACE DECIMAL ± 0.005	DRAWN	TK	MAR 4, 2024
			CHECKED		
			ENG APPR.		
			MFG APPR.		
		INTERPRET GEOMETRIC TOLERANCING PER: ASME Y14.5	Q.A.		
		MATERIAL AlSi10Mg	COMMENTS:		
NEXT ASSY	USED ON	FINISH			
APPLICATION		DO NOT SCALE DRAWING			

TITLE:
AM HEX - MACHINING DRAWINGS

SIZE	DWG. NO.	REV
B	AM034-2	4
SCALE: 1:1	WEIGHT:	SHEET 6 OF 11

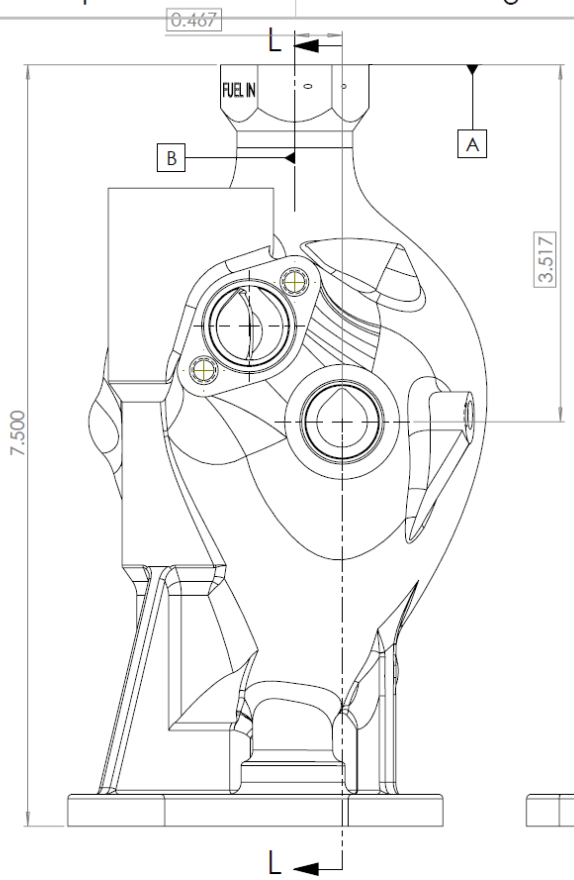

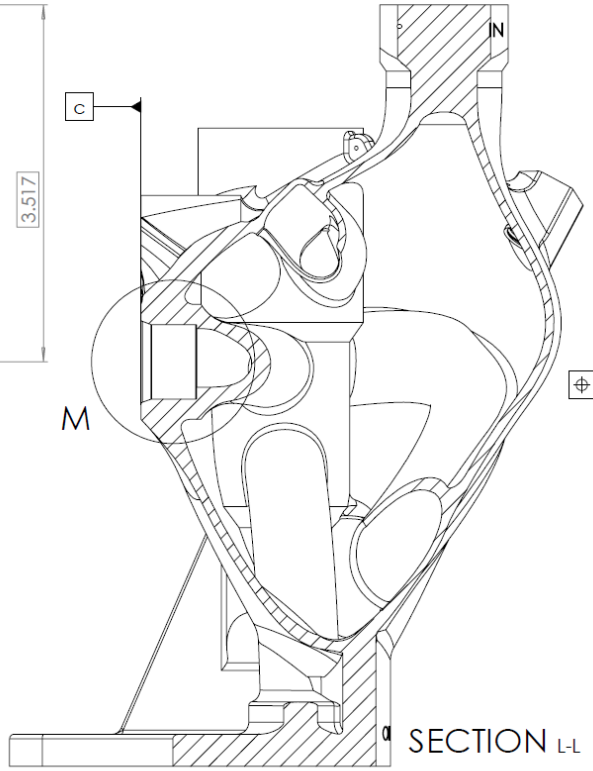

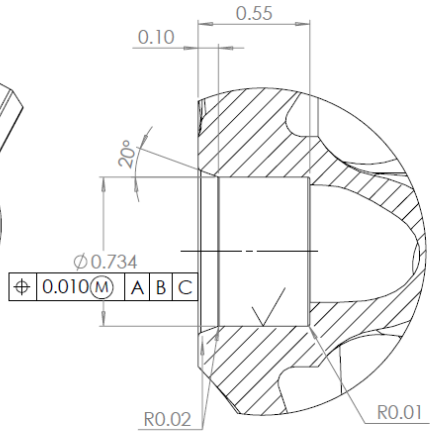

DETAIL M
SCALE 2 : 1

		UNLESS OTHERWISE SPECIFIED:		NAME	DATE
		DIMENSIONS ARE IN INCHES	DRAWN	TK	MAR 4, 2024
		TOLERANCES: FRACTIONAL ± ANGULAR: MACH ± BEND ± TWO PLACE DECIMAL ± 0.01 THREE PLACE DECIMAL ± 0.003	CHECKED		
			ENG APPR.		
			MFG APPR.		
		INTERPRET GEOMETRIC TOLERANCING PER:	Q.A.		
		MATERIAL AlSi10Mg	COMMENTS:		
NEXT ASSY	USED ON	FINISH			
APPLICATION		DO NOT SCALE DRAWING			

PROPRIETARY AND CONFIDENTIAL
THE INFORMATION CONTAINED IN THIS DRAWING IS THE SOLE PROPERTY OF TRONSOJET. ANY REPRODUCTION IN PART OR AS A WHOLE WITHOUT THE WRITTEN PERMISSION OF TRONOSJET IS PROHIBITED.

TITLE: AM HEX - MACHINING DRAWINGS

SIZE	DWG. NO.	REV
B	AM034-2	4
SCALE: 1:1	WEIGHT:	SHEET 7 OF 11

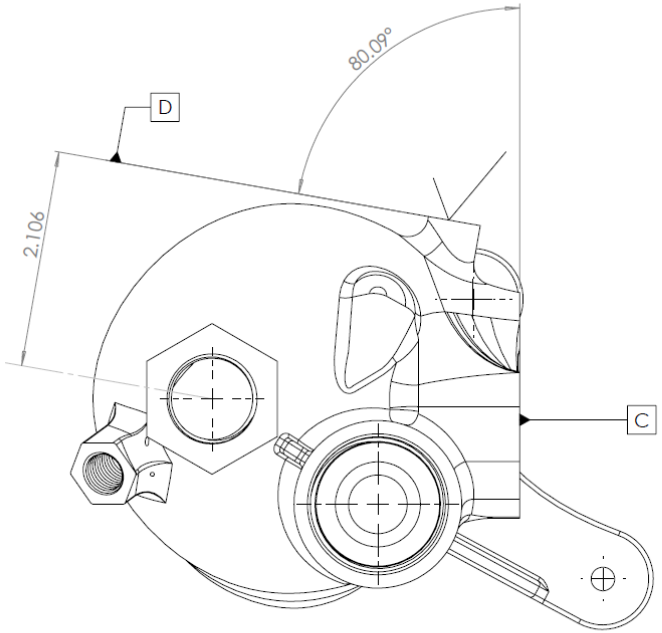

		UNLESS OTHERWISE SPECIFIED:		NAME	DATE
		DIMENSIONS ARE IN INCHES TOLERANCES: FRACTIONAL ± ANGULAR: MACH ± BEND ± TWO PLACE DECIMAL ± 0.01 THREE PLACE DECIMAL ± 0.003	DRAWN	TK	MAR 4, 2024
			CHECKED		
			ENG APPR.		
			MFG APPR.		
		INTERPRET GEOMETRIC TOLERANCING PER: ASME Y14.5	Q.A.		
		MATERIAL AlSi10Mg	COMMENTS:		
NEXT ASSY	USED ON	FINISH			
APPLICATION		DO NOT SCALE DRAWING			

TITLE:
AM HEX - MACHINING DRAWINGS

SIZE	DWG. NO.	REV
B	AM034-2	4

SCALE: 1:1 | WEIGHT: | SHEET 8 OF 11

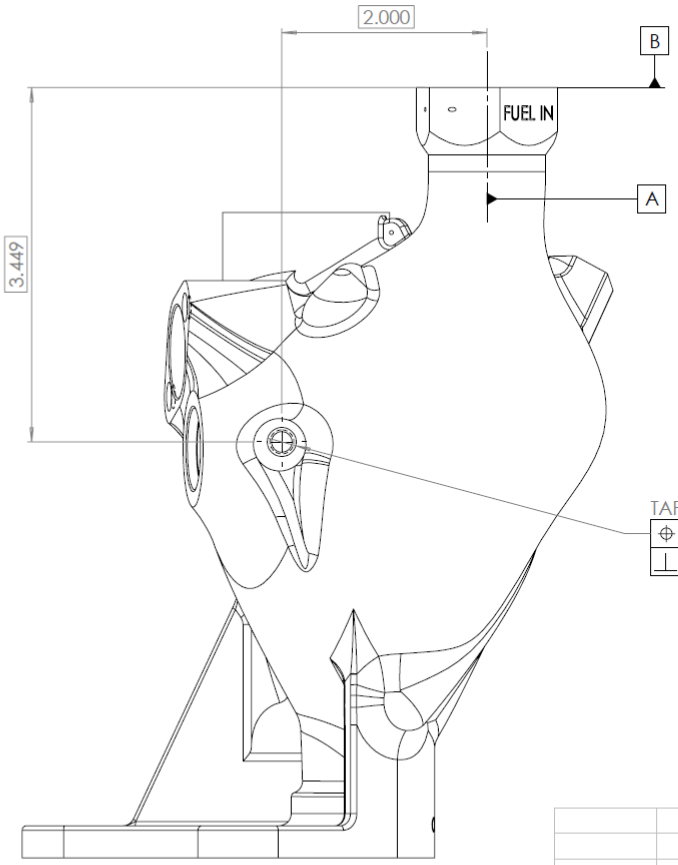

⌀ .20 ↧ .62
⌵ ⌀ .28 X 90°, NEAR SIDE
TAP FOR #10-32 HELICOIL INSERT = 2.5 * DIA.

⌖	0.01	A	B	D
⊥	0.01	D		

		UNLESS OTHERWISE SPECIFIED:		NAME	DATE
		DIMENSIONS ARE IN INCHES TOLERANCES: FRACTIONAL ± ANGULAR: MACH ± BEND ± TWO PLACE DECIMAL ± 0.01 THREE PLACE DECIMAL ± 0.005	DRAWN	TK	MAR 4, 2024
			CHECKED		
			ENG APPR.		
			MFG APPR.		
		INTERPRET GEOMETRIC TOLERANCING PER: ASME Y14.5	Q.A.		
		MATERIAL AlSi10Mg	COMMENTS:		
NEXT ASSY	USED ON	FINISH			
APPLICATION		DO NOT SCALE DRAWING			

TITLE:
AM HEX - MACHINING DRAWINGS

SIZE	DWG. NO.	REV
B	AM034-2	4

SCALE: 1:1 | WEIGHT: | SHEET 9 OF 11

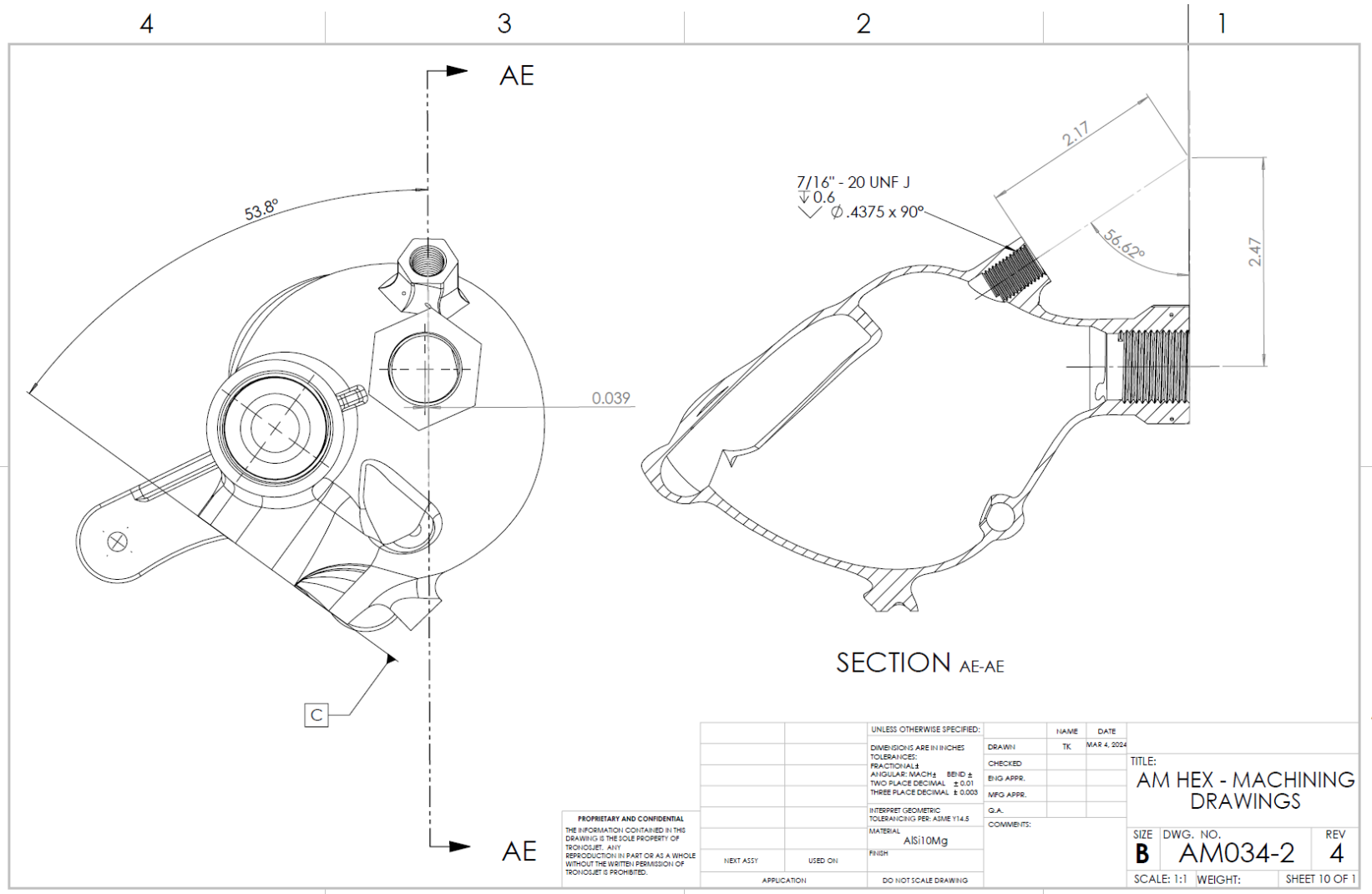

		UNLESS OTHERWISE SPECIFIED:		NAME	DATE
		DIMENSIONS ARE IN INCHES	DRAWN	TK	MAR 4, 2024
		TOLERANCES:	CHECKED		
		FRACTIONAL ±	ENG APPR.		
		ANGULAR: MACH ± BEND ±	MFG APPR.		
		TWO PLACE DECIMAL ± 0.01	Q.A.		
		THREE PLACE DECIMAL ± 0.005	COMMENTS:		
		INTERPRET GEOMETRIC TOLERANCING PER: ASME Y14.5			
		MATERIAL AlSi10Mg			
NEXT ASSY	USED ON	FINISH			
APPLICATION		DO NOT SCALE DRAWING			

TITLE: AM HEX - MACHINING DRAWINGS

SIZE	DWG. NO.	REV
B	AM034-2	4

SCALE: 1:1 WEIGHT: SHEET 10 OF 1

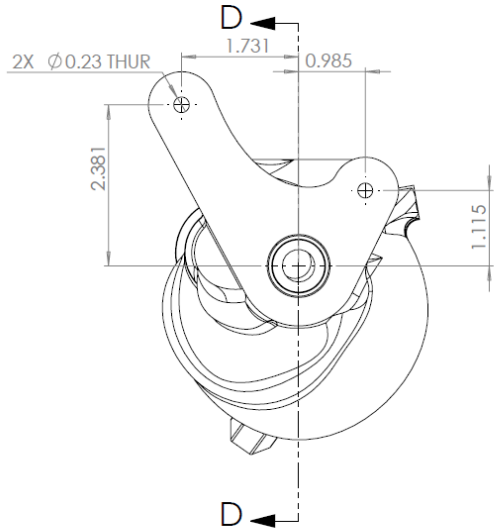

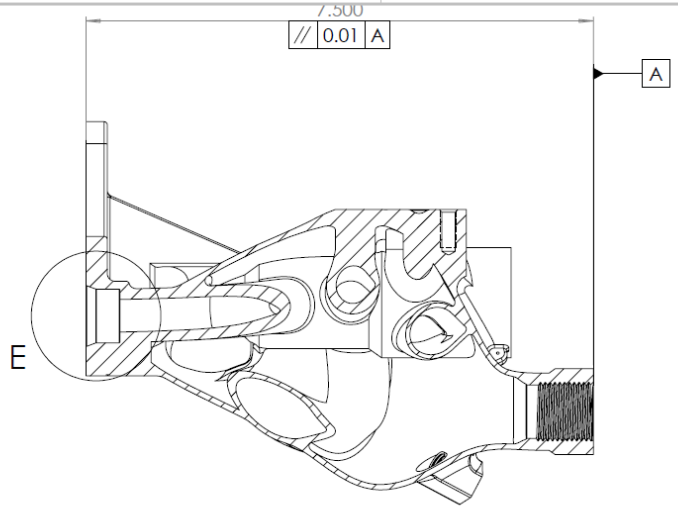

SECTION D-D
SCALE 1 : 1.5

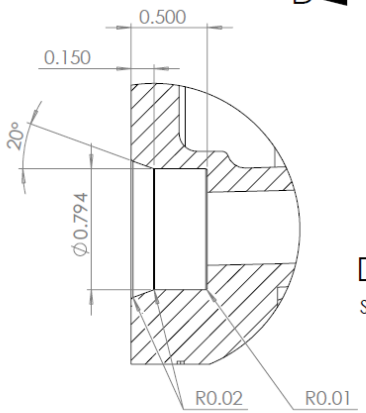

DETAIL E
SCALE 1.5 : 1

PROPRIETARY AND CONFIDENTIAL
THE INFORMATION CONTAINED IN THIS DRAWING IS THE SOLE PROPERTY OF TRONOJET. ANY REPRODUCTION IN PART OR AS A WHOLE WITHOUT THE WRITTEN PERMISSION OF TRONOSJET IS PROHIBITED.

UNLESS OTHERWISE SPECIFIED:		NAME / DATE
DIMENSIONS ARE IN INCHES	DRAWN	TK / MAR 4, 2024
TOLERANCES: FRACTIONAL ± ANGULAR: MACH ± BEND ± TWO PLACE DECIMAL ± 0.01 THREE PLACE DECIMAL ± 0.003	CHECKED	
	ENG APPR.	
	MFG APPR.	
INTERPRET GEOMETRIC TOLERANCING PER: ASME Y14.5	Q.A.	
MATERIAL AlSi10Mg	COMMENTS:	
FINISH		
NEXT ASSY / USED ON		
APPLICATION	DO NOT SCALE DRAWING	

TITLE: AM HEX - MACHINING DRAWINGS

SIZE	DWG. NO.	REV
B	AM034-2	4

SCALE: 1:1 | WEIGHT: | SHEET 11 OF 1